MECHANISTIC IMPLICATIONS FROM *IN OPERANDO* OPTICAL AND ELECTROCHEMICAL STUDIES OF BIO-RELATED FUEL CHEMISTRY IN SOLID OXIDE FUEL CELLS

by

John David Kirtley

A dissertation submitted in partial fulfillment
of the requirements for the degree

of

Doctor of Philosophy

in

Chemistry

MONTANA STATE UNIVERSITY
Bozeman, Montana

December 2014

DEDICATION

For Jesus: Your grace and presence has sustained me in every way, and I have fallen more in love with You, as I follow You in this race set before me. . .

For Mom and Dad: You have generously given so much to initiate me on my life and scholastic journey, and you have always been there to encourage me to run farther. . .

For numerous family and friends--proverbial iron-sharpeners: you have provided invaluable support when you ran alongside me during the tough and easy miles. . .

For Rob: you have coached and inspired me in the last several miles and made possible my scholastic aspirations. . .

For the love of my life and soon-to-be bride, Stephanie: I am so excited and privileged to run the rest of this race with you as we embark upon new life-long adventures. . .

ACKNOWLEDGEMENTS

I am forever thankful to so many in my life. First, and most importantly, I thank my heavenly Father for giving His strength and grace that has been needed for each step along the way. My fiancé, Stephanie Shively, has been so supportive and has provided balance in this busy season of transition, and cannot wait for the next, life-long step with my best friend. My parents have exemplified a rich heritage of love for Jesus, and taught me the value of creative and critical thinking through my homeschooling education.

I am humbled by the generous investment by so many others that have made this milestone possible. Rob Walker has provided invaluable support and leadership in my professional growth and inspired me to new heights. Michael Pomfret and Jeffrey Owrutsky have provided critical mentoring for integrated optical techniques at the US Naval Research Laboratory (NRL), and challenged me to hone my scientific approach.

Others have helped along the way. I would like to thank NRL for hosting me during several collaborative trips, and particularly Daniel Steinhurst and Harold Ladouceur (NRL). Josephine Hill, Anand Singh, and Thomas Oswell (University of Calgary) co-authored and provided samples for the carbon removal experiments. Bryan Eigenbrodt mentored me in my early days. David Halat, Melissa McIntyre, Kyle Reeping and Daniel Neuburger (MSU), have assisted in lengthy experiments and discussions. Stephen Sofie provided use of his lab facilities for SOFC construction. Robert Szilagyi first inspired me to consider graduate school. Finally, I give a big thanks to my committee members!

TABLE OF CONTENTS

TABLE OF CONTENTS - CONTINUED

TABLE OF CONTENTS - CONTINUED

TABLE OF CONTENTS - CONTINUED

LIST OF TABLES

Table Page

LIST OF FIGURES

Figure Page

LIST OF FIGURES – CONTINUED

Figure Page

LIST OF FIGURES – CONTINUED

Figure Page

LIST OF FIGURES – CONTINUED

Figure Page

NOMENCLATURE

Abbreviation	Definition
A	Ampere
BG	Surrogate Biogas
BuOH	*n*-Butanol
$C_{(s)}$	Adsorbed, elemental carbon
CCD	Charge Coupled Device
CHP	Combined Heating and Power
CP	Chronopotentiometry
E	Energy
EIS	Electrochemical Impedance Spectroscopy
EDX	Energy Dispersive X-ray
FEM	Field Emission Microscopy
FTIR	Fourier Transform Infrared
h	Planck's Constant
I	Current
I_{max}	Maximum Current (measured at 0 V)
IR	Infrared
LHV	Lower Heating Value
LSV	Linear Sweep Voltam metry
MEA	Membrane Electrode Assembly
MIEC	Mixed Ionic and Electronic Conductor
NIR	Near Infrared
NRL	Naval Research Laboratory (D.C.)
P	Power
PEM	Proton exchange membrane
Pa	Pascal
P_{CO2}	Partial Pressure of CO_2
P_{H2O}	Partial Pressure of H_2O
P_{max}	Maximum Power
R_B	Pure Impedance (x-intercept), from EIS
R_P	Polarization resistance, from EIS
R_1	High Frequency Capacitance Arc, from EIS
R_2	Middle Frequency Capacitance Arc, from EIS
R_3	Low Frequency Capacitance Arc, from EIS
SEM	Scanning Electron Microscopy
SOFC	Solid Oxide Fuel Cell
SCP	Spectrachronopotentiometry
TGA	Thermogravimetric Analysis
TPB	Triple Phase Boundary
TPO	Temperature Programmed Oxidation
UV	Ultraviolet

NOMENCLATURE

V	Volt
YSZ	Yttrium-stabilized Zirconia
XPS	X-ray photoelectron spectroscopy
XRD	X-ray diffraction
Z_{imag}	Imaginary Impedance, or capacitance
Z_{real}	Real Impedance, or pure resistance
v	Frequency (of light)

ABSTRACT

Solid oxide fuel cells using bio-renewable fuels promise efficient, sustainable, and clean electricity production, and are becoming more attractive sources of electrical power as global consumption of non-renewables accelerates. The excellent efficiencies of solid oxide fuel cells as solid state electrochemical devices arise mainly from the direct conversion of chemical to electrical energy--through oxygen reduction at the cathode, oxide diffusion through the electrolyte, and fuel oxidation at the anode. Some of these processes possess high activation energies, requiring high operational temperatures (generally > 650 °C). These conditions can hasten deleterious carbon accumulation and anode deterioration. These high operating temperatures also pose significant challenges in directly observing chemical reactions responsible for electrochemical oxidation and materials degradation. Yet, these observations are needed to understand fundamental mechanisms responsible for these processes—an understanding necessary to improve the performance, durability and versatility of SOFCs, especially as these devices are required to operate with complex fuels and fuel mixtures. In this work, solid oxide fuel cells constructed with traditional Ni/yttrium stabilized zirconia ceramic-metallic (or cermet) anodes are studied *in operando* and *in situ* with several novel optical techniques (Raman vibrational spectroscopy, near infrared thermal imaging and fourier-transform infrared emission spectroscopy) and electrochemical measurements that provide vital insights into mechanisms surrounding bio-related fuel electrochemistry. The first study demonstrated that Ni oxidation is slower than reduction at the anode. The second study quantified *electrochemically accessible* anode carbon accumulation under methane fuel, while detailing deleterious mechanisms and microstructural changes that accompany cell polarization in the absence of gas phase fuels. The third study explored the kinetics of carbon removal from Ni-based anodes by CO_2, H_2O, and O_2 and detailed mechanistically why they may be different. The fourth study revealed mechanisms associated with carbon formation and current generation from biogas and methane as a function of operational condition. Collectively, these studies have begun to provide the direct, molecularly specific information necessary to empirically evaluate mechanistic descriptions of bio-related fuel electrochemistry and anode degradation.

CHAPTER 1

INTRODUCTION

Solid Oxide Fuel Cells and Biofuels

General Introduction

As global energy demands continue to rise, the need for economical, sustainable, clean, and high-performing alternatives to traditional petroleum-based energy conversion is also growing. While petroleum reserves will likely remain viable into the foreseeable future,[1, 2] several countries have begun implementing policies to reduce dependence on this nonrenewable resource,[3] inspired by the need for increased energy security as well as policies that aim to reduce carbon dioxide emissions.[4] Furthermore, while many developing countries will inevitably require increased energy consumption, many regions (particularly Latin America, the Caribbean, and Africa)[3, 5] are transitioning more directly to renewable energy generation to avoid some of the disadvantages that have historically underpinned growth in developed regions.

Significant, global advancements have been made in several alternative energy arenas that utilize solar, wind, geothermal, and biomass energy sources. Solar, wind, and bio-mass energy conversion has been led by China, the US, and Germany.[3, 5] However, solar and wind power outputs suffer from seasonal and diurnal variations, motivating investments in biomass energy resources.[6, 7] Some plans envision an optimal energy infrastructure that utilizes the combined advantages of the cheaper solar and wind resources with more stable bio-renewable energy reserves.[6, 7] Biogas (derived from

fermented biomass) in particular has contributed significantly to a rapidly expanding green energy market in the European Union,[5] often upgraded to "biomethane," which involves the removal of carbon dioxide.[6-8] Upgraded biomethane is particularly important within the transportation and natural gas sectors.[6, 8] For electricity generation, energy conversion through biogas occurs mostly through combustion in CHP power systems, providing electrical efficiencies of up to 48%.[7, 9]

Ultimately, technological advancements are needed to provide clean, economically viable, and efficient energy conversion. Continued breakthrough in every renewable energy sector will facilitate continued transition away from traditional petroleum feedstocks. Energy from bio-derived fuels in particular offers significant promise in meeting these objectives, but current combustive technologies limits the efficiency and versatility of these fuel sources. On the other hand, energy conversion from fuel cells can alleviate some of these concerns by directly converting chemical energy to electricity. Five major types exist, including proton exchange membrane (PEM) fuel cells, phosphoric acid fuel cells, alkaline fuel cells, molten carbonate fuel cells and solid oxide fuel cells.[10] The former three, however, are compatible with only a limited portfolio of fuels (usually hydrogen). PEM fuel cells in particular, while regarded as technologically matured over the others, suffers from poisoning by CO and relatively low efficiencies. Molten carbonate fuel cells offer higher efficiency and better fuel versatility, but suffer from electrolyte corrosion. On the other hand, Solid Oxide Fuel Cells (SOFCs) promise both higher efficiency and superior fuel versatility in electrochemical processes that directly convert chemical energy from bio-derived fuels to electricity. In the

remainder of this section, I will first briefly describe the architecture of SOFCs and provide an overview of the chemistry that occurs in these devices. I will then describe recent investigations describing practical concerns of integrating SOFCs in biogas production sites. Finally, I will describe some of the remaining challenges associated with long-term SOFC operation using biogas, and how my Ph.D. work provides critically-needed molecular insights into these challenges. The remainder of this chapter outlines the experimental techniques and strategies used in this work, as well as summary of this dissertation.

Solid Oxide Fuel Cells

Recently, high temperature SOFCs have attracted considerable interest because of their relatively high efficiencies (> 70% in CHP systems) and clean emissions.[10-13] Furthermore, and in contrast with other lower temperature fuel cells (including PEM fuel cells, phosphoric acid fuel cells, and alkaline fuel cells), SOFCs offer flexibility in accommodating a wide variety of hydrocarbons and alcohols, including bio-derived fuels such as biogas.[9, 10, 12-15]

An SOFC, or MEA (membrane electrode assembly) is comprised of an anode and cathode connected by an external circuit and separated by a nonporous, solid oxide electrolyte. A planar geometry is commonly utilized but tubular MEA designs are also being explored.[16] Additionally, the support layer providing the bulk of the cross sectional thickness can vary, with common configurations including electrolyte and anode-supported MEAs. In general, anode supported cells allow higher performance but are more prone to temperature-induced failure.

The overall processes that lead to the direct conversion of chemical energy to electrical energy in an SOFC are relatively simple. At the cathode, molecular oxygen is catalytically reduced to form oxide anions. Oxides then diffuse through the electrolyte and oxidize fuels at the anode to form products (generally water and/or carbon dioxide depending on the fuel feed) and electric current, which returns to the cathode (Figure 1.1). High operational temperatures (650 ºC – 800 °C) are needed to overcome high activation barriers associated with oxide reduction at the cathode[17] and transport (100 kJ/mol)[18, 19] through the electrolyte. In turn, these high operational temperatures contribute to the wide fuel versatility.

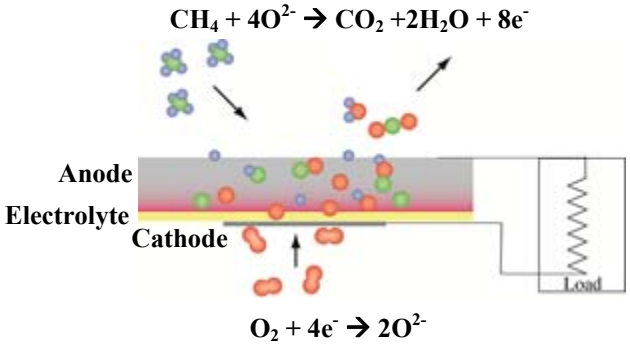

Figure 1.1. SOFC components including an anode support (~800 µm), cathode (~50 µm), and separating solid oxide electrolyte (10 µm). Hydrogen and numerous hydrocarbons and alcohols serve as viable feedstocks; in this example methane fuel is shown.

Each layer of the MEA (electrolyte and electrodes) must meet its own set of unique challenges. First, each layer must be thermally compatible at high temperatures to avoid delamination.[15, 18] Furthermore, the electrolyte must be electronically insulating while capable of conducting oxides through oxide vacancies in a ceramic structure.[15, 18] A zirconia lattice doped with 8% ytrrium (YSZ) has historically served as a superior oxide

conductor because of its stability as a cubic crystalline structure at the high temperatures required for oxide conduction,[11, 18, 19] though other alternative electrolytes have also been explored, including doped ceria and bismuth oxides.[11, 15, 18, 20-24] In addition, both electrodes must possess both high electronic *and* ionic conductivity, in addition to sufficient catalytic activity, while maintaining microstructural integrity at high temperatures and varying chemical environments. At the anode, these requirements are often met by mixing a metal catalyst with an electrolyte oxide conductor of choice (e.g. cermet). For example, anodes are traditionally composed of a relatively low-cost Ni-YSZ-pore cermet.[11, 15, 25] Of critical importance in cermet anodes is high connectivity within the ionic, electronic[11], and porous networks, as well as maximal triple-phase-boundary lengths (or TPBs),[14, 26] the interface shared by each of these three phases (Figure 1.2). Recently, some have investigated alternative anode materials including mixed electronic and ionic conductors (MEICs); a subset of such efforts include $Sr_{2-x}MM_oO_{6-y}$ (x=0.0,0.1,0.2, M = V, Fe, Mn, Mg, Cr, Co, Ni) double perovskites,[27,25, 28] $SrTiO_3$-based anodes,[29] among others.[11, 25, 30] This work is promising and avoids the challenges of maintaining TPB integrity, and though significant improvements have been made in terms of low catalytic activity and electronic conductivity, these alternative anodes remain an active area of research.[11] Nevertheless, Ni-based anodes remain the current state-of-the-art technology.[25, 26, 31]

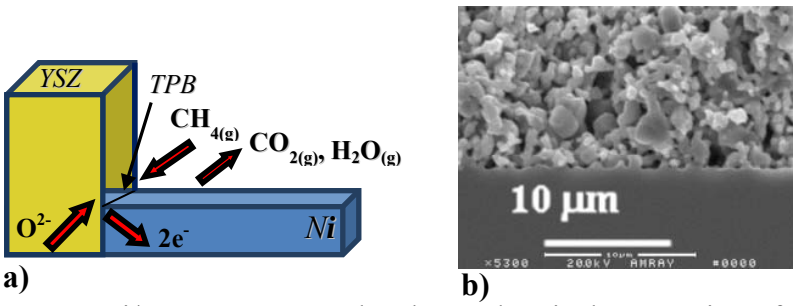

Figure 1.2. In a Ni/YSZ cermet anode, electrochemical conversion of methane fuel to exhaust and electricity at the triple phase boundary (TPB), the one-dimensional interface between YSZ, Ni, and pore (a). A representative image of a Ni/YSZ cermet structure is shown in (b).

Integrating Biogas with SOFCs

While biogas has been gaining momentum for electricity production through combustive generators,[7, 9, 32, 33] several studies[34-37] have begun assessing the viability of electricity generation through SOFCs for at least two reasons. First, SOFCs in general promise higher energy efficiency, cleaner emissions, and high tolerance to sulfur (often present in biogas).[7, 9, 35, 38] Gandiglio et al.[35] assessed a biogas-fed SOFC stack to be constructed in Torino, Italy, and used this as a basis for a larger scale, 100 kW model system. Both were to generate electricity and heat while sequestering CO_2 emissions to be fed into photo-bioreactors that grow algae, a biogas source also the subject of several studies.[4, 39, 40] These algae were in turn harvested to form "recycled" biogas. Overall modeled electrical efficiencies exceeded 52% (LHV). Second, biogas composition can vary widely (dependent on the source); major constituents are CH_4 and CO_2 but also contains trace (often deleterious) species.[9, 32, 41, 42] Raw biogas compositions can present difficulties for combustive technologies.[9, 43] Furthermore, trace impurities also pose difficulties, a challenge also for SOFC operation.[9, 35, 43, 44] In many current applications,

biogas is upgraded to "biomethane" by removing CO_2 and other species[6, 9], and some combustive technologies are known to fail with CO_2 compositions above 55%.[9, 11] On the other hand, biogas' low methane content is ideal for SOFC operation.[11, 34] Van erle and coworkers[34] modeled a small 1 kW system installed on a farm in Lully, Switzerland and demonstrated that maximal electrical efficiency was obtained for CO_2 contents near 60%, in fuels reformed with O_2. Papadam et al.[36] demonstrated that the most stable SOFC operation under a constant current for a combined total of 600 hours was achieved for CO_2 content near 50%.

Challenges

Despite the advantages of Ni-based anodes, numerous challenges persist, exacerbated by high operational temperatures. These disadvantages have been well-documented, and include nickel's susceptibility to oxidation from oxygenated species[45-47] and fouling by carbon.[48-51] These processes lead to degradation, including a loss of microstructural integrity (including loss of TPB boundaries, porosity, and ionic/electronic connectivity), and deactivation of the catalyst (including loss of surface area and metal dusting). Each of these processes can lead to power loss in an operational SOFC, and sometimes lead to irreversible degradation.

Nickel oxidation/reduction cycles in particular have been associated with irreversible cell degradation. Reduced nickel, when oxidized (to NiO), undergoes a 40% volume expansion.[45] Repeated oxidation and reduction cycles have been shown to lead to Ni particle agglomeration and loss of TPB lengths.[45] In the context of SOFC operation

with biogas, excessive CO_2 (or other added reformates such as O_2 or H_2O) mole fractions may plausibly present concerns for unwanted anode oxidation.

In addition, solid carbon formation (or 'coking') has been associated with irreversible power losses when SOFCs with Ni-based anodes are operated with carbon-containing fuels.[50, 52, 53] For example, from Reaction 1.1, methane can catalytically decompose on a nickel surface to form $C_{(s)}$ and $H_{2(g)}$:[54]

1.1 $CH_{4(g)} \rightarrow C_{(s)} + 2H_{2(g)}$

While nickel is very effective at catalyzing C-H bond cleavage, nickel itself serves as an attractive substrate for $C_{(s)}$ accumulation. This surface carbon can quickly form graphitic-like carbon structures that cover catalytic Ni sites and obstruct porous networks within the anode microstructure.[51] Eventually, these carbon structures can form carbon nanofibers associated with metal dusting (erosion of the Ni anode to Ni powder; nickel carbides have also been considered) and irreversible cell degradation.[51, 54, 55]

In biogas fuel mixtures, CO_2 can serve as a "natural" reformer that helps alleviate carbon formation that can be extensive under Reaction 1.1 in the absence of CO_2. In this dry reforming reaction, CH_4 and CO_2 react heterogeneously to form CO and H_2:[54]

1.2 $CH_{4(g)} + CO_{2(g)} \rightarrow 2CO_{(g)} + 2H_{2(g)}$

Increasing O:C ratios in fuel mixtures in general leads to less carbon formation, though operational temperatures also play a critical role. Lanzini et al.[54] demonstrated in TPO/mass spectroscopy studies that an equimolar CO_2:CH_4 mixture exposed to a Ni/YSZ anode supports at 800 °C led to only ~4% of the carbon compared to carbon deposited with plain CH_4. Increasing CO_2 mole fractions in the fuel stream further led to no

detectable carbon. Thus, in the context of preventing carbon-induced nickel degradation, increased CO_2 mole fractions in biogas is desirable.

Mechanistic descriptions of biogas fuel chemistry are tentative, largely because they rely upon indirect experimental measurements or theoretical models. TPO measurements such as those described above have provided important quantitative insights, but require that the device is cooled and disassembled.[54, 55] Using mass spectroscopy and isotopically-labeled reactants, Wei and Iglesia described the rate limiting step for the reforming reaction.[56] Hecht et al.[57] concluded from an innovative application of this technique that within a representative (but not *in operando*) Ni/YSZ anode, dry reforming was kinetically limited. Girona et al.[58] performed electrochemical measurements to provide input parameters needed for theoretical models that elucidated chemical mechanisms while Deutschmann and coworkers[59] modeled a related thermodynamically-consistent mechanistic scheme.

However, none of these techniques described above directly observe anode chemistry *in operando* and with molecular specificity—largely because of the challenges afforded by operational conditions. Yet direct, molecularly specific measurements are needed to provide a mechanistic description of the catalytic and electrochemical processes associated with electricity production. This information, in turn, can lead to better informed decisions regarding fuel and reformer compatibility, operational temperatures, current loads, component fabrication, and other operational and design parameters. This dissertation describes a suite of novel *in operando* optical observations coupled with electrochemical measurements collected during SOFC operation with

biogas and methane (as a reference case, providing additional insight). Together, these studies have begun to provide some of the first direct insights into mechanisms surrounding biogas fuel oxidation and Ni/YSZ anode degradation, particularly nickel oxidation and carbon growth.

Technical Background of *In-Operando* Techniques

High Temperature SOFC Assemblies

The *in operando* vibrational Raman experimental assembly depicted in Figure 1.3 was initially designed by Pomfret et al., and meets a demanding set of operational parameters.[60, 61] In particular, the SOFC MEA must be carefully pasted onto an alumina tube (inset) to maintain a tight seal between the anode (top layer) and cathode (bottom layer). Flowing over the anode surface is a fuel/carrier gas mixture (red arrows); over the cathode is an air (or oxygen/carrier gas mixture, blue arrows), and any mixing between each gas stream results in combustion-rather than electrochemical conversion. In addition, an adequate seal between the anode compartment, enclosed by a quartz tube, and the outside environment is maintained by a silicone stopper. The quartz tube provides access for a 488 nm Ar-ion laser beam that is focused onto the Ni/YSZ surface for Raman measurements.Surrounding the quartz tube is an insulated furnace that can bring MEA temperatures over 900 °C. A thin insulation piece is fitted over most of the quartz tube to retain sample heat while shielding the objective. An air stream continuously flows over the objective to provide cooling. The collaborative measurements collected at NRL utilized a very similar experimental rig,[62, 63] but with an alumina tube that replaced the

quartz tube, complete with a sapphire window on top. This new window allows for better transmission in the near and mid-IR, rather than visible, electromagnetic radiation.

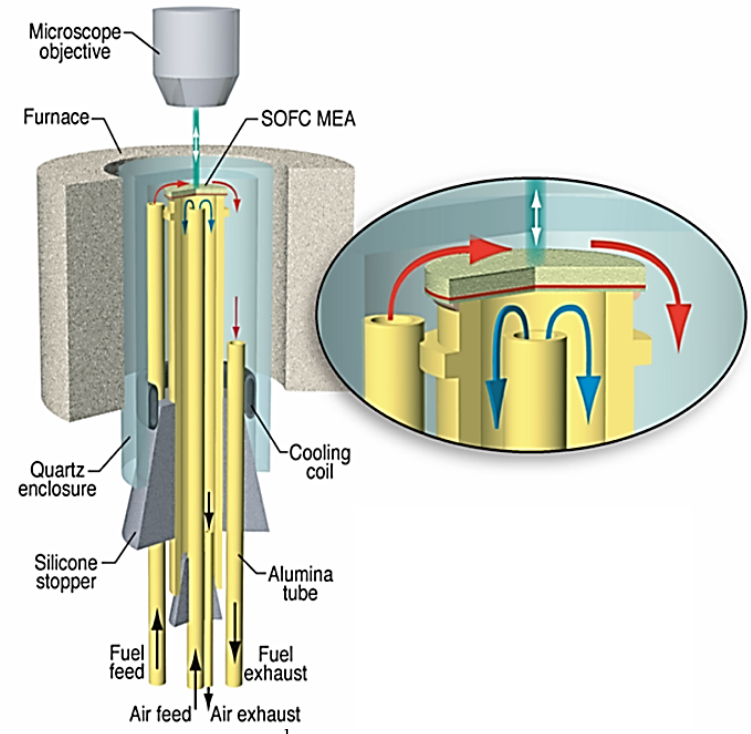

Figure 1.3. Schematic[1] of our Vibrational Raman assembly, used to test MEAs *in operando*.

Electrochemical Measurements

Linear Sweep Voltammetry. In LSV experiments described in this work, potential (or E) across an MEA is varied by a potentiostat at a constant rate (typically 0.1 *V*/s) from OCV (or the Nernstian potential between the anode and cathode) to (usually) 0 *V* relative to a reference electrode (Figure 1.4a).[64] At OCV, virtually no current passes through the potentiostat, and OCV reflects the difference in potential from each half cell, relative to an external reference electrode in the potentiostat. As MEA potential is decreased, cell

[1] Courtesy of Prof. Robert Kee, Dept. Mechanical Engineering, Colorado School of Mines

current increases, according to ohm's law. At 0 V, maximal current is measured (essentially short-circuited), referred to as I_{max}. In this work, any current applied to a cell (resulting in a potential smaller in magnitude relative to OCV) is sometimes referred to as polarization. Often, MEA power is also reported through $P = VI$. Typically, maximal power is reached at ~50% I_{max}.

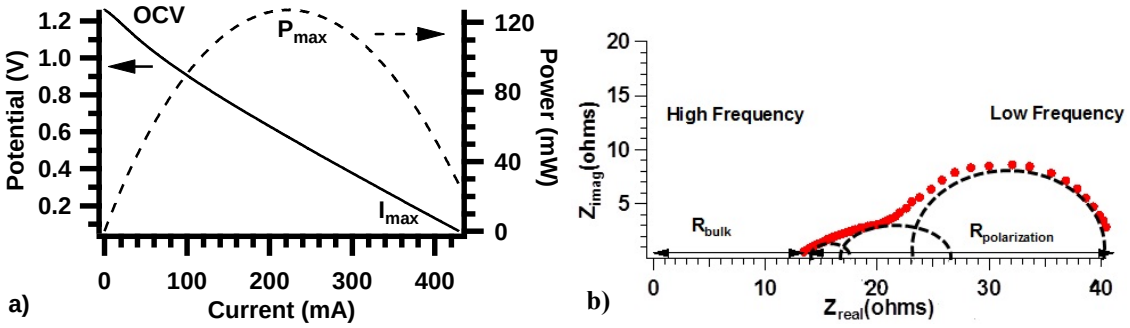

Figure 1.4. A LSV measurement taken under methane fuel at 800 °C and with an anode supported MEA (a). An EIS measurement taking under hydrogen fuel near 725 °C and with an electrolyte supported MEA (b).

Electrochemical Impedance Spectroscopy. EIS is useful for quantifying different contributions to MEA impedance that can reflect electrode structure and different electrochemical processes. EIS data measure the total impedance (resistance and capacitance) associated with chemical and mass transfer in operating SOFCs.[45, 64] EIS experiments involve sending low amplitude (in our experiments, generally ±10 mV), AC current to the cathode and monitoring any attenuation and phase shift of the current at the anode. Attenuation describes processes that contribute to the electrochemical impedance as a pure resistance (or Z_{real}) while the phase shift is the capacitive contribution (Z_{imag}) and is related to charge build up at various junctions (nominally TPBs) within the device.[45, 65]

Figure 1.4b shows impedance data acquired from an operating SOFC at ~725°C using H_2/Ar fuel at the anode and air at the cathode. Interpreting EIS data requires assuming a model circuit to describe the different processes occurring in the system.[45, 65] Each arc in the impedance spectrum represents electrochemical process(es) probed by different AC frequencies. Although the arcs often overlap, they can be deconvoluted using commercial software. The high frequency, low Z_{real} x-intercept (~14 Ω) corresponds to the pure ohmic resistance associated with the mass transport of oxides through the electrolyte.[45, 65] For this process, Z_{imag} is virtually zero. The first, high frequency arc is generally assigned to charge transfer reactions occurring at the cathode.[65] The middle arc corresponds to resistances associated with fuel activation and charge transfer at the anode; the low frequency arc corresponds to mass transport resistance primarily over and through porous electrode structures.[65] Often each of these impedance components grow in both dimensions as a cell ages and deteriorates; by assessing how impedance changes with fuel speciation, cell polarization, or materials, one can develop insight into mechanisms responsible for cell performance and degradation.[65, 66]

In Operando Vibrational Raman Spectroscopy

When light incident to a surface undergoes backscattering, it typically does so at a frequency identical to that of the incident light (Rayleigh scattering) but in Raman active species, incident light will couple with the electrons of the molecule/material and scatter at a frequency either lower (Stokes scattering) or higher (anti-Stokes scattering) than the incident frequency. Molecular and lattice vibrational modes are Raman active when a change in polarizability occurs as a result of motion along a particular vibrational

coordinate.[67] Plotting the intensity of the Stokes or anti-Stokes scattered light as a function of ($E_{inc} - E_{scattered}$) results in a vibrational spectrum of the material. In my studies, Raman spectroscopy has been particularly useful for monitoring the Stoke's shift of NiO (1100 cm^{-1}),[68] graphite (1350 to 2700 cm^{-1}, dependent on the structure)[69-71] and a likely Ni-CH_x intermediate (2920 cm^{-1}).[72]

Vibrational Raman spectra are measured *in operando* by focusing a 488 nm light source (8 – 25mW) through a long working distance (~10 mm) objective onto the Ni/YSZ anode surface of a working SOFC. These experiments provide the molecular specificity, spatial resolution (~1μm), and temporal resolution (at best ~1 s) needed to isolate and characterize chemical mechanisms responsible for fuel oxidation and device degradation, representing some of the first *in operando* spectroscopic measurements.[63, 73, 74]

In operando NIR Thermal Imaging
and FTIR Emission Spectroscopy

The elevated operational temperatures of our SOFCs (700 – 800 °C) result in a good deal of infrared radiation from a near-blackbody source. This radiation can be a liability for Raman experiments when the incident wavelength and subsequent Stokes signal must maintain sufficient strength against a large and rising background signal. (In our Raman experiments, this condition has motivated our use of a 488 nm excitation source, and also inspired investigations with a UV excitation source.) However, IR radiation from SOFCs has also provided a good deal of information with the strategic application of two novel techniques. The Near Infrared (NIR) thermal imaging techniques used in these studies here was developed at the NRL by Pomfret et al. was first used to

directly observe anode processes in operational SOFCs.[62] Similar experiments by others have used NIR thermal imaging to assess thermomechanical stability on a half-cell anode exposed to surrogate biogas[75] and cathodes of SOFCs (but with lower operating temperatures).[76] However, neither of these studies probed anode chemistry *in operando*. In my studies, a camera affixed with a broadband filter allows 720 nm to 1000 nm light to pass through to a SI-CCD detector, and records IR intensities as a function of time (> 4 Hz resolution) and space (~0.1 mm) across the entire MEA surface. The measured intensities are calibrated with a thermocouple to give a temperature resolution of ~0.1 °C. Further details regarding the development and integration of this technique can be found elsewhere.[62]

More recently, Pomfret et al. also used the infrared radiation in an innovative technique that measured the IR emission of hot gasses incident over the anode surface.[77] Liu and coworkers had implemented this technique several years prior in cathode studies although those studies were plagued by very high backgrounds and required extensive data processing in order to report on polarization dependent reduction of molecular oxygen.[78] In my studies at NRL, IR emission was measured by allowing IR radiation pass from the anode surface, through a sapphire window, and into an FTIR spectrometer. The IR source had been removed from the spectrometer to allow the IR emission from the MEA to pass through to a detector. This technique permitted the direct observation of gas phase and surface constituents in real time, with spectral resolution < 1 cm^{-1}.

Organization

The processes associated with SOFC operation with biogas are complex and difficult to ascertain without direct observation. The primary objective of this Ph.D. work is to use direct, non-intrusive optical and electrochemical techniques to describe processes and chemical mechanisms associated with electricity production and, more importantly, MEA degradation. Taken as a whole, this work has demonstrated the utility of direct observation in corroborating results from theoretical studies and other, indirect observation while highlighting the path forward in quantitatively validating model-based electrochemical oxidation mechanisms.

Chapter 2 presents efforts intended to bring familiarity with experimental techniques while improving data collection capabilities. This chapter describes experiments that utilized Raman spectroscopy and *ex situ* FEM imaging techniques to examine morphology changes in Ni/YSZ cermets exposed to alternating reducing and oxidizing environments. This work also discussed the possible mechanisms and kinetics regarding Ni oxidation and reduction, but remains highly speculative. This work did confirm, however, that Ni reduction under H_2 is much more rapid than Ni oxidation under O_2, and that repeated reduction/oxidation cycles leads to changes in the Ni/YSZ cermet microstructure. While the causes of deleterious Ni oxidation can vary widely, this work finds relevance in biogas fuel systems in which CO_2 is a "natural" reformer and in which air has also sometimes served as an additional reformer.[34, 54]

Chapters 3 and 4 describe experiments that combined Raman spectroscopy with chronopotentiometry to observe the electrochemical removal of carbon that had been

previously deposited (by CH_4) on the Ni/YSZ anode of an electrolyte-supported MEA. Chapter 2 demonstrates that within a pristine anode, virtually all carbon was electrochemically removed. This observation was supported by close correlation between an electrochemical equivalence point and a Raman spectroscopic equivalence point. As an MEA degraded, carbon still formed, but less of this carbon was "electrochemically accessible," perhaps indicating deterioration in TPBs. This hypothesis was supported by decreased correlation between the spectroscopic and electrochemical equivalence points. Chapter 3 further explores the mechanisms associated with MEA degradation during a chronopotentiometric experiment. Each chapter provided critical insights needed for subsequent investigations of SOFCs operating with biogas: 1) These studies provided a way to quantify "electrochemical accessible" carbon, or carbon near TPBs and 2) These studies described degradation mechanisms under lean or absent fuel conditions (particularly important under conditions of high current loads and low methane mole fractions in biogas fuels).

Chapter 5 describes experiments performed in collaboration with Prof. Josephine M. Hill (Dept. of Chemical and Petroleum Engineering, University of Calgary) and coworkers using a combination of Raman spectroscopy and OCV measurements. As in Chapters 2 and 3 Ni/YSZ anodes of operational SOFCs were pre-coked with CH_4, but in these studies carbon was removed by exposing the coked surface to Ar gas containing H_2O, CO_2, and O_2. Each of these three oxidants is a common CH_4 fuel reformer, and can be effective in reducing carbon formation during SOFC operation. These studies purposed to delineate carbon *removal* mechanisms by these reformers. This study showed

that carbon removal rates by each of the reformers under SOFC operational conditions followed the order: $H_2O > O_2 > CO_2$, and proposed a mechanistic explanation for these differences.

Chapters 6 and 7 describe observations of surrogate biogas and methane fuel chemistry during SOFC operation (Ni/YSZ-based anode supported cells). Observations from Vibrational Raman spectroscopy, FTIR emission spectroscopy, NIR thermal imaging, and electrochemical measurements each provide an internally-consistent mechanistic description of heterogeneous fuel reforming and electrochemical oxidation in two limiting cases: 1) neat CH_4 (diluted with Ar), and 2) 50% CH_4/50% CO_2 (diluted with Ar). These studies showed that mechanisms associated with carbon deposition and fuel oxidation are influenced strongly by operational temperature, fuel composition, and polarization. The mechanistic insights afforded by these studies also found support with other theoretical and experimental studies.

Chapters 2-7 have already appeared in press or have been submitted for publication. As such, some redundancy is present, especially in the introduction and experimental sections presented in each chapter. Furthermore, some chapters have experienced light editing to accommodate typographical errors and to bring clarity. Gas flow rates in chapters 3 and 4 were misreported in the published versions and have been corrected here. Additionally, some figure captions have been modified to clarify the vertical offset applied to some reported Raman signal intensities in Chapters 4 and 5. Finally, a parenthetical statement in Chapter 7 to detail the standard state equilibrium constant of reaction 7.3 has been added.

CHAPTER 2

IN SITU OPTICAL STUDIES OF OXIDATION KINETICS OF NI/YSZ CERMET ANODES

Contribution of Authors and Co-Authors

Manuscript in Chapter 2

Author: John D. Kirtley

Contributions: Conducted and led most experiments in this work (except FEM images), analyzed all data, wrote first draft, and contributed to subsequent editions.

Co-Author: Dr. Bryan C. Eigenbrodt

Contributions: Provided assistance in laboratory training and helpful conversations regarding experimental design.

Co-Author: Dr. Robert A. Walker

Contributions: Conceptualized experimental design, assisted with manuscript revisions.

Manuscript Information Page

John D. Kirtley, Bryan C. Eigenbrodt, Robert A. Walker
ECS Transactions
Status of Manuscript:
____ Prepared for submission to a peer-reviewed journal
____ Officially submitted to a peer-review journal
____ Accepted by a peer-reviewed journal
__x__ Published in a peer-reviewed journal

Published by © The Electrochemical Society
33 (40), 2011

Introduction

As the need for cleaner, more efficient and more sustainable sources of electricity continues to grow, solid oxide fuel cells (SOFCs) are attracting interest for a host of applications.[10, 11] Indeed, in combined heating and power systems SOFCs can operate with efficiencies approaching 70%, considerably higher than the 30-35% efficiencies achieved by traditional combustion engines.[11] Other advantages of SOFCs include a relatively simple construction from inexpensive materials, versatile fuel sources, few moving parts, and a scalable design.[17, 18]

An SOFC is comprised of an anode and cathode connected by an external circuit and separated by a nonporous, solid oxide electrolyte. SOFC operation begins with reduction of molecular oxygen at the cathode to form oxide anions. The ions diffuse through the electrolyte and oxidize fuels incident on the anode to form products (generally H_2O and/or CO_2 depending on the fuel feed). Electrons are collected and passed through a load before returning to the cathode to begin the cycle all over again (Figure 2.1). To work efficiently, SOFCs must operate at temperatures above 700 ºC to overcome large activation barriers associated with oxygen reduction at the cathode (223 kJ/mol) and oxide diffusion through the electrolyte (100 kJ/mol).[17, 18]

Limiting the utility of SOFCs is their tendency to suffer irreversible degradation and failure after extended use.[45] The potential sources of failure are many. The anode and/or the cathode can delaminate from the electrolyte, or current collecting leads can delaminate from the electrodes. Carbon containing fuels have the potential to form carbon deposits that occupy electrocatalytic sites on the anode restricting the ability of

the anode to catalyze fuel oxidation.[63] New materials can form at the boundaries between solid state components and these phases can limit electrochemical activity.[79] Because of the need to fully insulate operating SOFCs, identifying sources of SOFC degradation and failure represents a major challenge to fully understanding the *molecular* processes that occur *in situ* and in real time during normal operation. Traditional analytical methods have utilized *in situ* electrochemical methods, including voltammetry and impedance spectroscopy. However, these techniques only report on how well a device is operating, not on the species responsible for observed changes in performance.[63] *Ex situ* analyses, using scanning electron microscopy (SEM) imaging, X-ray photoelectron spectroscopy (XPS), and X-ray diffraction (XRD) can provide exceptional detail about the molecules and materials present on SOFC surfaces *only after the devices have been cooled and disassembled*. In order to fully understand and quantify the mechanisms responsible for SOFC operation and degradation, materials specific data need to be acquired *in situ* and in real time. We have recently developed methods that allow us to use vibrational Raman scattering to obtain molecularly specific information with temporal resolution ≤ 5 sec, and a spatial resolution of ~1 μm to explore changes on SOFC components in operating cells at temperatures up to 715 °C, ~100 °C higher than other recently published data using Raman spectroscopy.[61, 63, 80, 81] This ability has given us a unique opportunity to probe the chemistry that occurs in functioning SOFCs while simultaneously monitoring SOFC performance with traditional electrochemical tools to obtain a better understanding of specific chemical mechanisms that can affect electrochemical performance in SOFCs.

Experiments described in this work examine the oxidation and reduction behavior of Ni particles in Ni/YSZ ceramic-metal (cermet) composites. Ni/YSZ cermets are the most commonly used anode materials in SOFCs due to Ni's electrocatalytic[82] and conducting abilities. However, Ni is also susceptible to oxidation during SOFC operation.[83] Oxidation of the anode can lead to SOFC failure due to loss of catalytic activity, loss of conductivity, and volume expansion, resulting in decreased porosity and delamination.[84-86] Ni oxidation at high temperatures has been studied extensively, albeit indirectly, and rarely in the context of working SOFC devices. Nevertheless, oxidation of Ni/YSZ anodes is widely recognized as an important source of SOFC degradation.[45] Three possible mechanisms that can lead to Ni/YSZ anode oxidation include: 1) leakage of gaseous O_2 from the cathode to the anode, 2) water oxidation (present as a product and/or fuel reformer), and 3) high oxide concentrations at the anode due to either large overpotentials or a diluted fuel mixture.[45, 83, 86] In the studies described below, we use vibrational Raman scattering to monitor directly the *in situ* oxidation of Ni particles in Ni/YSZ cermets as a function of Ni particle size and gas phase conditions above the cermet material. The kinetic data are acquired with 5 s resolution and report on the relative intensity of the NiO vibrational band at ~1100 cm^{-1}. The kinetic data acquired from the Raman experiments are correlated with *ex situ* field emission microscopy (FEM) images acquired from samples subject to different reduction/oxidation cycling conditions.

Experimental

NiO/YSZ Sample Preparation

Five NiO/YSZ samples were prepared using a single method. Two important objectives in this experiment were to assess the impact of Ni particle size on oxidation rates and to determine if $H_2O_{(g)}$ could drive Ni oxidation. A given sample used three different Ni pastes with Ni grain sizes of 5-20 nm, 2-3 μm, and 3-7 μm (Alfa Aesar). Samples were prepared using a 66/33% (by mass) Ni/8%YSZ mixture (Tosoh), to which an organic ink vehicle (Fuel Cell Materials) was added to create a viscous paste. The 5-20 nm particles came with a thin NiO coating; the other two sizes were pure screened Ni particles. These three pastes were applied to a pressed polycrystalline YSZ disc (previously sintered at 1450 °C) as shown schematically in Figure 2.1. Each sample was then heated in a furnace with a 1 °C/min. ramp rate to 1350 °C, held at this temperature for 1 hour, and cooled at a rate of 1 °C/min. Because the sample was exposed to air during heat-up, each Ni/YSZ cermet was oxidized in the process as confirmed using vibrational Raman scattering.

Figure 2.1. Ni/YSZ sample schematic (25 mm diameter; ~90 μm thick).

Reduction/Oxidation Raman
Spectroscopy Experiment at 715 °C

The nickel reduction and oxidation kinetics of the first sample were measured at 715 °C with the assembly that is usually employed in working SOFC studies.[61] In this device, the sample was set over an alumina tube, cermet side up. A gas inlet near the sample guided reactant gas over the anode. Argon gas was forced up the alumina tube to provide a pressure balance on the opposite side of the sample. The sample was set inside a clear quartz tube; this assembly in turn was enclosed with a semi-cylindrical thermocouple-controlled furnace (Thermcraft) and wrapped with high-density insulation. A long-working distance objective (Leica) focused the 488 nm excitation light used in the Raman scattering experiments through the top of the quartz tube and onto the sample. After heating the sample to ~715 ºC, the reduction and oxidation kinetics of each sample having a different particle size were monitored using the intensity of the NiO Raman band at 1100 cm^{-1}. Following the cessation of growth in the NiO band intensity, samples were re-reduced and then exposed for up to 10 minutes to 4% humidified argon. The data presented below show that $H_2O_{(g)}$ at these temperatures did not lead to any observable oxidation of the Ni particles. Two reduction/oxidation cycles (using H_2/Ar and O_2/Ar) finished the sequence of experiments. The sample was cooled to room temperature at 1°C/min. under Ar gas (90 mL/min) to be tested by *ex situ* FEM to acquire images of the preserved, oxidized samples.

All Raman Measurements were made using an 8mW 488nm excitation source from an inVia Renishaw Raman microscope, with an approximate spot size of diameter 1μm. A long-working distance 50x lens was used for all Raman measurements. The

Stoke's shift in incident wavelength caused by symmetric vibrations of the NiO bond (near 1100 cm^{-1}), allowed us to determine the relative surface NiO concentration as a function of time (Figure 2.2).

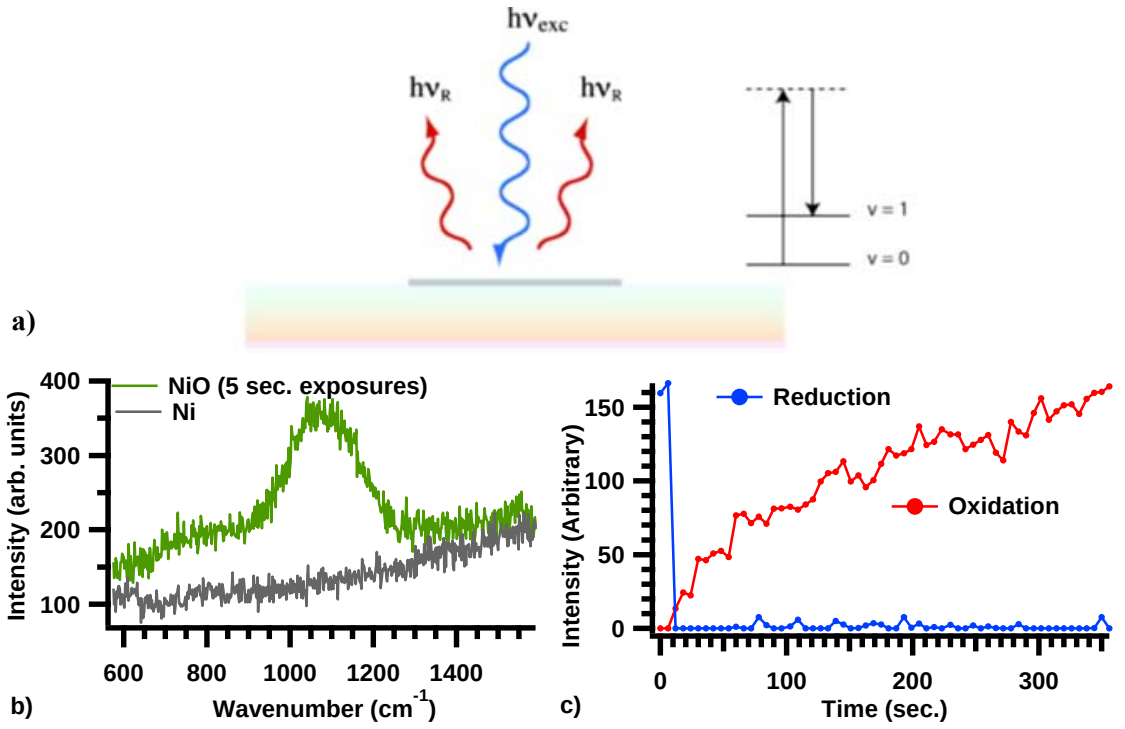

Figure 2.2: a) A schematic illustration showing the mechanism responsible for vibrational Raman scattering. In experiments described below $h\upsilon_{exc}$ is provided by an Ar^{+} laser and the back-scattered signal ($h\upsilon_{scatter}$) is collected with a long working distance microscope objective. b) Representative vibrational Raman spectra of NiO (green) and reduced, elemental Ni (gray). Spectra were acquired in 5 s intervals at a temperature of 715 ˚C, c) plot of relative NiO Raman vibrational peak intensities as a function of time. The data have been baseline connected to remove background from blackbody radiation.

FEM Imaging with Samples
Processed at 550 °C

The reduction and re-oxidation kinetics of four of the five prepared samples were tested at 550 °C using a Linkam heat stage to determine the effects of both water and oxygen as an oxidant; these samples were characterized *ex situ* using FEM. Each of the

four samples was subjected to one of four experimental procedures then characterized *ex situ* using FEM imaging:

- Test the Ni/YSZ sample as prepared.
- Heat to 550°C at 1 °C/min. under a constant flow of Ar gas (43 mL/min); reduce under Ar/H_2 gas (72 mL/min and 100 mL/min, respectively), and re-oxidize using Ar/O_2 gas (72 mL/min, 110 mL/min, respectively). Cool at 2 °C/min. under Ar gas (72 mL/min).
- Heat to 550 °C and reduce under the conditions described above. Expose to 86 sccm/min. humidified Ar, saturated at room temperature. Cool at 2 °C/min. under Ar gas (72 mL/min). The humidified Ar stream was created by bubbling the Ar carrier gas through a water reservoir at room temperature.
- Heat to 550 °C and repeat step 3, then re-reduce with Ar/H_2 gas (72 mL/min, 100 mL/min) and re-oxidize using Ar/O_2 gas (72 mL/min, 110 mL/min, respectively). Cool at 2 °C/min. under Ar gas (72 mL/min).

Results and Discussion

Oxidation by Molecular Oxygen

Figure 2.3 shows the peak intensity of the NiO band at 715 °C for the different sized Ni particle samples exposed to O_2/Ar (Figure 2.3a) and the same sized NiO samples exposed to H_2/Ar (Figure 2.3b). Several initial observations stand out: 1) the intensity of the NiO Raman peak increases as the sample is oxidized by O_2 at 715 °C; 2) the intensity of this peak decreases when the same (oxidized) sample is exposed to H_2 at 715 °C; 3)

oxidation occurs much more slowly (on the order of minutes) than reduction (in a matter of seconds); 4) nickel particle size (5-20 nm 2-3 μm, 3-7 μm) does not appear to significantly influence relative NiO Raman peak intensities (after base-line correction). Furthermore, after an abrupt initial rise, the oxidation kinetics appear to follow pseudo-first order reaction kinetics. Reduction occurs so quickly that fitting the data to a single, unique model is difficult.

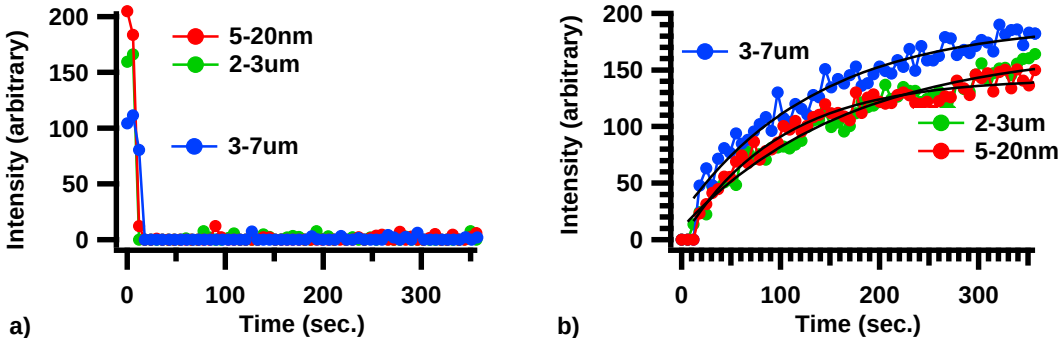

Figure 2.3. Oxidation and reduction kinetics of Ni and NiO at 715 ºC as a function of particle size prior to water exposure.

The oxidation and reduction of Ni and NiO, respectively, can be described by the simple rate laws shown below:

$$2.1 \qquad Ni_{(s)} + 1/2O_{2(g)} \xrightarrow{k_1} NiO_{(s)}$$

$$2.2 \qquad NiO_{(s)} + H_{2(g)} \xrightarrow{k_2} H_2O_{(g)} + Ni_{(s)}$$

To verify that experiments were carried out under pseudo-1st order conditions, oxygen and hydrogen partial pressures were varied by a factor of 3 with no measurable change observed in the oxidation/reduction kinetics. (Data not shown.) Within the pseudo-first order approximation, the differentiated rate laws can be expressed as follows:

2.3 $$\frac{d[NiO]}{dt} = (k_1 P_o)[NiO]$$

2.4 $$[NiO(t)] = Ni_o(1 - e^{-k1*Po*t}) \quad oxidation$$

2.5 $$-\frac{d[NiO]}{dt} = (k_2 P_H)[Ni]$$

2.6 $$[NiO(t)] = Ni_0(e^{-k2*PH*t}) \quad reduction$$

where k_1P_O and k_2P_H are the pseudo first-order rate constants and Ni_o is the amount of nickel originally present. Given the rapid reduction of NiO exposed to H_2 we are not able to accurately model the reduction kinetics measured in our experiments.

The kinetic behavior of nickel oxidation has been reported previously by Karmhag et al., who monitored mass uptake by a collection of 4 μm Ni particles using thermogravimetric analysis (TGA).[87] These authors observed exponential behavior in the measured isothermal oxidation rates. When fitting their data these authors used a model originally proposed by Carter (Equation 2.7) to account for the particulate nature of nickel and nickel oxide:[88]

2.7 $$t = \frac{r_o^2}{2(z-1)k_p}\left(z - (z-1)(1-x)^{\frac{2}{3}} - (1 + (z-1)x)^{\frac{2}{3}}\right)$$

Here, *t, ro, x,* and *kp* represent time, initial radius of nickel particle (reduced), fraction of particles that have oxidized, and rate constant, respectively. The last term, *z,* accounts for the relative volume expansion of Ni to NiO, reported to be 1.53.[88] This model assumes that the oxidation rate is limited by diffusion of oxygen through an outer oxide layer into the central nickel core. Experimental data followed this model at temperatures ≤ 400 ºC, but deviated significantly at higher temperatures due to particle agglomeration.

Because TGA measures for bulk mass changes, the data of Karmhag et al. reflect the oxidation kinetics of the entire bulk Ni sample.[87] In contrast, the vibrational Raman experiments described in this work are sensitive solely to surface oxidation. This distinction is apparent when comparing data from the two studies. While reported oxidation from TGA measurements typically occurred over a time scale of 11-12 hours, the Raman data reached asymptotic limits on a time scale of ~5-10 minutes. Samples used in experiments described in the work presented in this paper also differed significantly from those tested by Karmhag due to the presence of added YSZ particles. YSZ serves to conduct oxides and prevent excessive Ni particle sintering.[11, 18] In operating SOFCs the YSZ in the cermet anode also reduces the risk of delamination from the YSZ electrolyte.[11]

Particle agglomeration is thought to occur at temperatures between 350 ºC and 500 ºC, depending on the particle's surface morphology.[86] Because our Ni/YSZ samples have been sintered at 1350 ºC, we expect that some agglomeration has occurred even before testing. The pre-experiment sintering may explain why the relative oxidation rates of each of the three particles sizes were comparable (Figure 2.3a). Unlike other methods such as TGA, Raman spectroscopy will probe only the surface chemistry of metallic (reflecting) substrates.

Effects of Water on Oxidation Kinetics

The effects of water on SOFC electrode structure have been largely overlooked. Water is important in reforming hydrocarbon fuels for use in SOFCs, and is also an important component of SOFC exhaust.[85] To evaluate the effects of water on the gross

cermet anode structure and Ni oxidation kinetics, each Ni-YSZ cermet at 715 °C was exposed to 4% humidified Ar feed (saturated at ~22 °C), and Raman spectra were measured as a function of time. Kinetic data in Figure 2.4 show clearly that the all of the Ni/YSZ samples regardless of size did not undergo measurable oxidation when exposed to humidified Ar.

These observations stand in contrast to oxidation studies reported by Stathis et al., who also studied the impacts of water on SOFC Ni/YSZ anodes.[84] Again using TGA to study the susceptibility of pressed Ni/YSZ cermet samples to oxidation, these authors measured Ni oxidation kinetics using humidified inert gases. Oxidation of the anode was observed in several experiments using water baths heated to 40 ºC and 80 ºC, and passing the humidified gases across the anode. The sample was maintained at isotherms ranging from 800 ºC to 950 ºC. The authors found that the temperature of the water bath used to control P_{H2O} plays a significant role in the Ni oxidation rate: lower water vapor pressures resulted in much slower oxidation rates that were also less sensitive to the temperature of the anode. Despite the apparent contradictions between the results reported by Stathis et al., and the findings described in this work, several important considerations differentiate the two studies and these differences likely account for the apparent disagreement. These differences include 1) the TGA experiments of Stathis et al. measure bulk oxidation rates whereas the vibrational Raman experiments are sensitive primarily to surface oxidation; 2) a ~100 °C temperature difference exists between the highest temperature in the vibrational Raman experiments (715 °C) and the lowest temperature of the TGA experiments (800 °C); and 3) the TGA experiments were performed with water vapor

pressures that were 3 to 20 times higher than the vapor pressure used in the vibrational Raman measurements. In fact, given the strong sensitivity observed by Stathis et al. of Ni oxidation to water partial pressure *and* the higher temperatures at which the TGA experiments were performed, we propose that H_2O oxidation of Ni may pose a problem for Ni/YSZ anodes at higher temperatures and at high humidities but not at lower temperatures and H_2O vapor pressures more commonly found in SOFC reformers.

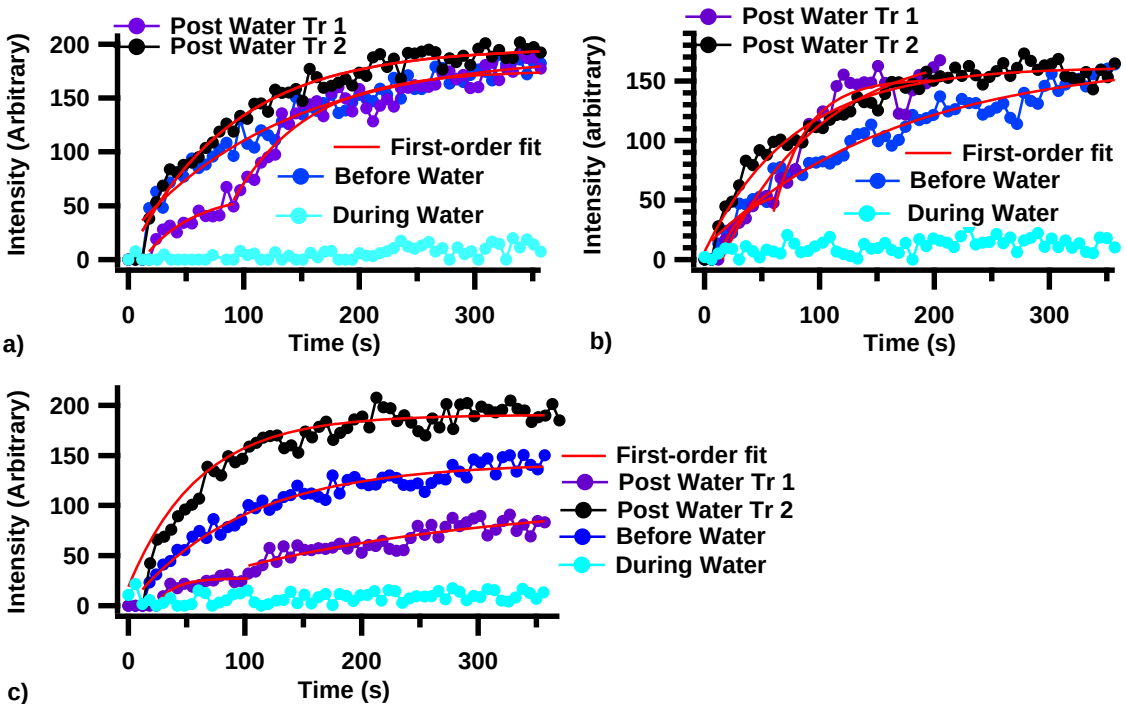

Figure 2.4. Kinetic traces measuring the rates of Ni oxidation for a) 3-7μm sized Ni particles; b) 2-3 μm sized Ni particles and c) 5-20nm sized Ni particles. Ni/YSZ experiment cycle including: 1) initial oxidation (black) and subsequent reduction, 2) exposure to water (light blue) and subsequent reduction, 3) first oxidation after water exposure (purple) and subsequent reduction, and 4) second oxidation after water exposure (blue).

Step 1				Step 2		
	Oxidation Before Water					
	Y_o	Ni_o	$k_1P_o(/10^2)$			
5-20 nm	142 +/- 6	126 +/- 6	1.02 +/- 0.09			
2-3 um	170 +/- 8	154 +/-7	0.60 +/- 0.06			
3-7 um	192 +/- 3	155 +/-4	0.74 +/- 0.07			
	Oxidation After Water Trial 1					
	Y_o	Ni_o	k_1P_o (/10^2)	Y_o	Ni_o	k_1P_o (/10^2)
5-20 nm	27 +/- 2	26 +/-4	6 +/- 1.5	107 +/-26	67 +/- 24	0.4 +/-0.3
2-3 um	58 +/- 6	57 +/-6	5 +/- 1.0	151+/-5	111+/-10	3.3+/-0.6
3-7 um	62 +/-20	54 +/-18	2 +/- 1.0	176 +/-4	121+/-6	1.5+/-0.2
	Oxidation After Water Trial 2					
	Y_o	Ni_o	k_1P_o (/10^2)			
5-20 nm	190 +/- 2	171 +/- 5	1.65 +/- 0.09			
2-3 um	162 +/- 2	156 +/- 4	1.29 +/- 0.07			
3-7 um	196 +/- 3	170 +/- 4	1.14 +/- 0.07			

Table 2.1 Psuedo-first order kinetic parameters of Ni oxidation as a function of particle size and water exposure, with approximate uncertainties reported. Each oxidation trace is fit to reflect Equation 2.4, where $y = Y_o - Ni_o e^{-k1Po*x}$. Ni_o refers to the Ni originally present (mole fraction), k_1P_o is a pseudo first-order rate constant (s^{-1}), and x refers to reaction time (s). Y_o is a fitting parameter intended to reflect Ni_o*1 in Equation 2.4 and should, in principle, equal Ni_o.

Oxidation data from our Raman spectra of the 3-7 μm sample (Figure 2.4a) reveal several additional insights into the effects of water on Ni oxidation. 1) Re-oxidation of the Ni/YSZ cermet immediately following exposure to water led to a slower *overall* oxidation rate compared to oxidation rates for the *same* sample not exposed to water. 2) The effects of water exposure on Ni particle oxidation are reversible and are apparent *only during the first oxidation cycle following exposure to water*. Subsequent re-oxidation cycles show kinetic behavior comparable to observations made prior to water exposure. Here, we note that the quantitative details of the kinetic behavior can vary significantly from sample to sample (composed of the same sized Ni particles), but for a given sample, the kinetic data reproduced to ± 20%. Often, the optical alignment and surface morphology can vary among experiments, leading to variability in overall Raman signal.

Also, we note that the results reported in Table 2.1 should be regarded as *relative* rate constants that fail to account for experimental variables such as exposed surface area, gas phase partial pressures, etc.

A closer look at Figure 2.4 reveals that oxidation kinetics for all samples appear to closely follow pseudo-first order behavior. As shown above in Equation 2.2, a pseudo-first order integrated rate law has two important parameters: Ni_o (amount of reduced Ni initially present) and k_1 (a relative rate constant). It is important to note that these rate constants are not absolute, but do provide an accurate comparison of the *relative* rates of each oxidation trial. Pseudo-first order fits are shown with the data in Figure 2.4 and the parameters are reported in Table 2.1. The initial oxidation observed for all three particle sizes follow a single first-order mechanism; the oxidation immediately following an exposure to water consistently follows a two-step process. Initial growth of the NiO vibrational signature in the initial post-water experiments appears to plateau after ~30 seconds before rising steeply again after ~90 seconds. The rate constant of the first step is, in all cases, larger than corresponding rate constant observed prior to water exposure. The single, pseudo-first order rate constant of the second oxidation cycle following water exposure returns to that same quantity observed initially prior to water exposure. This general behavior was observed for all Ni/YSZ samples regardless of particle size.

Correlating Results from Raman Spectroscopy with Surface Morphology using FEM Imaging

The vibrational Raman data reported in the previous section provide a quantitative description of nickel oxidation kinetics and the effects of water on these kinetics. However, these results do not provide any direct insight into the observed systematic

variations. Several factors likely influence the observed trends, particularly those associated with the effects of water exposure on subsequent oxidation kinetics. These factors include 1) a possible restructuring of the Ni/YSZ sample during water exposure and 2) water's chemical modification of surface site structure and oxide vacancy availability. To cultivate some insight into the kinetic data reported in Figure 2.4, we performed several reduction and oxidation experiments on identical Ni/YSZ samples similar to those used in the Ni oxidation studies at 715 °C and these samples were then analyzed using *ex situ* FEM imaging. Due to several technical difficulties, sample treatment for the FEM experiments was performed at 550 °C using an external, resistively heated stage. Several FEM images were taken after each step in the oxidation cycle (see experimental section) and the resulting images are displayed below in Figures 2.5 through 2.7.

Despite the cooler temperatures under which the Ni/YSZ cermets were treated prior to FEM analysis, the resulting images provide suggestive explanations of the trends observed from the Raman kinetic data. Close inspection of the images consistently indicate particle growth and possible surface roughening following oxidation at 550 ºC (Figures 2.5-2.7, panel b). Particle growth is thought to occur at temperatures between 350 ºC and 500 ºC, depending on the particle's surface morphology.[87] Although our Ni/YSZ samples were sintered at 1350 ºC, with significant agglomeration expected during sample preparation, additional agglomeration might be expected during oxidation at 550 °C. Images for the 3-7 μm (Figure 2.5), 2-3 μm (Figure 2.6) and 5-20 nm (Figure 2.7) particles consistently indicate particle growth following oxidation at 550 ºC. These

structural changes are evidenced by a loss of sharp facets characteristic of well-defined crystalline structures and an overall increase in the average dimensions of gross structural features. An important point to note is that this restructuring occurred even after the high temperatures experienced during sample preparation. Again noting that the relative volume expansion between Ni and NiO is about 1.53, some literature sources indicate that repeated reduction and oxidation cycling is not reversible and tends to promote particle agglomeration and less porosity in the cermet structure.[45, 46]

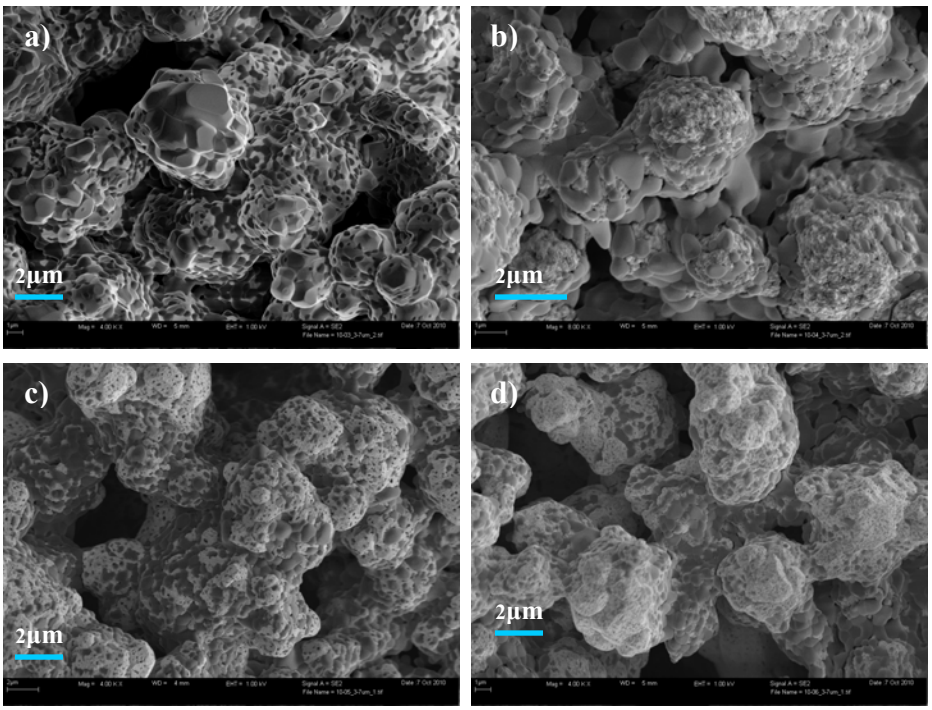

Figure 2.5. 3-7 µm Ni/YSZ a) as sintered, b) after one reduction/oxidation cycle, c) after exposure to humidified argon at 550 °C, and d) reduction/oxidation after water exposure.

To assess the effects of water (a byproduct in fuel cell operation) on the cermet structure and (by inference) Ni oxidation kinetics, each sample was exposed to 4% hydrated argon gas (saturated at ~22 °C) after reducing. Kinetic data from the vibrational

Raman scattering experiments shown in Figure 2.4 indicate clearly that little or no nickel oxidation occurred during exposure, regardless of particle size. Changes in the cermet structure following exposure to water are subtle, but still observable in tile (c) of Figures 2.5-2.7. Particle sizes are slightly larger but the biggest change is in the distribution of Ni and YSZ material in the cermet structure. An increased percentage of Ni (observed from the dark 'speckles') may also be deduced from all three sizes of Ni particles. These observations remain consistent with the ~50% relative volume expansion between Ni and NiO, a phenomena from which some researchers have suggested that repeated reduction and oxidation cycling leads to irreversible agglomeration and densification.[45, 46]

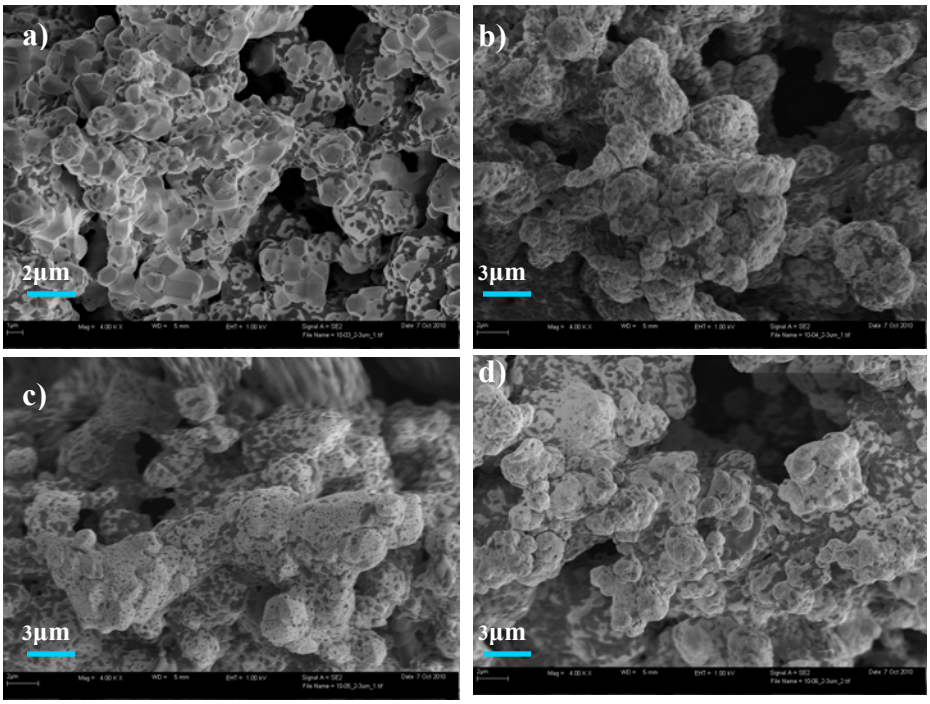

Figure 2.6. 2-3µm Ni/YSZ a) as sintered, b) after one reduction/oxidation cycle, c) after exposure to humidified argon at 550 °C, and d) reduction/oxidation after water exposure.

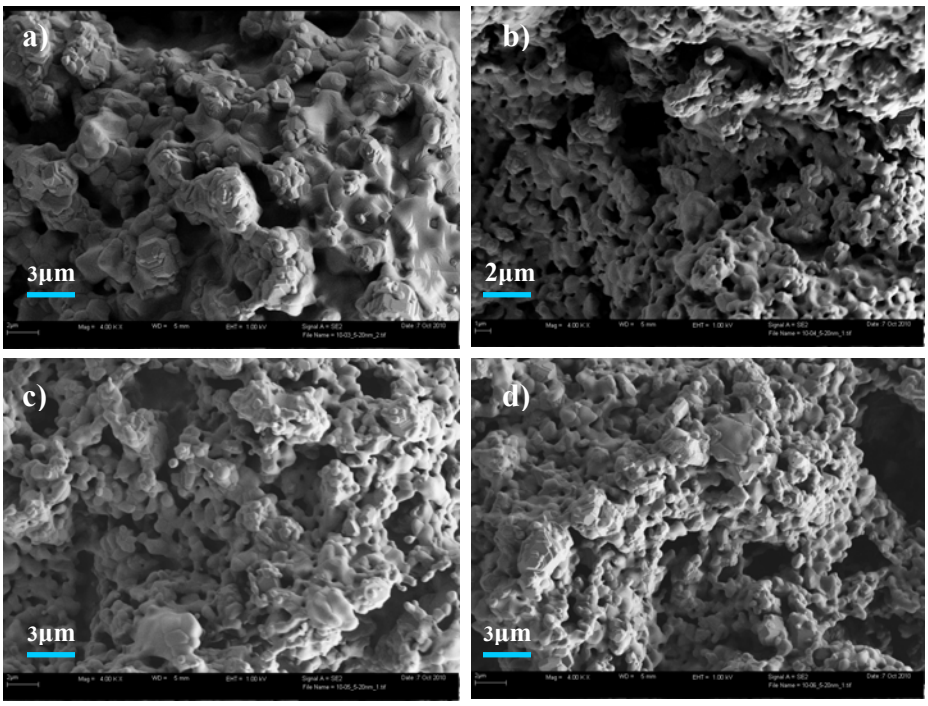

Figure 2.7. 5-20nm Ni/YSZ a) as sintered, b) after one reduction/oxidation cycle, c) after exposure to humidified argon at 550°C, and d) reduction/oxidation after water exposure.

Relating the structural changes in the Ni/YSZ cermets observed in the FEM images to the unusual, two-step kinetic data observed in Figure 2.4 requires some speculation. Tile (c) in Figures 2.5-2.7 shows a slight decrease in porosity following exposure of the reduced cermet to humidified Ar (regardless of Ni particle size). Consequently, in the subsequent re-oxidation we might expect the surface kinetics to proceed more slowly. However, from Table 2.1 and Figure 2.4, one sees that the first step of the observed two-step mechanism has a rate constant (k_1) ~2-8 times larger than that of the initial oxidation. This result implies that the exposure to water may sensitize sites on the Ni/YSZ surface making them more susceptible to subsequent oxidation opportunities. Whatever effects that H_2O has on the Ni/YSZ cermet, the consequences are reversible. The surfaces of the Ni/YSZ samples seen in tile (d) of Figures 2.5-2.7 underwent the

same procedure as those shown in tile (c), but in this case followed by an additional reduction and oxidation cycle. The surfaces shown in these images from each of the three particle sizes are indistinguishable from those observed immediately after the initial oxidation (tile b). This apparent reversibility remains consistent with previous observations made from our Raman data, which demonstrated, during the second post-water oxidation trial, a return of the oxidation kinetics to those seen before water exposure.

Conclusions

In situ vibrational Raman scattering was used to study Ni surface oxidation and NiO surface reduction kinetics in Ni/YSZ cermet anodes at two different temperatures, 550 °C and 715 °C. The oxidative behaviors of these samples were characterized as a function of Ni particle size and as a function of gas phase conditions. Ni/YSZ cermets used Ni particles having diameters of 5- 20 nm, 2-3 μm, and 3-7 μm. In general, NiO reduction occurred ~10 times faster than Ni oxidation. The smallest Ni particles (5-20 nm) showed the fastest initial oxidation rates. Although earlier literature reports of the ability of water vapor to oxidize Ni, repeated trials of each of our three particle sizes clearly indicate using Raman that no surface oxidation took place during the first ~10 minutes of exposure. However, exposure to water consistently changed the oxidation kinetics of reduced Ni particles during the first oxidation cycle following sample exposure to humidified Ar. The net result was a distinctive, two step oxidative process with each step following pseudo-first order kinetics. The origin of this behavior is uncertain, but water may play a role in both the restructuring of the Ni/YSZ cermet and in

blocking catalytic Ni oxidation sites during the initial re-oxidation process. After the water has been displaced, then cermet structure and oxidation rates return to their pre-water exposure conditions. Finally, the kinetics of the second oxidation strongly indicate reversibility: all three particle sizes appear to return to the pseudo-first order reaction rate observed initially before water exposure. While these ideas are admittedly speculative and lacking direct confirmation, consistency in the observed behavior and the potential consequences for SOFC component degradation motivates additional study using complementary methods.

CHAPTER 3

HIGH TEMPERATURE "SPECTROCHRONOPOTENTIOMETRY": CORRELATING ELECTROCHEMICAL PERFORMANCE WITH *IN SITU* RAMAN SPECTROSCOPY IN SOLID OXIDE FUEL CELLS

Contribution of Authors and Co-Authors

Manuscript in Chapter 3

Author: John D. Kirtley

Contributions: Led and conducted experiments in this work, analyzed data, wrote first draft, and contributed to subsequent editions.

Co-Author: David M. Halat

Contributions: Assisted in experimental setup, assisted in programming data processing software.

Co-Author: Melissa M. McIntyre

Contributions: Assisted in general laboratory needs.

Co-Author: Dr. Bryan C. Eigenbrodt

Contributions: Performed preliminary measurements and first conceptualized experiment, assisted in manuscript editing.

Co-Author: Dr. Robert A. Walker

Contributions: Assisted in experimental design, contributed to subsequent manuscript editions.

Manuscript Information Page

John D. Kirtley, David M. Halat, Melissa M. McIntyre, Bryan C. Eigenbrodt, Robert A. Walker
Analytical Chemistry
Status of Manuscript:
____ Prepared for submission to a peer-reviewed journal
____ Officially submitted to a peer-review journal
____ Accepted by a peer-reviewed journal
__x__ Published in a peer-reviewed journal

Published by © American Chemical Society,
84, 2012
http://pubs.acs.org/doi/abs/10.1021/ac301504g

Introduction

In the context of increasing global energy demands, solid oxide fuel cells (SOFCs) promise enhanced fuel economy, reduced emissions, and versatility in directly converting fuels into electricity. Fuel flexibility is a particularly attractive feature of SOFCs. Because these devices function at temperatures as high as 1000 °C, SOFCs can operate with a broad spectrum of fuels including H_2, syngas, methane, and higher MW hydrocarbon and bioderived species.[11] Furthermore, because SOFCs produce power through electrochemical conversion, these devices are more efficient than traditional, combustion-based sources of electricity. In combined heating and power applications, SOFCs have conversion efficiencies that approach 70%.[10, 12, 13, 89]

The general SOFC architecture consists of a porous ceramic − metallic (or cermet) composite cathode, a dense, ion-conducting, solid oxide electrolyte and a porous cermet anode. The cathode reduces molecular oxygen to form oxide anions. Oxide anions diffuse through the electrolyte to the anode where they react with fuel to produce products and electricity. Oxide diffusion through the electrolyte has an activation energy of ~100 kJ/mol necessitating high operating temperatures to ensure adequate oxide flux.[18, 19] Cermet materials are chosen for the cathode and anode based on their relatively large surface areas and three-phase boundaries, as well as on their ability to electrochemically catalyze oxygen reduction and fuel oxidation, respectively.

High operating temperatures also enhance processes responsible for device degradation. A primary degradation mechanism in SOFCs is the tendency of carbon-containing fuels to form solid carbon on the anode. Carbon deposition or “coking” blocks

active sites compromising overall SOFC efficiency and eventually causing device failure.[48, 90, 91] Nickel, the most common SOFC anode material, is an inexpensive, efficient electrocatalyst, but nickel's ability to promote hydrocarbon cracking also means that this anode material can accelerate carbon deposition. At the high temperatures required for SOFC operation, solvation of carbon into Ni particles becomes increasingly important as carbon nucleation and grain growth lead to anode disintegration, a process also referred to as "metal dusting."[11, 49, 55, 91-93]

Most evidence of carbon's deleterious effects on SOFC performance comes from coupling in situ electrochemical data with extensive ex situ measurements performed after the SOFC has been cooled to room temperature and disassembled.[52, 55, 86, 94, 95] While these studies have provided compelling motivation to operate SOFCs under conditions that minimize carbon formation, direct correlation between carbon deposition and electrochemical performance has remained poorly defined. In fact, several reports proposed that limited amounts of carbon on the anode actually improve SOFC operation by providing conducting pathways between regions of the anode that were otherwise electrically isolated.[96-98]

Recently, considerable effort has been dedicated to developing methods that can probe in situ the chemistry occurring in operating SOFCs. IR emission,[78] vibrational Raman scattering,[61, 80, 81, 99] near-IR imaging,[62, 76] and high-pressure X-ray photoelectron spectroscopy[100] have all been employed to examine chemical and structural changes that take place on SOFC components at temperatures up to 800 °C under a host of

environmental and electrochemical conditions. Of these techniques, vibrational Raman scattering has shown tremendous promise for identifying chemical species present in SOFCs operating with carbon-containing fuels.[52, 93] Raman scattering skirts the challenges posed by the significant blackbody emission emanating from SOFCs by measuring the Stokes-scattered light from visible or UV excitation sources. Furthermore, Raman spectra unambiguously identify molecular and materials species and their rates of their formation with temporal resolution of seconds or faster. Finally, by exploiting microscope optics, Raman spectra can explore with ~1 μm spatial resolution the distribution of electrochemically active regions across a functioning SOFC electrode.[101, 102]

In the absence of carefully measured standards, however, Raman spectroscopy remains a qualitative or, at best, a semiquantitative technique. Raman spectra can identify whether or not a species is present and that species' relative abundance. Line widths and spectral shifts provide clues about sample heterogeneity and local environment. Quantifying the amount of a species responsible for the measured Raman signal is much more challenging, as collection efficiency will depend sensitively on substrate microstructure, the distribution of Raman-active materials throughout the anode, and collection optics. This quantitative information, however, is exactly what is needed to develop models that predict conditions for stable, long-term SOFC operation. Experiments presented in this work couple quantitative time-resolved chronopotentiometry data with the relative intensities of features in vibrational Raman spectra to correlate SOFC performance with the amount of carbon formed on a Ni cermet

anode. When combined with FT-IR analyses of the SOFC exhaust, these experiments enable us to calculate the amount of carbon formed on stable, nondegraded anodes exposed to CH_4 and, more importantly, assign dramatic changes in SOFC electrochemical potential to different electrochemical oxidation reactions taking place, including carbon oxidation and subsequent Ni oxidation. As the cell degrades such quantitative correlations become more tenuous because changes in the carbon oxidation kinetics and electrochemical behavior imply that new, nonelectrochemical pathways may begin to play a role in graphite disappearance thereby limiting the utility of the chronopotentiometry data.

Spectrochronopotentiometry (SCP) -- coupling spectroscopic and electrochemical potential under constant current -- is a technique that has been used in diverse applications including (1) the determination of protein and enzyme oxidation−reduction potentials[103, 104] and (2) electrosynthesis of organic films.[105] In an SCP experiment, a spectroscopic observable is monitored concurrently with coulometric data that record the amount of charge required to drive a reaction of interest. Coupling optical spectroscopy with electrochemical data from SOFCs can provide detailed mechanistic information about how much of a specific species is being oxidized electrochemically on an anode.[106] As a tool for quantifying the chemistry occurring in extreme environments, SCP is underutilized in part because of the difficulty associated with making spectroscopic measurements under the conditions required for SOFC operation. The SCP experiments performed in this work demonstrate the promise of applying this proven analytical method to identify chemical and electrochemical correlations that historically have been

difficult to assign unambiguously. We anticipate that future studies leveraging these findings will lead to improved protocols and diagnostics that enable SOFCs to operate stably under conditions that promote efficient power production and device longevity.

Experimental Considerations

SOFC Construction

Our electrolyte-supported solid oxide fuel cells are assembled using procedures similar to those described previously.[52, 60, 61, 93] The membrane electrode assembly (MEA) consists of a 0.8 mm thick, 2.54 cm diameter YSZ (8 mol % yttria-stabilized zirconia) electrolyte with a 30 μm thick Ni−YSZ cermet anode on one side and a 30 μm thick LSM (lanthanum strontium manganite)−YSZ cermet cathode on the other side. In the experiments described below, a gold current collecting wire (Alfa Aesar) was applied to the anode using gold paste (Heraeus); a gold wire was attached to the cathode using platinum mesh (Alfa Aesar) and platinum paste (Heraeus). The fully constructed SOFC MEA was attached to an alumina tube (2.5 cm diam) using alumina paste, and the entire apparatus was placed inside of a quartz tube. A custom optical assembly was used to direct an incident 488 nm excitation source onto the MEA as described in previous reports.[52, 60]

Spectroscopic Measurements

Vibrational Raman spectra were acquired by collecting the backscattered light from the incident 488 nm Ar-ion excitation source (24 mW focused on the MEA surface by a 10× long-working distance objective). The collected Stokes radiation passed through

a notch filter (to remove the 488 nm Rayleigh scattered light) and was dispersed onto a CCD detector of a Renishaw InVia spectrometer.[52, 61, 93] When measuring kinetic data, spectra were acquired continuously with 10 s exposures per spectrum. Representative data showing Raman signals from graphite and NiO appear in Appendix A (Figure A.1). SOFC exhaust samples were also collected for FT-IR analysis. During an SCP experiment, exhaust was directed through a 10 cm gas cell chamber that had been purged previously with Ar. After exhaust had been flowing through the cell for ~90 s, the inlet and outlet ports were closed simultaneously. All spectra were acquired with 16 scans having 0.5 cm^{-1} resolution at room temperature and atmospheric pressure. Individual rovibrational lines in the IR spectra for both CO and CO_2 could be isolated for population analysis, and these absorption bands had line widths of 0.6 cm^{-1} fwhm (full width at half-maximum).

Electrochemical Diagnostic Measurements

Linear sweep voltammetry (LSV), electron impedance spectroscopy (EIS), and chronopotentiometry (CP) data were acquired with a Princeton Applied Research VersaStat MC. We note that voltammetry measurements were not carried out to maximum current (I_{max}) conditions in order to avoid an excessive electrochemical load on the cell and device damage. I_{max} was estimated by extrapolating the linear region of the voltammetry data to 0.0 V. Over the course of an experiment, I_{max} diminished due to cell degradation. Power production was determined by plotting the product of each $V-I$ ordered pair as a function of operating current. Voltammetry measurements served as benchmarks and were used to assess the device condition after each experiment that first

deposited and then oxidized away carbon on the Ni cermet anode. Fuel flows during all LSV benchmark tests were 18 mL/min H_2/106 mL/min Ar to the anode; 129 mL/min air to the cathode.

Electron impedance spectroscopic measurements were also performed after each trial to provide insight into molecular and structural sources of higher resistivities associated with cell degradation. An ac current of $\pm 10\ mV$ was applied from the cathode to the anode at rates of 100 000 − 0.1 Hz. The spectra were plotted in a Nyquist plot and modeled using ZSimpWin 3.22 software to quantify and associate different real and imaginary impedance elements of the SOFC. The particular electrochemical parameters (R_B, R_1, R_2, and R_3) measured after each trial can be found in Table 3.2.

Spectrochronopotentiometry

Spectrochronopotentiometry describes experiments that compare the intensities of different vibrational features in Raman spectra with electrochemical performance while a load is applied to the cell. Correlations between the relative amount of graphite present (measured in the Raman data) and the cell potential provide direct evidence of the chemical species responsible for electrochemical performance. Moreover, the relative amounts of $CO_{(g)}$ and $CO_{2(g)}$ in the exhaust provide direct correlation between applied current and oxidized carbon. This information quantified the amount of electrochemically accessible carbon deposited on the anode.

To perform an SCP measurement, the Ni−YSZ cermet anode was first exposed to dilute methane (20 mL/min CH_4, 106 mL/min Ar) for either 10 min (trials 1−5, 7) or 30 min (trial 6) at open circuit voltage (OCV). Applied currents were either 30 mA (~70%

I_{max}, trials 1−5) or 20 mA (~70% I_{max}, trials 6−7). Graphite formation during this period was monitored by recording the growth of the graphite "G" peak at 1556 cm^{-1}.[61, 93] After exposure to methane, the anode was kept at OCV under Ar (106 mL/min) while the lines were purged of residual methane. At the start of the SCP experiment, the cell was polarized to maintain a constant current and the voltage across the MEA was monitored. Raman spectra were acquired continuously with 10 s integrations. The SCP experiment was halted following a steep rise in the potential required to maintain constant current conditions. Following each SCP experiment, the anode was reconstituted with H_2 and benchmarked with EIS and LSV before further exposure to methane. This procedure generally led to residual carbon remaining on the anode (as evidenced in the Raman spectra), so following trials 3 and 4, the anode was briefly reoxidized with air before reconstitution with H_2. This procedure eliminated any residual carbon that had not been electrochemically oxidized. SCP experiments led to generally reproducible behavior with slight degradation in cell performance observed following each trial. An SCP experiment that was continued long after the elimination of electrochemically accessible graphite led to observable Ni oxidation and significant, irreversible degradation of the SOFC anode.

Results and Discussion

Evolution of the Raman Graphite Peak during Methane Exposure

The kinetics of graphite growth on Ni cermet anodes exposed to CH_4 can be seen in Figure 3.1, parts a and b. These data are representative of spectra acquired during methane exposure prior to each SCP experiment. Each spectrum in Figure 3.1a represents

a 10 s acquisition from the anode at a temperature of ~725 °C. The spectra show the growth of a single sharp feature at 1556 cm^{-1} assigned to the E_2g mode (also called the "G band") of highly ordered graphite.[70] In spectra acquired at later times, additional weak intensity occasionally appeared in a vibrational transition at ~1355 cm^{-1} and was assigned to the "D peak" associated with graphite having grain boundaries and/or site defects. Ratios of G/D intensities can be used to estimate the approximate size of graphite domains.[70, 107] After the graphite G peak intensity had reached its asymptotic limit after ~10 min, the graphite D peak is barely discernible leading to a lower G/D intensity ratio of ≥20. On the basis of work performed previously, this intensity ratio sets a lower limit on average domain size of ≥50 nm.[93, 108, 109]

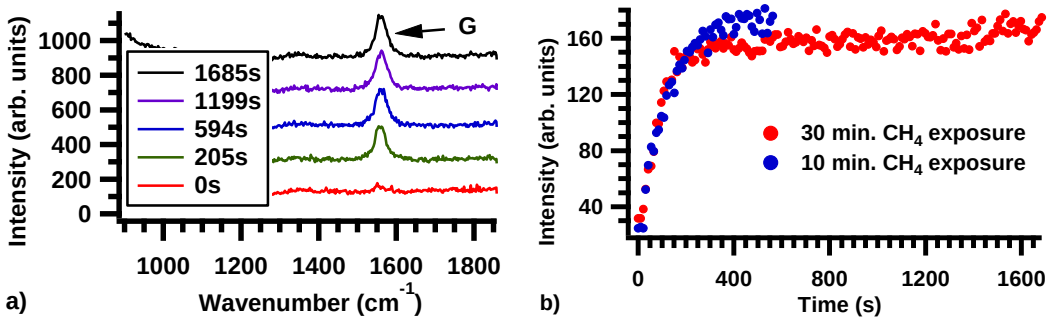

Figure 3.1. (a) Evolution of the Raman spectroscopic graphite peak (1556 cm^{-1}) during a 30 min CH_4 exposure at 20 mL/min (trial 6). Spectra have been displaced vertically for clarity. (b) Plot of 1556 cm^{-1} Raman peak intensity vs time during a 30 min exposure (red, trial 6) and 10 min exposure (blue, trial 4). All measurements were performed at 725 ± 5 °C.

Spectrochronopotentiometric Results

Allowing graphite to accumulate on the Ni−YSZ cermet anode held at OCV can reduce SOFC efficiency and ultimately damage cermet microstructure, but graphite formation also effectively loads the SOFC with a fuel reservoir that can be used to

produce electricity even in the absence of any additional fuel arriving with a carrier gas. SCP experiments performed in this work electrochemically oxidized graphite formed from methane by drawing a constant current from the cell while the anode was exposed to a flowing, inert Ar atmosphere. During this period of constant oxide flux through the electrolyte, we monitored the electrochemical potential across the MEA and acquired vibrational Raman spectra at 10 s intervals. Using FT-IR absorbance spectroscopy we also confirmed that CO_2 and CO were the primary (IR-active) species present in the anode exhaust.

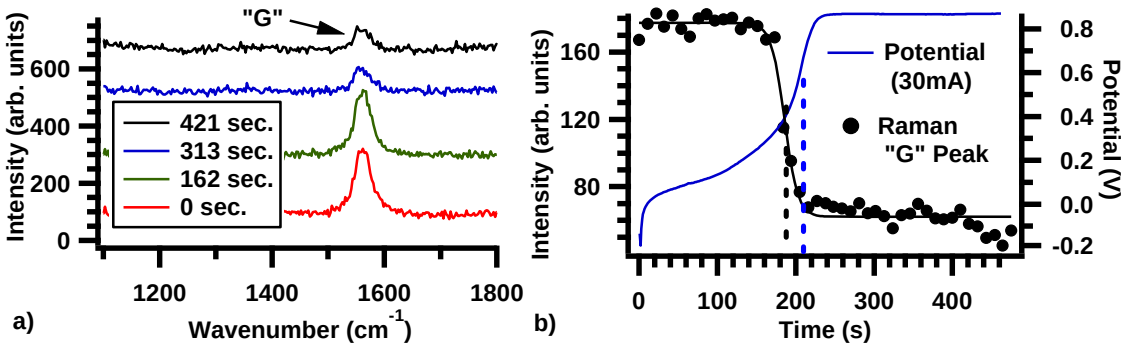

Figure 3.2. (a) Disappearance of the Raman spectroscopic "G" graphite peak (1556 cm^{-1}) following a 10 min CH_4 exposure, oxidized at 30 mA (trial 4). (b) Plot of the Raman "G" peak intensity (red dots) vs time during SCP oxidation and the Nernstian rise in cell potential (blue).

Figure 3.2a shows representative Raman spectra acquired while the MEA was polarized. Not surprisingly, the constant current (30.0 mA) and absence of a gas-phase fuel led to significant reduction of the G band intensity on a ~5 min. time scale. The residual intensity at 1556 cm^{-1} in the final spectrum (at 420 s) is assumed to result from graphite formed on parts of the anode surface that are not near the electrochemically active three phase boundary (TPB). Figure 3.2b shows the intensity of the G band and the

cell potential required to maintain a constant current. G band intensity diminished most rapidly between 2 and 4 min, passing through an equivalence point at 186 s. The cell potential required to maintain constant current was strongly anti-correlated with the G band signal: when the Raman spectra showed significant amounts of graphite on the anode, the cell potential rose only modestly, but the potential rose steeply when the graphite disappearance rate was fastest. The electrochemical equivalence point at 208 s lagged the spectroscopic equivalence point by less than 30 s, implying that the spectroscopic measurements were sensitive to most but not all of the electrochemically accessible graphite. (Note that temporal resolution of the spectroscopic data was ±10 s.) This assumption is reasonable given that Raman measurements cannot sample the entire depth of the 30 μm thick Ni−YSZ anode, while the chronopotentiometric data are sensitive to graphite at the three-phase boundary throughout the electrode's cermet structure. (In contrast, electrochemically inaccessible graphite describes graphite deposits that are oxidized by mechanisms that do not produce electricity for the device.) This result is general, and results from the sequence of the experiments conducted with a given SOFC are summarized in Table 3.1 and presented in full in Appendix A. In the discussion below, we propose that the electrochemical equivalence point coincides with a removal of graphite at the three-phase boundary, leading to the oxidation of Ni and the recombination of O^{2-} ions on the anode surface to form O_2 (and electricity). This molecular oxygen can (and does) oxidize residual, electrochemically inaccessible graphite.

Data in Figure 3.2 lead to several conclusions: (1) Graphite deposited by carbon-containing fuels on the SOFC anode can be removed electrochemically. Similar results have also been observed with thermal imaging methods.[62] (2) MEA cell potential during the SCP trial is anticorrelated to the relative amount of electrochemically accessible graphite. (3) The cermet anode is both ionically and electronically conductive from the anode/electrolyte junction to the anode/outer gas-phase interface. Assuming that the anti-correlated spectroscopic and electrochemical data in Figure 3.2b indicate that virtually all of the graphite is electrochemically accessible, the chronopotentiometry data can be used to quantify the amount of graphite originally formed on the anode provided that the relative amounts of CO_2 and CO produced by electrochemical oxidation are known. (See equations 3.1 and 3.2.)

3.1 $C_{(s)} + 2O^{2-} \rightarrow CO_{2(g)} + 4e^-$

3.2 $C_{(s)} + O^{2-} \rightarrow CO_{(g)} + 2e^-$

Quantifying the amount of CO_2 and CO produced in an SCP experiment required the use of FT-IR spectroscopy (Figure 3.3). The spectrum shows clear evidence of both CO (at lower frequency) and CO_2 (at higher frequency). Using IR absorption cross section information from the HITRAN database,[110] we calculate the amount of CO_2 and CO present in the SOFC exhaust to be 30 ± 2 mTorr of CO_2 and 50 ± 5 mTorr of CO. (Calculations used the absorption of the J = 2→3 line of the v = 0→1 transition of CO, and the J = 0→1 line of the antisymmetric stretch (ν3) of CO_2.) While the absolute amounts of CO_2 and CO change slightly from experiment to experiment, the ratio of CO_2 to CO remains relatively constant at the operational current density. On the basis of the

stoichiometry extrapolated from the gas-phase concentrations of CO_2 and CO, we estimate that 1.38 mol of O^{2-} was needed to oxidize 1.00 mol of $C_{(s)}$ (to form CO_2 and CO).

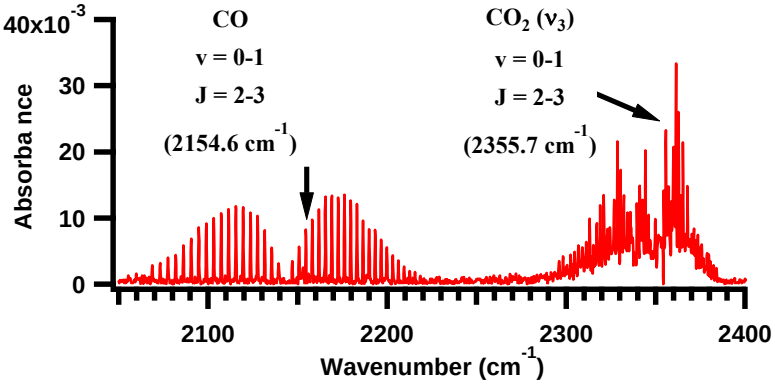

Figure 3.3. FT-IR spectrum of exhaust collected from the SOFC during an SCP experiment.

With the potentiometric data in Figure 3.2b and assuming a product ratio of 1.67 CO/CO_2 (from Figure 3.3), we calculate that exposing the Ni−YSZ anode at OCV to 104 mg ($8.7 \times 10{-}3$ mol) of CH_4 led to the formation of ~0.27 mg ($2.28 \times 10{-}5$ mol) of electrochemically accessible graphite. This result represents a lower limit to the amount of graphite present on the anode because neither Raman spectroscopy nor chronopotentiometric data can account for graphite formed on electrochemically isolated regions of the anode that are also spectroscopically inaccessible. We note that the amount of electrochemically accessible graphite that forms will depend sensitively on properties including anode microstructure, fuel composition, and device temperature, and these variables will continue to change as the SOFC cycles through successive trials. Data from

all seven experimental trials are summarized in Table 3.1. The actual data for each trial are presented in Appendix A as Figures A.1, a−g.

Data from trials 1−5 show that coupling in situ Raman spectroscopy with time-resolved chronopotentiometric data provides quantitative, chemically specific information that relates the chemical condition of an SOFC anode to its electrochemical performance. Numerous questions about this correlation remain, however, including (1) what is the chemical significance of the steep rise in cell potential observed in an SCP experiment; (2) does the amount of electrochemically accessible carbon depend on the duration of methane exposure; (3) does correlation between spectroscopic and electrochemical equivalence points depend on exposure time; (4) does prolonged MEA polarization lead to Ni oxidation that is detectable both electrochemically and spectroscopically?

Tr.	CH_4 exposure (min)	CH_4 delivered to anode ($x10^{-3}$mol)	electrochem. equiv. pt (s)	raman equiv. pt. (s)	ΔT (echem-raman equivalence pt.) (s)	electrochemically accessible C_s ($x10^{-5}$ mol)	% recovered C_s
1	10	~8.7	240	218	22	2.63	0.30%
2	10	~8.7	169	150	19	1.85	0.21%
3	10	~8.7	156	123	33	1.71	0.20%
4	10	~8.7	208	186	22	2.28	0.26%
5	10	~8.7	169	156	13	1.85	0.21%
6	30	~26	216	258	-42	1.58	0.06%
7*	10	~8.7	4	173	-169	.03	0.003%
						av. (1-5)	0.24%
						SD (1-5)	0.04%

Table 3.1. Representative graphite deposition and oxidation data from potentiometry and spectroscopic measurements. All equivalence points were determined by derivative plots of their respective data sets. *Trials 6-7 were performed after benchmark electrochemical data showed clear evidence of irreversible degradation. Data from Trials 6- 7 are not included in reported averages.

To address the first question, we performed an experiment similar to the SCP experiment but with molecular hydrogen as the only fuel. In this experiment, the cell was

polarized to operate at 70% of I_{max} as H_2 was being supplied to the anode. After ensuring stable operation for several minutes, the hydrogen supply was turned off and the cell remained polarized. Time was required for residual H_2 to clear the lines, but eventually, the voltage required to maintain constant current rose by 0.8−0.9 V. Given the absence of any other oxidizable species capable of being oxidized, we assign this jump in cell potential to the onset of Ni oxidation (eq 3.3). Because Ni oxidation presumably begins initially at the anode electrolyte boundary, this process is not immediately observable in the Raman spectra, with an ~40 s lag between the electrochemical equivalence point and the first appearance of a vibrational feature assigned to NiO in the spectra. Prolonged operation of the SOFC in the absence of H_2 leads to a second steep rise in cell potential (of ~1.2 V) that we assign to a loss of electronic conductivity through the anode (due to extensive NiO formation) and a resulting recombination of O^{2-} according to eq 3.4. Data for this experiment are shown in Figure A.2 in Appendix A.

3.3 $Ni_{(s)} + O^{2-} \rightarrow NiO_{(s)} + 2e^-$

3.4 $2O^{2-} \rightarrow O_{2(g)} + 4e^-$

Two important points are worth noting. First, in order for SOFC to remain polarized, oxidation must occur at the anode current collector. Consequently, we propose that the anode retains ionic connectivity from the electrolyte to the current collector so that equation 3.4 can continue to accommodate the forced polarization. Second, equation 3.4 provides a source of O_2 on the anode side of the SOFC MEA. This molecular oxygen can diffuse out of the anode and be carried away by the exhaust. However, the molecular oxygen can also chemically oxidize graphite that remains on the anode but is not

electrochemically accessible. Chemical oxidation of graphite to form CO and CO_2 provides an additional mechanism that could lead to further disappearance of spectroscopic graphite signals that do not correlate directly with the chronopotentiometry data. To summarize these SCP results acquired with H_2, the first steep rise in cell potential required to maintain constant current is assigned to the electrochemical oxidation of Ni in the anode; the second steep rise is assigned to a loss of electronic conductivity at the electrolyte−anode boundary and the resulting recombination of O^{2-} at the anode current collector.

To assess the effects of prolonged MEA exposure to methane at OCV, we performed an SCP measurement after 30 min of CH_4 exposure. These data are reported as trial 6 in Table 3.1. Graphite growth was again measured spectroscopically, and after 30 min, the fuel supply was shut off and the SCP measurement began. Kinetic data characterizing graphite growth are shown in Figure 3.1. Because graphite growth kinetics during the 30 min exposure closely follow those during the 10 min exposures and the maximum graphite signal observed spectroscopically is virtually equivalent for the 10 and 30 min exposures (Figure 3.1b), we conclude that the detected spectroscopic signals represent a saturated limit from the near-surface region of the anode probed in the Raman experiment.

As with the shorter exposure experiments, following methane exposure the MEA was polarized to maintain constant current (20 mA) corresponding to ~70% of I_{max}. The spectroscopic and electrochemical data qualitatively resemble results from the shorter exposure experiments, but several important differences also stand out (Figure 3.4). As

before, polarizing the cell leads to a diminishment of the Raman graphite signal and a corresponding rise in cell voltage under constant current operation. Again, the spectroscopic and electrochemical data pass through correlated equivalence points. In contrast, however, the electrochemical equivalence point (216 s) leads the spectroscopic equivalence point (258 s). A point also worth noting is that these equivalence points are not as well-defined as in earlier trials. The cell potential begins to rise steeply at early times meaning that the chemistry responsible for electrochemical oxidation must overcome a larger ohmic resistance.

After the first spectroscopic equivalence point, we observe a qualitative change in the rate of graphite loss based on the Raman data. The spectroscopic graphite signal continues to decrease monotonically from ∼500 to ∼1100 s. During this 10 min window, the cell voltage required to maintain constant current operation hovers between +0.9 and +0.8 *V*. Finally, when the last of the graphite disappears, the cell voltage again rises steeply at 1100 s, coinciding with continued growth of a vibrational band in the Raman spectrum at 1070 cm^{-1} assigned to NiO. Several hypotheses could explain these observations, although the SCP measurements cannot differentiate between them. One explanation for the continued loss of graphite after the steep rise in cell voltage is that, in addition to oxidizing Ni to form NiO, oxide ions are also recombining directly to form molecular oxygen (O_2) and electricity (after 216 s). As noted above, molecular oxygen will react with graphite at these temperatures to form CO_2. A changing P_{CO2} will change the system's reaction quotient and, correspondingly, measured cell potential. A second explanation is that, as Ni begins to oxidize, the accompanying 40% lattice expansion will

bring particles in the anode microstructure into contact with carbon deposits that have not previously been electrochemically accessible.[45, 88] This behavior would reduce the overall cell voltage as both Ni and carbon oxidation would contribute to the electrochemical cell potential.

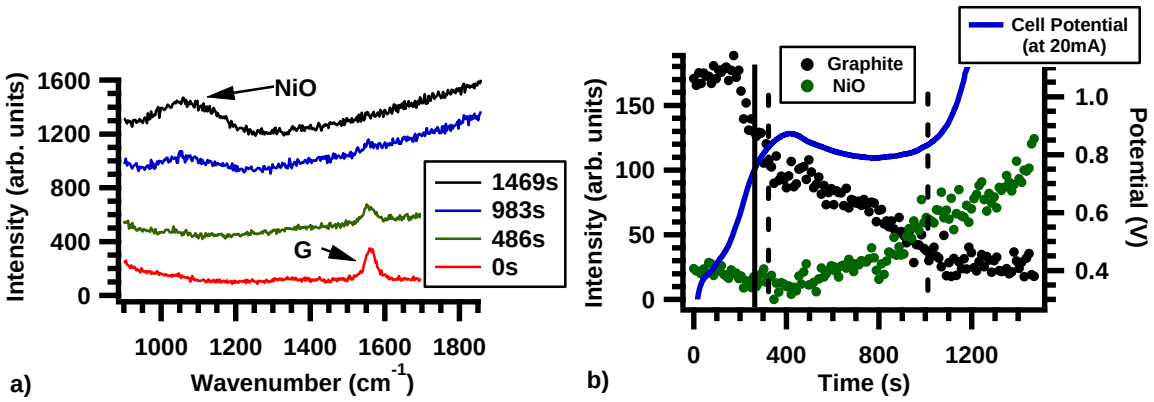

Figure 3.4. (a) Disappearance of the Raman graphite "G" peak (1556 cm^{-1}) following a 30 min CH_4 exposure and polarizing the SOFC to draw 20 mA (trial 6). Note the growth of NiO at ~1060 cm^{-1}. (b) Graphite peak intensity (black) and NiO peak intensity (green) vs time, correlated with a rise in cell potential (blue).

Continued operation of the SOFC leads to a second steep equivalence point (at 1165 s) that coincides with the strong growth of a NiO signature in the Raman spectra. Again, drawing from the H_2 SCP data, this second equivalence point is assigned a new mechanism responsible for current generation, namely, a large-scale loss of ionic conductivity between the electrolyte and the anode leading to the recombination of O^{2-} at the anode current collector to produce O_2 on the anode side of the MEA.

Taken together, SCP data from trials 1−6 can be used to construct an internally consistent description of how carbon deposits on Ni−YSZ cermet anodes impact SOFC performance and how changes in cell potential reflect changes in the mechanisms responsible for electrochemical power production. At times prior to the first equivalence

points – spectroscopic and electrochemical -- graphite is electrochemically oxidized. This claim is supported by the constant graphite signal in the Raman spectra coupled with the gently rising cell potential. The spectroscopic and electrochemical equivalence points remain closely correlated throughout the early trials, and their appearance signifies an SOFC anode that has not suffered significant degradation. At later times (and at higher cell potentials), electrochemical Ni oxidation is the primary reaction responsible for observed device behavior, although generation of O_2 cannot be ruled out. When electrical connectivity between the anode and electrolyte is lost (due to NiO growth at the anode/electrolyte boundary), the requirement of constant current forces O^{2-} to recombine exclusively as molecular oxygen at the anode current collector.

Following trial 6 and the complete oxidation of the anode we reconstituted the anode with dilute H_2 (in Ar) and performed one additional 10 min SCP experiment (trial 7). Graphite growth kinetics during exposure was comparable to those shown in Figure 3.2, and the terminal graphite intensity implied that similar amounts of carbon deposited on the anode. Data from trial 7 are shown in Figure 3.5 and appear qualitatively different from earlier SCP experiments. Two observations in particular stand out: First, the cell potential required to operate at constant current immediately climbed above 1.0 *V* without any apparent electrochemical equivalence point. This result implies that the cermet TPB had been severely compromised and that carbon deposited on the anode could no longer be electrochemically oxidized. The second observation is related to the first. Spectroscopic data show that graphite disappeared almost monotonically after the first minute of the SCP measurement. This behavior contrasts with the sigmoidal type

decrease in Raman intensity observed in earlier trials. Because the spectroscopic intensity of the graphite peak is no longer correlated with electrochemical performance of the cell, we propose that the carbon disappears through mechanisms not directly related to electrochemical oxidation. Related electrochemical impedance measurements described below also corroborate that the anode that has suffered significant degradation in performance compared to earlier trials. These results support previous ex situ studies that have shown how repeated oxidation and reduction of the Ni−YSZ cermet leads to significant agglomeration of Ni particles, a loss of overall three-phase boundary, and delamination from the underlying electrolyte.[45, 46, 84, 108]

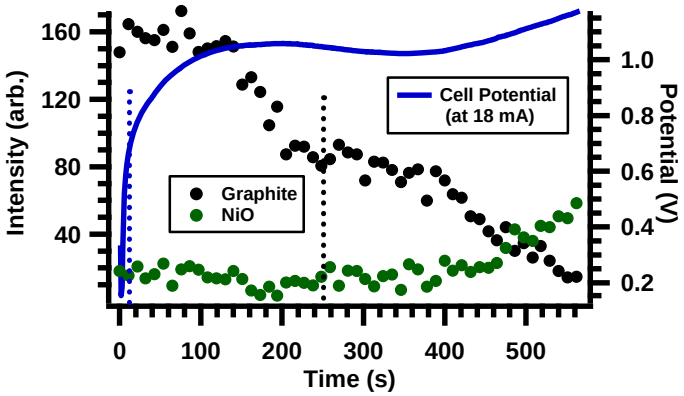

Figure 3.5. SCP data (trial 7) from a 10 min exposure to methane following electrochemical oxidation and reconstitution of the Ni cermet anode.

Electrochemical Diagnostics of MEA Degradation

Electrochemical evidence of anode degradation can be observed in the LSV and EIS acquired after each SCP trial (using H_2 as the fuel). These measurements provide a crucial link between the changes in composition and operating conditions following an SCP trial and the resulting consequences on device efficiency and durability.

Specifically, the benchmark H_2 diagnostics measured after each SCP trial provide quantitative information about whether initial cell performance can be recovered or if the carbon accumulation/electrochemical oxidation cycles lead to irreversible electrode degradation. Repeated cycling of the anode through SCP experiments can change anode microstructure as well as ionic conducting continuity across the electrolyte/anode interface. These changes will reflect themselves in the SOFC's overall ability to produce power through electrochemical oxidation (measured in LSV plots) and overall device impedance (measured in EIS data).

Following each SCP experiment, the anode was reconstituted with dilute H_2 (in Ar) and benchmark experiments were run using H_2 as the fuel. These repeated measurements enabled us to monitor the condition of the SOFC as the trials progressed. The LSV data (Figure 3.6a) show consistently diminishing electrochemical performance following each trial. Similarly, the corresponding impedance measurements (Figure 3.6b) similarly show significant increases both in bulk resistance (R_B) and polarization resistance (R_p). R_B describes oxide transport through the electrolyte and was approximately constant between trials 1 and 5, but following trial 6, R_B increased significantly, a result that can arise from partial delamination of the electrodes from the electrolyte. R_p is modeled with three RC circuits in series.[45, 93] Through the first five trials, R_1 (at high frequency) and R_3 (at low frequency) remain relatively constant, but R_2 rises consistently after every trial and becomes much more pronounced after trials 5 and 6. Following convention, we assign R_1 to cathodic charge transfer and R_3 to mass transport phenomena.[65, 101] R_2 is generally associated with anode processes including fuel

activation and charge transfer at the Ni/YSZ TPB.[65] The impedance data imply that, following each trial, fuel activation and charge transfer at the anode become increasingly difficult. Previous studies have shown how multiple oxidation/reduction cycles of Ni can lead to significant geometric changes and subsequent loss in catalytic activity.[87, 88, 91, 108] We propose that the growth of R_2 reflects a steady loss of TPB and Ni surface area as anode particles agglomerate. The effects of electrochemical oxidation on anode performance observed in the SCP measurements also manifest themselves clearly in the EIS data. Specifically, following the 30 min exposure and anode oxidation in trial 6, R_2 and R_3 both rise by ~10 Ω, implying that Ni oxidation leads to significant restructuring of the cermet microstructure.

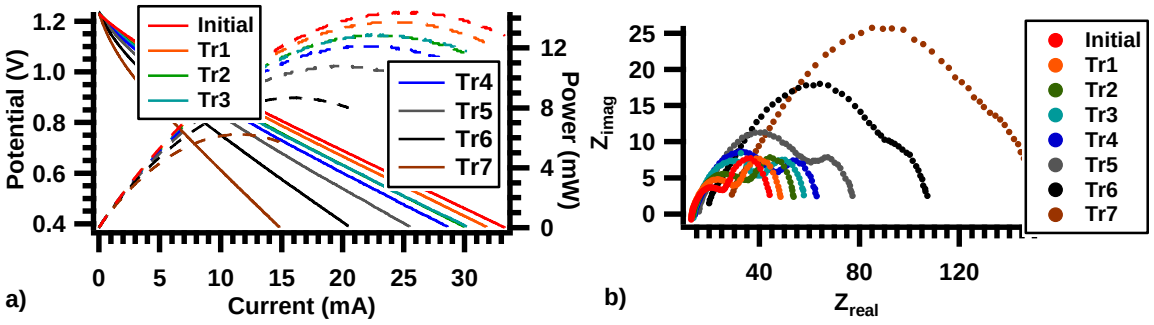

Figure 3.6. (a) Evaluation of SOFC performance with hydrogen fuel using LSV following each SCP experiment. The LSV data show a consistent drop in MEA performance following each trial. Voltammetry data are shown as solid lines, power as dashed lines. (b) Impedance data acquired with H_2 following each SCP experiment. Data were fit to a resistance (R_B) (a). Insight into mechanisms why are suggested by the EIS spectra in the Nyquist plot (b).

Conclusions

Direct correlation of SOFC electrochemical performance with in situ spectroscopic data has enabled chronopotentiometry experiments to quantify the amount

of electrochemically accessible carbon that accumulates on the Ni−YSZ cermet anodes of stable, nondegraded SOFCs operating at 725 °C. Vibrational Raman spectroscopy identifies the carbon formed from dry methane as highly ordered graphite. Specific findings include (1) increasing exposure time leads to proportionately less electrochemically accessible carbon (as reported in Table 3.2); (2) accumulated graphite can be used as a fuel allowing an SOFC to operate stably and reversibly; (3) excessive carbon formation and subsequent electrochemical oxidation results in significant and irreversible damage to the SOFC even after the carbon has been oxidized away. In summary, coupling in situ optical spectroscopy with quantitative electrochemical measurements holds tremendous promise for quantifying graphite deposits on stable, nondegraded high temperature energy conversion devices while also identifying mechanisms responsible for electrochemical oxidation and degradation in these systems. Ultimately, we expect that these techniques will be able to identify operational protocols and diagnostics that lead to long-term MEA stability and performance.

Trial	OCV (V)	Peak Power (mW)	$R_B\,(\Omega)$	$R_1\,(\Omega)$	$R_2\,(\Omega)$	$R_3\,(\Omega)$
Initial	1.2279	14.4	13.63	5.472	7.312	16.88
1.	1.2307	13.7	13.81	6.885	9.998	16.88
2.	1.2319	12.8	14.77	8.520	11.97	17.45
3.	1.2338	12.9	14.78	8.669	16.04	17.17
4.	1.2313	12.1	15.64	9.532	19.06	17.06
5.	1.2335	10.8	17.40	11.68	25.46	19.87
6.	1.2362	8.67	22.08	13.71	36.40	29.43
7.	1.2325	6.23	32.00	19.40	49.85	42.83

Table 3.2. Electrochemical parameters following each trial. OCV was measured under H_2 immediately prior to each trial; peak power is calculated from LSV data; R_B refers to pure ohmic resistance due to oxide transport; R_1 ,R_2 ,and R_3 refer to the high-, middle-, and low frequency arcs respectively.

CHAPTER 4

INSIGHTS INTO SOFC NI/YSZ ANODE DEGRADATION USING *IN SITU* SPECTROCHRONOPOTENTIOMETRY

Contribution of Authors and Co-Authors

Manuscript in Chapter 4

Author: John D. Kirtley

Contributions: Led and conducted experiments in this work, analyzed data, wrote first draft, and contributed to subsequent editions.

Co-Author: Melissa M. McIntyre

Contributions: Assisted in experiments in this work.

Co-Author: David M. Halat

Contributions: Assisted in programming data processing software.

Co-Author: Dr. Robert A. Walker

Contributions: Conceptualized experimental design, contributed to subsequent manuscript editions.

Manuscript Information Page

John D. Kirtley, Melissa M. McIntyre, David M. Halat, Robert A. Walker
ECS Transactions
Status of Manuscript:
____ Prepared for submission to a peer-reviewed journal
____ Officially submitted to a peer-review journal
____ Accepted by a peer-reviewed journal
__x__ Published in a peer-reviewed journal

Published by © The Electrochemical Society
50 (44), 2013

Introduction

While solid oxide fuel cells (SOFCs) promise high efficiencies, simplicity of design, and wide fuel versatility, many component-level challenges present difficulties in meeting minimum performance standards required for commercial viability.[10, 11, 13, 14, 111] Recently for example, significant interest has focused on anodes that minimize coking (or carbon formation) from hydrocarbon fuels. Prominent examples include development of Cu/Ceria/yttrium-stablized zirconium (YSZ)-based anodes,[112, 113] precious metal doping into the Ni/YSZ matrix,[114] BaO -modified Ni/YSZ anodes,[14, 115] and conductive metal oxides.[27, 29, 116] While many of these examples have successfully demonstrated increased carbon tolerance, difficulties with non-Ni based anodes still remain, including lower component melting points and decreased thermal compatibility with the YSZ phase.[13, 14] As such, a Ni-YSZ cermet composite remains the most common, commercially viable anode material because of its excellent catalytic ability, electronic conductivity, and thermal compatibility with the YSZ electrolyte phase.[14]

However, nickel's excellent capabilities in catalyzing C-H and C-C cleavage of various hydrocarbons fuels can also lead to severe coking (or carbon formation) on and within the bulk Ni/YSZ anode microstructure. Carbon is known to nucleate on catalytic Ni surfaces and eventually crystallize and grow into various structures, including ordered and disordered graphite, and carbon nanotubes. Minimal coking may only lead to temporary power loss, but as crystal growth continues, irreversible disintegration of the anode microstructure is inevitable through a process called metal dusting.[48, 49, 55, 91, 93]

Recently, several *in situ* spectroscopic methods have successfully demonstrated diagnostic methods and operating conditions that promote minimal coking and sustainable Ni/YSZ-SOFC operation with hydrocarbon fuels; these techniques stand poised to provide mechanistic insights into oxidative processes occurring in SOFC electrodes.[63, 117] Work by Kirtley et al. had the two-fold purpose of 1) quantifying graphite deposits on pristine Ni/YSZ anodes in functioning SOFCs using a combination of spectroscopy and chronopotemtiometry and 2) demonstrating that repeated electrochemical removal of carbon leads to cell deactivation. This technique, coined "spectro-chronopotentiometry," also provided critical insight into mechanisms that are responsible for carbon removal and Ni anode oxidation under a variety of operational currents.[118]

Spectro-chronopotentiometry (SCP) is an analytical technique that correlates *in situ* Raman vibrational spectroscopy with chronopotetiometric data. In our previous SCP experiments, a constant current was drawn through an MEA (membrane electrode assembly) that had been coked and left under a flowing, inert gas feed. In this way, graphite deposits were electrochemically removed and the rate of disappearance was monitored with *in situ* Raman spectroscopy. Continued polarization led to oxidation of the Ni anode, again observed spectroscopically. These changes in anode chemical composition were correlated with concurrent changes in the cell potential required to maintain constant current.

In the work described below, we use SCP to also develop a mechanistic understanding of 1) how Ni anodes are oxidized electrochemically in polarized cells in

the absence of a fuel and 2) how differences between Ni oxidation and carbon formation affect the long-term durability of SOFCs. By correlating increases in MEA potential with spectral features that are monitored *in situ*, insight into the species and mechanisms responsible for the potential changes can be observed. Additional clues for these mechanisms also come from monitoring changes in MEA impedance as anode microstructure degrades. From these studies, we propose that oxidation in the Ni/YSZ anode occurs via two distinct mechanisms: 1) electrochemical oxidation at lower operating loads in a pristine, functional cell and 2) oxide recombination at Ni/YSZ interfaces and subsequent oxidation of Ni by the reformed molecular oxygen at higher operating loads in degraded cells. These findings have direct relevance to polarized SOFCs forced to operate under lean or absent fuel conditions.

Experimental

SOFC Construction and Experimental Assembly

Our electrolyte-supported solid oxide fuel cells are assembled using procedures similar to those described previously.[52, 60, 61, 93] The membrane electrode assembly (MEA) consists of a 0.8 mm thick, 2.54 cm diameter YSZ (8 mole% yttria stabilized zirconia) electrolyte with a 30 μm thick 50 wt% Ni - YSZ cermet anode on one side and a 30 μm thick LSM (lanthanum strontium manganite) - YSZ cermet cathode on the other side. In the experiments described below, a gold current collecting wire (Alfa Aesar) was applied to the anode using gold paste (Heraeus); a gold wire was attached to the cathode using platinum mesh (Alfa Aesar) and platinum paste (Heraeus). The fully constructed SOFC MEA was attached to an alumina tube (2.5 cm diam.) using alumina paste and the

entire apparatus was placed inside of a quartz tube. The sample/alumina tube assembly was placed inside of a tube furnace and slowly heated to ~727±5 °C with the anode under reducing conditions. A custom optical assembly was used to direct an incident 488 nm excitation source onto the MEA as described in previous reports.[52, 60]

Spectroscopic Measurements

Vibrational Raman spectra were acquired by collecting the backscattered light from the incident 488 nm Ar-ion excitation source (24 mW focused on the anode surface by a 10x long-working distance objective). The collected Stokes radiation passed through an edge filter (to remove the 488 nm Rayleigh scattered light) and was dispersed onto a CCD detector of a Renishaw InVia Spectrometer.[52, 61, 93] When measuring kinetic data, spectra were acquired continuously with 10 second exposures per spectrum. Representative data showing Raman signals from NiO (~1050 cm^{-1}) (a) and ordered and disordered graphite (~1560 cm^{-1} and ~1350 cm^{-1}, respectively) and YSZ (~620 cm^{-1}) (b) appear in Figure 4.1.[52, 69, 93, 101]

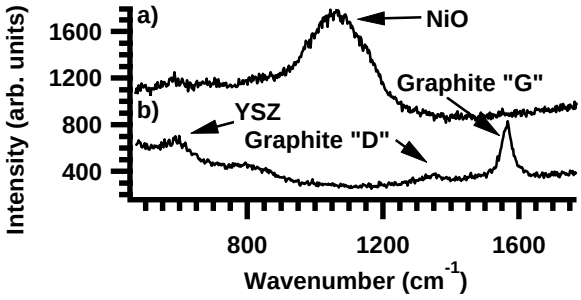

Figure 4.1. Raman spectra acquired from SOFC Ni/YSZ anode at 727±5 °C under different conditions. a) under oxidizing conditions, NiO is evidenced by the band at 1050 cm^{-1}; b) the graphitic "G" vibrational mode (~1560 cm^{-1}) and "D" vibrational mode (~1350 cm^{-1}) correspond to ordered and disordered graphite, respectively. A weak feature from the YSZ in the anode cermet is observed near 590 cm^{-1}.

Electrochemical Diagnostic Measurements

Linear sweep voltammetry (LSV), electrochemical impedance spectroscopy (EIS), and chronopotentiometry (CP) data were acquired with a Princeton Applied Research VersaStat MC before and after each experiment. Representative voltammetry data from a cell operating with H_2 appear in Figure 4.2a. We note that voltammetry measurements were not carried out to maximum current (I_{max}) conditions in order to avoid polarizing the cell excessively and causing damage during these benchmark measurements. I_{max} was estimated by extrapolating the linear region of the voltammetry data to 0.0 V. Over the course of an experiment, I_{max} diminished due to cell degradation. Power production was determined by plotting the product of each *V*-*I* ordered pair as a function of operating current. Voltammetry measurements served as benchmarks and were used to assess the device condition after each experiment that first deposited and then oxidized away carbon on the Ni cermet anode.

Electrochemical impedance spectroscopy (EIS) measurements were also performed after each trial to quantify how component resistivities changed with repeated cycling of the device.[45] An AC current of ±10 mV was applied from the cathode to the anode at rates of 100,000-0.1 Hz. The spectra were plotted in a Nyquist plot and modeled using ZSimpWin 3.22 software to quantify and associate different real and imaginary impedance elements of the SOFC using a conventional R(CR)(CR)(CR) model circuit.[45, 65] Specific electrochemical parameters (R_B, R_1, R_2, and R_3) measured after each trial can be found in Table 4.3, and a representative Nyquist plot from a cell operating with H_2 at OCV appears in Figure 4.2b. R_B is purely resistive and is associated with oxide transport

through electrolyte. R_1 and R_2 are associated with fuel activation and charge transfer at the active sites at the cathode and anode, respectively. R_3 is associated with mass transfer at the electrodes.[45, 65, 93, 101] Fuel flows during all electrochemical benchmark tests were 18 mL/min H_2/ 106 mL/min Ar to the anode; 129 mL/min air to the cathode.

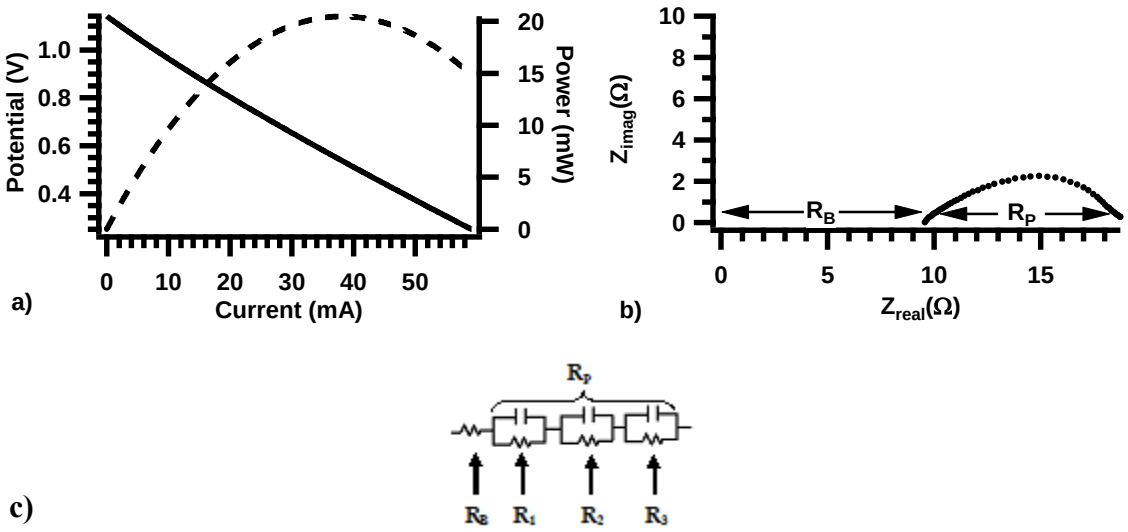

Figure 4.2. Linear Sweep Voltammetry plot where potential (V) is plotted versus current (mA), solid line and power (mW) is plotted versus current (a). In (b), a Nyquist plot depicts both capacitive (Z_{imag}) and ohmic (Z_{real}) impedances (in Ω). Pure ohmic resistance (R_B) and polarization resistance (R_P) can be modeled using an R(CR)(CR)(CR) circuit, where R_P is comprised of three smaller components (c).

Spectrochronopotentiometry (SCP)

Spectro-chrono-potentiometry (SCP) describes experiments that compare the intensities of different vibrational features in Raman spectra with electrochemical performance while a load is applied to the cell. Correlations between the relative amount of NiO and graphite present (measured in the Raman data) and the cell potential provide direct evidence of the chemical species responsible for cell potential under a chosen

current load at a given time. Such measurements can be used to quantify, for example, the amount of graphite electrochemically oxidized during the procedure.[118]

SCP experiments performed for these studies began by first monitoring the cell's OCV under 18 mL/min H_2, 106 mL/min Ar (0-10 s). A constant current of 50 mA (~70% I_{max}) was then applied to the cell under the same fuel flows, followed by elimination of H_2 in the anode gas feed at 210 s. Beyond this point, the length of each experiment was varied to show how electrochemical benchmarks depended on the extent of repetitive anode oxidation. All trials began under H_2 fuel *except* for Trials 5 and 8. For Trials 5 and 8, the anode was first exposed to 20 mL/min CH_4 at OCV for 10 min (Figure 4.5), followed by a 4.25 min. Ar purge. Carbon deposits formed during Trial 5 (and 8) were oxidized at a constant current of 50 *mA* (and 15 *mA*). Notably, also, lower current loads were used in the last three trials reflecting a decreasing I_{max}. Table 4.1 below lists these conditions for each of the 8 trials reported in this work.

Trial	Fuel	Current (mA)	Termination Point
1	H_2	50	1st equivalence point
2	H_2	50	2nd equivalence point
3	H_2	50	½ first equivalence point
4	H_2	50	2nd equivalence point
5	C_s	50	Absence of graphite
6	H_2	20	2nd equivalence point
7	H_2	30	2nd equivalence point
8	C_s	15	2nd equivalence point

Table 4.1. Experimental parameters for each of trials 1-9.

The general electrochemical observations from an SCP sequence initiated with hydrogen fuel are shown in Figure 4.3. Under conditions of constant current, cell voltage must change to accommodate changing fuel conditions. In many trials, cell voltage

passed through two sharp rises, also called electrochemical equivalence points. Raman spectra that were concurrently acquired in 10 s intervals showed how the appearance of NiO correlated with rises in cell potential. In trials 5 and 8, the loss of graphite could also be seen as cell potential rose (Figure 4.4).

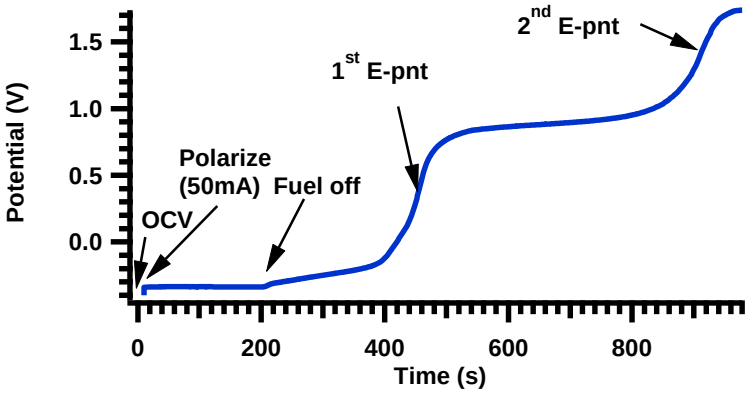

Figure 4.3. Representative chronopotentiometry trace (trial 2): 0 - 10 sec: 0 *mA* current load under 18 mL/min H_2, 106 mL/min Ar at anode; 10 - 210 sec: 50 *mA* current load under same anode flows; 210 - 978 s: 50 *mA* current load under 106 mL/min Ar.

Results and Discussion

Correlating Spectroscopic and Chronopotentiometry Data

Experiments described in this work were motivated by 1) the need to correlate directly the chemical condition of the anode with overall device performance, 2) develop insight into mechanism(s) that lead to anode oxidation and cell failure, and 3) identify whether or not observed degradation of different MEA components is reversible or irreversible. Real time correlation of chronopotentiometric and Raman spectroscopic data illustrate directly how the changing chemical condition of the SOFC anode is responsible for overall device performance. Pairing the spectroscopic/cell potential data with results

from EIS experiments (described below) illustrate how operating conditions initiate degradation in anode microstructure as evidenced by changes in MEA impedance. Figure 4.4 presents data that are representative of observations from almost all of the SCP trials. As the H_2 was eliminated from the anode chamber, the polarization data show first a slow rise in cell potential followed by a steep rise. The slow rise is assigned to a changing fuel partial pressure above the anode as the last of the H_2 diffused out of the system. The first steep rise in potential was associated with a change in mechanisms of how the SOFC generates electricity. With no fuel present and a demand for constant current, the SOFC could only begin to oxidize Ni to form NiO and two electron equivalents. The second equivalence point implies a new mechanism responsible for electrical power generation. The electrochemical data are correlated with observations in the Raman spectra. After the H_2 fuel disappeared a vibrational band assigned to NiO soon began to grow in intensity in the Raman spectra. Generally, NiO signal grew rapidly, briefly flattened and then rose steeply again coinciding with the 2^{nd} electrochemical equivalence point. One point worth noting is that the rise in Raman intensity always lagged the first electrochemical equivalence point. We denote this rapid change in Raman intensity as the first *spectroscopic* equivalence point.

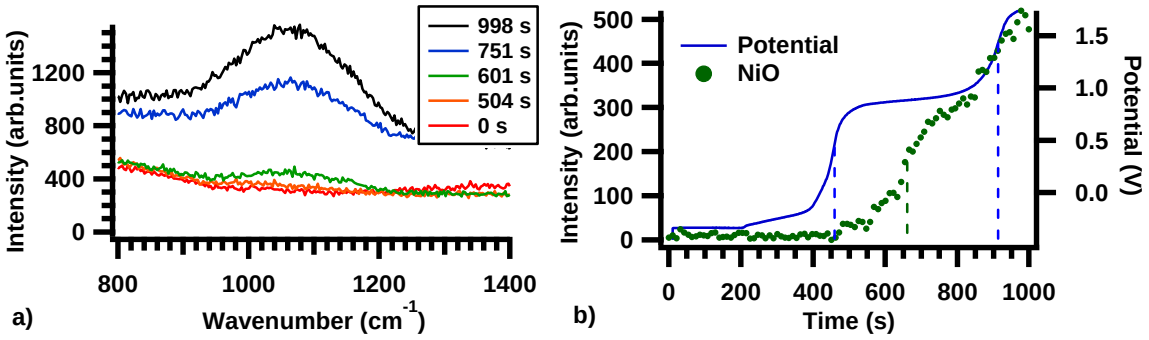

Figure 4.4. Appearance of a NiO Raman vibrational feature at 1050 cm^{-1} during SCP Trial 2. Initially, no NiO could be seen but as cell polarization continued in the absence of fuel, NiO increased (a). The intensity of this peak (vertically offset to bring lowest intensity value to 0) is correlated with cell potential as observed in real time in (b).

Comparisons between electrochemical and spectroscopic equivalence points can be made as repeated SCP cycles are performed. These values are summarized in Table 4.2. Interestingly, in Trials 1 and 3, NiO signal was never observed. This remains consistent with the hypothesis that Ni oxidation does not occur significantly until after the first equivalence point, and reflects a difference in sampling regions of the two techniques. Trials 2 and 4 were carried through the second equivalence point; trial 4 is shown above in Figure 4.4. In both Trials 2 and 4 NiO began to grow after the first electrochemical equivalence point. Trials 6 and 7 were also carried out to the second equivalence point, although the potential did not stabilize at the termination point. However, in Trials 2, 4, and 6, when NiO *was* observed, the Raman equivalence point lagged the electrochemical equivalence point *and* the delay between these two occurrences correlated inversely with the condition of the cell. A longer delay (in Trial 4) was associated with a degraded MEA. As will be discussed below, this delay is assigned tentatively to changes in the amount of Ni available to be electrochemically oxidized.

Trial	1st E-Chem (s)	1st Raman (s)	2nd E-Chem (s)	2nd Raman (s)
1	431	NA	NA	NA
2	446	646	904	892
3	~406	NA	NA	NA
4	411	733	885	NA
5	1	NA	NA	NA
6	508	915	~1184	1181
7	389	NA	~840	NA
8	0	NA	849	NA

Table 4.2. Electrochemical and spectroscopic equivalence points for trials 1-8. First spectroscopic equivalence points were determined by fitting to a sigmoidal function and recording the time when the second derivative of the function passed through an inflection point. Second spectroscopic equivalence points were best fit linearly and were consequently estimated. Note that in Trials 1, 3, and 5, SCP experiment were halted before the observed onset of NiO formation. Trials 5 & 8 were performed with anodes that had been pre-loaded with graphite formed from methane decomposition at OCV. See the Experimental Section for more details.

In Trials 5 and 8 the Ni-YSZ anodes were loaded with graphite from methane decomposition at OCV, to provide a graphite ($C_{(s)}$) fuel source. Highly ordered graphite accumulation was apparent from an increase in the Raman graphite "G" peak (~1560 cm^{-1}) (Figure 4.5).The appearance of the Raman "D" peak (~1350 cm^{-1}) was observed at later times during exposure to methane. The D-peak is a signature of disordered carbon bonding, caused by sp^3-type bonding, associated with grain boundaries and site defects within an ordered graphite network (represented by the G-peak and signature of sp^2-type bonding). The relative intensities of these two signatures can provide insight into the nature of the carbon deposits, domain sizes, and the interaction of the carbon with the anode cermet. Furthermore, the D-peak signature is generally less stable and may indicate spontaneous restructuring of carbon into more ordered structures even after deposition.[52, 70, 93, 107]

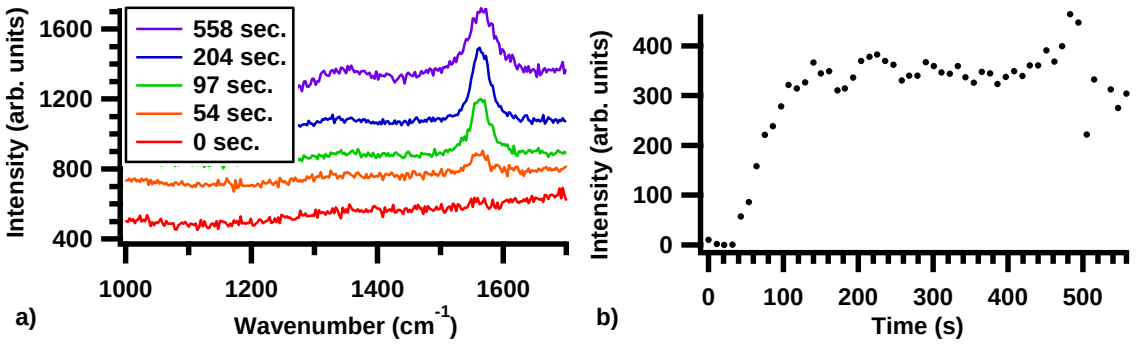

Figure 4.5. Growth of the graphite "G" and "D" Raman signatures as methane fuel is flowed over the surface of the 727 ˚C anode at OCV before SCP trial 5 (a). Raman "G" intensities (vertically offset to bring lowest intensity value to 0) are plotted as a function of exposure time (b).

Subsequent polarization of the cell during SCP Trial 5 led to the elimination of both graphite signatures (Figure 4.6). Note that as soon as the cell was polarized, the cell potential rose immediately and steeply to a value between +700 mV to + 1 V. This potential is similar to the potential reached by the MEA during trials 1- 4 (with H_2) after the first electrochemical equivalence point. Furthermore, the loss in graphite signal was nearly linear back down to baseline rather than showing expected sigmoidal pattern seen in cells operating at lower currents.[118] Together, these two observations have been associated with graphite oxidation that is dominated by non-electrochemical oxidation and may reflect either a loss of electrical and/or ionic conductivity throughout the cermet anode or a kinetic limitation of electrochemical oxidative processes.[118]

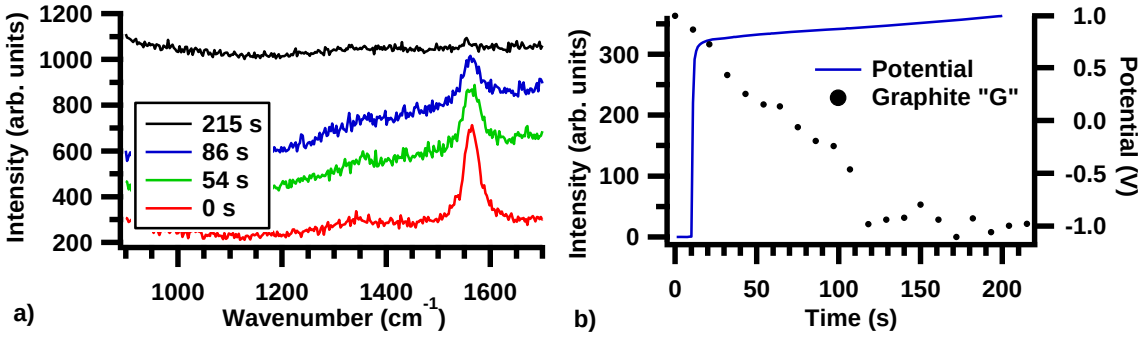

Figure 4.6. During trial 5, Raman graphite "G" signal at ~1560 cm^{-1} and "D" signal at ~1340 cm^{-1} decreased during the SCP trial (a). In (b), it can be seen that the loss in graphite signal (vertically offset to bring lowest intensity point to 0) is nearly linear as the cell is continuously loaded with 50 *mA*.

Electrochemical Insights into MEA Degradation

To assess the extent and nature of cell degradation following each SCP experiment, the MEAs were reconstituted under a reducing atmosphere and LSV scans were performed after the cell OCV had stabilized. Data from each of these benchmark experiments following an SCP trial are shown in Figure 4.7a. Further insight into the component and mechanistic-specific origins of consistent MEA power losses came from EIS measurements performed immediately after the LSV experiments (Figure 4.7b and c). The EIS data were modeled to show how different components of impedance (R_B, R_1, R_2, and R_3) changed following each trial. These results are summarized in Table 4.3.

Impedance data reported in Table 4.3 reveal several very suggestive trends that hint at the origins of SOFC anode degradation. First, R_B remained relatively constant throughout trials 1-4. This result implies that ionic connectivity through the cathode cermet, electrolyte, and anode cermet was largely continuous and experienced little degradation. After trial 5, however, R_B increased almost 2-fold. Trial 5 was the first trial

that used methane to deposit graphite on the MEA anode before conducting an SCP trial. This increase in R_B implies that carbon formation (and subsequent oxidation) severely compromised ionic conductivity. Ex-situ observation verified that significant delamination between the anode and electrolyte had occurred, and we postulate that nonelectrochemical removal of this carbon was responsible. A second large increase in R_B was observed after Trial 8, performed similarly.

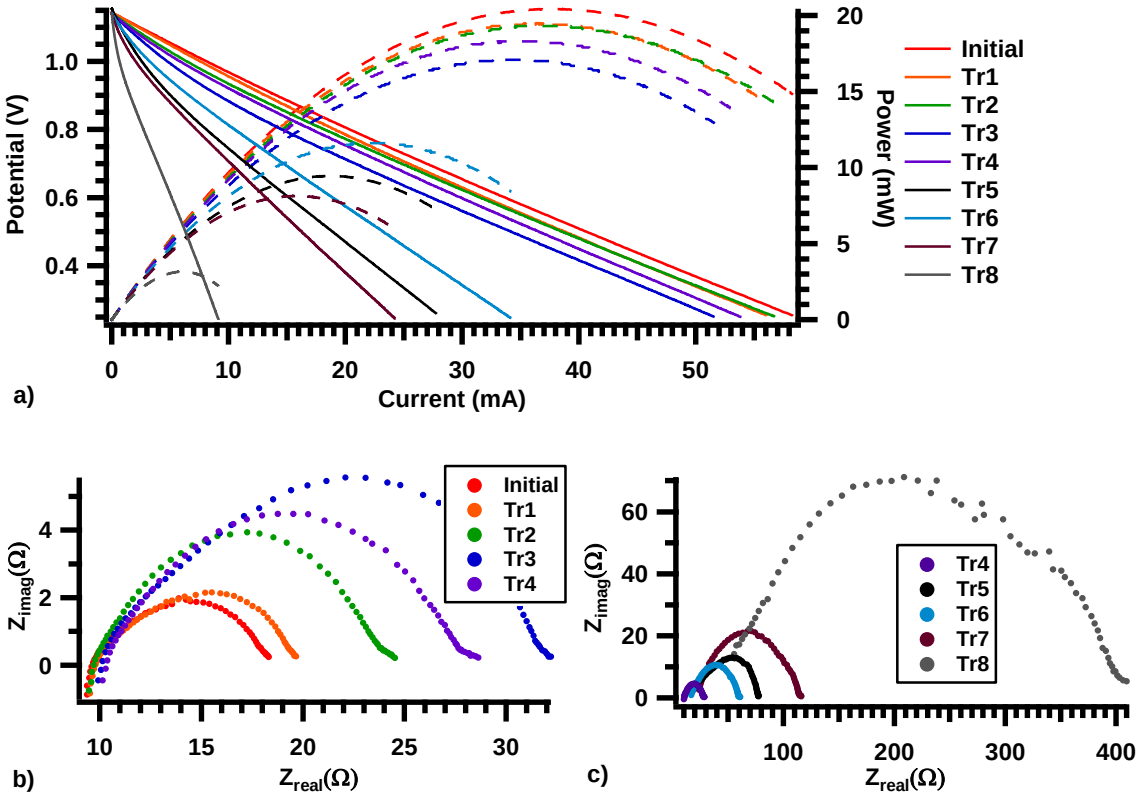

Figure 4.7. Linear sweep voltammetry (dashed lines: *P-I* traces, solid lines: *V-I* traces) (a) and electron impedance spectroscopy (b and c) performed under 18 mL/min H_2, 106 mL/min Ar (anode) and 129 mL/min (cathode) after each trial.

Trial	P_{max}(mW)	$R_{B(\text{actual},\Omega)}$	$R_{B\,(\text{rel})}$	$R_{1(\text{actual},\Omega)}$	$R_{1(\text{rel})}$	$R_{2(\text{actual},\Omega)}$	$R_{2(\text{rel})}$	$R_{3(\text{actual},\Omega)}$	$R_{3(\text{rel})}$
Initial	20.4	9.8	1.0	1.8	1.0	3.4	1.0	3.0	1.0
1	19.5	10.0	1.0	1.8	1.0	3.5	1.0	3.9	1.3
2	19.3	10.0	1.0	2.6	1.4	7.2	2.1	4.0	1.3
3	17.1	10.5	1.1	3.6	2.0	9.3	2.7	7.9	2.6
4	18.3	10.7	1.1	3.3	1.8	8.2	2.4	5.4	1.8
5*	9.5	18.8	1.9	9.9	5.5	18.7	5.5	28.0	9.3
6	11.6	17.5	1.8	7.3	4.1	18.4	5.4	15.5	5.2
7	8.1	24.7	2.5	17.7	9.8	40.8	12.0	28.9	9.6
8*	3.2	56.4	5.8	47.6	26.4	145.2	42.7	134.3	44.8

Table 4.3 Quantification of each of the four components of cell impedance following each trial. Both actual values and relative values are given above. Relative values are those scaled to initial (pre-SCP) values. Experimental uncertainty is ~±0.05 Ω
*Data following Trials 5 and 8 were acquired after SCP trials with carbon loaded anodes. See text for more details.

As noted in the Experimental section, the three resistances R_1, R_2, and R_3 used to model the EIS data are traditionally associated with cathodic, anodic and mass transfer processes, respectively. We note in passing that the EIS data showed changes in R_1 that mirrored changes in R_2 implying that the cathodic processes were inextricably coupled to the anodic processes. R_2 showed a significant and irreversible increase after Trial 2. Trial 2 was the first to oxidize the anode beyond the 2nd electrochemical equivalence point. This result may point to irreversible loss of catalytic activity and perhaps loss of anode/electrolyte connectivity at the Ni/YSZ/gas phase interfaces. Following Trial 2, the subsequent first electrochemical equivalence points appeared earlier after H_2 had been eliminated. This result may contain clues about the structural changes responsible for this first equivalence point. After the completion of Trial 5 – the first graphite SCP trial – R_2 again increased significantly, providing more evidence that carbon formation and electrochemical removal damages the electrochemically active regions within the anode. As with R_B, this damage proved irreversible. Finally, even though Trials 6 and 7 were completed to the second electrochemical equivalence point, only after trial 7 was another

large increase in R_2 observed. We speculate that oxidation of residual carbon remaining within the anode microstructure (as observed with Raman spectroscopy) before Trial 6 may have delayed the oxidation of Ni and subsequent degradation of the Ni/YSZ electrochemical activity. This was no longer a factor during Trial 7.

Finally, measured losses in R_3, associated with mass transfer resistivity, were not irreversible, contrary to the others. In general, R_3 is an indirect measure of anode porosity. Consequently, R_3 increased significantly after SCP trials with carbon laden anodes. Changes in R_3 imply that carbon may not have been removed from the anode completely following Trials 5 and 8. Generally, we observe that an additional SCP trial (with H_2) is needed to completely remove residual carbon. If cermet sintering (due to repeated redox cycling) could be decoupled from coking effects, the measurement of R_3 could become a metric for determining the total contributions of carbon to cell impedance.

Towards a Mechanistic Understanding of Cell Degradation

Correlating EIS results with the SCP data described above encourages us to infer a great deal of information about oxidative mechanisms that may take place in a cell operating under an electrochemical load as the fuel source disappears. Referencing Figure 3, we propose that from 210 s (when H_2 fuel is removed from gas feed) to 446 s (first electrochemical equivalence point), residual H_2 fuel left in the anode chamber is electrochemically oxidized. The gradual change in partial pressure of H_2 will be responsible for the gradual rise in cell potential required to maintain constant current. We

cannot discount the possibility that some Ni adjacent the dense electrolyte is also being oxidized, but these effects could not be detected by the Raman experiments.

We propose that the first electrochemical equivalence point reflects a loss in electrochemically-accessible fuel (either H_2 or carbon) and that a *new oxidative mechanism* begins to dominate, namely the electrochemical oxidation of Ni to make NiO. This consumption of anode material will occur first at the electrolyte/cermet boundary, a region that is too far away from the anode/gas phase interface to be observed in the vibrational Raman spectra. As the oxidation front moves through the Ni-YSZ cermet anode, the Raman spectra begin to show signs of NiO. It is also possible, especially as more Ni is electrochemically oxidized, that a *second* mechanism could take place in this region. Oxide ions could recombine at the anode current collector to form O_2 and 4 electron equivalents. O_2 would then be free to *chemically* oxidize non-electrochemically accessible Ni (or graphite).

Ni oxidation will diminish the extent of electrical conductivity throughout the anode. As current continues to be drawn, any remaining elemental Ni will no longer be in electrochemical contact with the rest of the anode and the *only* means for generating continued electrical current will be through O^{2-} recombination at the anode current collector. We propose that this mechanism of current generation begins to dominate at the second equivalence point observed in Trials 2 and 4. Furthermore, the molecular oxygen generated can then proceed to *chemically* oxidize Ni that is no longer electrochemically accessible. Furthermore, we note the two-step growth in NiO in Figure 4.4. This behavior is also consistent with the two electrochemical equivalence points observed. Finally, as

noted above, the delay between the first electrochemical and spectroscopic equivalence points implies that Ni oxidation begins at the anode/electrolyte interface and outside of the region that can be probed by the initial Raman experiments.

Following the second equivalence point, we expect anode oxidation to be nearly complete. As the cell potential reaches +1.7 V, we might expect that only oxide recombination is taking place, with no further oxidation of the anode cermet. This result was especially apparent during Trial 4. In later trials, the second electrochemical equivalence point never levels out (Figure 4.8). Contrary to what we observed in earlier trials, NiO signal also continued to increase. The reason for this behavior remains unclear, but it appears to be associated with a significant increase in R_B (delamination) and overall MEA degradation. Ex situ observation showed that significant delamination had occurred.

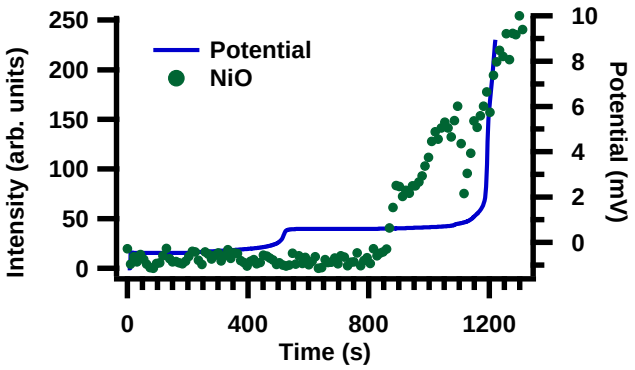

Figure 4.8. SCP Trial 6 (Raman vertically offset to bring the lowest intensity point to 0).

This delamination was initiated and enhanced by the formation and oxidation of carbon on the anode. Before Trial 6, both disordered and ordered graphitic deposits accumulated on the Ni anode. Additional experiments have shown that R_3 increases at

least seven-fold and R_2 increases at least two-fold (increases in R_B and R_1 were small) during methane exposure at OCV. (Data not shown.) This result supports the significant clogging of the porous network expected as carbon accumulates.[55, 91] While some deposited graphite will be near TPBs and available for electrochemical oxidation (note that R_2 increased ~2-fold following graphite exposure), much of the carbon will be in areas that are not electrochemically accessible. During SCP Trial 5 (Figure 4.6), one can see that the MEA had degraded sufficiently such that it no longer can sustain 50 *mA* of current in the "electrochemical oxidation region" but rose immediately to a potential near +800 *mV*. Graphite signal simultaneously dropped slowly in a linear fashion. This observation has been made previously in a degraded cell unable to maintain high current.[118] Our current hypothesis is that slow, linear depletion of graphite signal corresponds to non-electrochemical oxidation of graphite (via oxide recombination into molecular oxygen, followed by molecular oxygen reacting with carbon to form CO_2), while rapid, sigmoidal drops in graphite signal occurs via electrochemical oxidation at much lower potentials.[118]

Conclusions

While a mechanistic understanding of oxidative processes occurring in a Ni/YSZ SOFC anode *in situ* has historically proven elusive, this study provides insights into some of these processes using a unique combination of *in situ* Raman vibrational spectroscopy correlated with chronopotentiometric data (spectro-chronopotentiometry, or SCP). By monitoring in real time vibrational signatures of various species on an anode surface as fuel reserves diminish, and while simultaneously drawing a constant current through the

cell, we can begin to assign chemical and mechanistic significance to patterns observed in cell potential throughout the experiment. In this work we propose that both electrochemical and non-electrochemical oxidation of fuels and even the Ni anode can take place; the predominance of any given mechanism is a function of fuel concentration, cell impedance, and operating potential. These experiments also show how degradation in a Ni/YSZ anode under lean or absent fuels might take place, and how some oxidative mechanisms increase anode impedance, measured with electrochemical impedance spectroscopy.

Results presented here are speculative but lay a foundation for future work using spectro-chronopotentiometry and other techniques to directly correlate electrochemical performance with the underlying electrochemical mechanisms. This work also reinforces the need to further understand the close relationship between anode impedance, anode microstructure and degradation, and predominant oxidative mechanisms. Our current studies continue to explore the relationship between the chemical condition of SOFC anodes and the effect on SOFC performance and durability. A detailed understanding of oxidative processes occurring in situ will prove crucial in strategizing effective anode fabrication and cell operation.

CHAPTER 5

IN SITU RAMAN STUDIES OF CARBON REMOVAL FROM HIGH TEMPERATURE NI-YSZ CERMET ANODES BY GAS PHASE REFORMING AGENTS

Contribution of Authors and Co-Authors

Manuscript in Chapter 5

Author: John Kirtley

Contributions: Led and conducted experiments in this work, analyzed data, contributed to first draft and subsequent editions.

Co-Author: Dr. Anand Singh (University of Calgary)

Contributions: Prepared some samples used for testing, assisted in experiments, provided helpful insight, contributed to first draft and subsequent editions.

Co-Author: David Halat

Contributions: Assisted in experiments, assisted in programming data processing software.

Co-Author: Thomas Oswell (University of Calgary)

Contributions: Assisted in experiments and manuscript preparation.

Co-Author: Dr. Josephine M. Hill (University of Calgary)

Contributions: Initially approached our group for collaborative research, contributed to manuscript preparation, provided helpful insights.

Co-Author: Dr. Robert A. Walker

Contributions: Conceptualized experimental plan, provided helpful insights, contributed to manuscript preparation.

Manuscript Information Page

John Kirtley, Anand Singh, David Halat, Thomas Oswell, Josephine M. Hill, Robert A. Walker
Journal of Physical Chemistry C
Status of Manuscript:
____ Prepared for submission to a peer-reviewed journal
____ Officially submitted to a peer-review journal
____ Accepted by a peer-reviewed journal
__x_ Published in a peer-reviewed journal

Published by © American Chemical Society
117, 2013
http://pubs.acs.org/doi/abs/10.1021/jp408192e

Introduction

Solid oxide fuel cells (SOFCs) are solid state, electrochemical devices that produce electrical power by electrochemically oxidizing hydrogen and/or carbon-containing fuels into water and carbon dioxide. Consisting of three components - cathode, anode, and solid oxide electrolyte - SOFCs typically operate at temperatures in excess of 700 °C in order to achieve desired current and power densities.[10-12] These high operating temperatures also enable SOFCs to be fuel flexible. Unlike lower temperature devices that use precious metal catalysts and can only function with clean sources of H_2, SOFCs can operate with H_2, natural gas (CH_4), syn-gas (H_2/CO mixtures), renewable biogas (CH_4/CO_2 mixtures), and higher molecular weight hydrocarbons, provided that carbon accumulation can be avoided.[11, 119-121] Carbon-containing fuels can form carbon deposits (described more generally as "coke") on SOFC anodes. These deposits block catalytic sites, impede mass transport, and induce structural changes in the anode microstructure that adversely and irreversibly impact overall device performance.[48, 55, 90, 91]

Carbon formation and removal occur simultaneously on Ni/YSZ anodes during operation with carbon-containing fuels. Carbon accumulation occurs when the rate of carbon formation exceeds the rate of carbon removal.[120] Species created from fuel reforming or intentionally added to the fuel feed can remove the deposited carbon via reactions shown below (equations 5.1 and 5.2). Minimal leakages of O_2/air into the anode chamber may sometimes also occur with button cell testing because of incomplete sealing between the anode and cathode environments. O_2 in the anode chamber can remove carbon through direct oxidation[122] (reaction 5.3).

5.1 $C_{(s)} + H_2O_{(g)} \rightarrow CO_{(g)} + H_{2(g)}$

5.2 $C_{(s)} + CO_{2(g)} \rightarrow 2CO_{(g)}$

5.3 $C_{(s)} + O_{2(g)} \rightarrow CO_{2(g)}$

Significant effort has focused on improving anode carbon tolerance through modification of conventional Ni/YSZ anodes, new anode material development, and new cell design; different analysis techniques have been used to assess the ability of these newly developed anodes to resist carbon accumulation under different operating conditions. Operational stability[123-125] is important, but traditional electrochemical methods used to assess SOFC performance do not isolate the chemical or structural evolution responsible for changes observed during device performance.[93] More detailed information has been obtained by techniques including in situ thermogravimetric analysis (TGA) of Ni/YSZ powders doped with Au,[126, 127] Ag,[128] and Sn,[129] energy-dispersive ex situ X-ray spectroscopy (EDX) for Ni/YSZ powders doped with Sn,[124] and temperature programmed oxidation (TPO) for a variety of Ni/YSZ anodes operated at different conditions.[55, 92, 119-121, 130] The latter two techniques give qualitative (TPO) and/or quantitative (EDX, TPO) information about carbon accumulation but do not differentiate the carbon formation and removal rates. TGA used in situ can give information about the separate rates if the processes do not occur simultaneously.

Recent advances using in situ Raman spectroscopy and near-IR thermal imaging allow carbon formation and removal rates to be probed independently, by sequentially exposing a cell to different conditions.[93, 131] In addition to the importance of carbon accumulation/removal in SOFCs, removing carbon deposits has long been a subject of

strong interest to chemical and petroleum engineers in the context of regenerating spent catalysts where deposits have deactivated the catalysts and of gasification when solid carbonaceous fuels (e.g., coal, petroleum coke, and biomass) are converted to gaseous components (e.g., CO, H_2, and CH_4). Identifying the exact mechanism responsible for carbon gasification is difficult as numerous reactions occur simultaneously in a gasifier. Snoeck et al.[132] used a gravimetric balance to develop a model describing how carbon gasification processes are sensitive to both the type of carbon present and the gasifying agent. The authors determined that carbon gasification between 500 and 575 °C by carbon dioxide and water occurred at similar rates but via different processes. Otsuka and co-workers[133] examined structural changes and particle growth in various catalytic supports under repeated carbon formation cycles of methane on Ni, followed by gasification by carbon dioxide. These latter studies are relevant for SOFC electrodes because Ni particle agglomeration was found to lead to diminished catalytic activity.

These gasification studies provide guidance about how to evaluate the removal of carbon from an SOFC anode. In SOFCs, electrochemical performance and durability depend sensitively on electrode microstructure, and any process that alters that microstructure is likely to adversely affect device durability. Excessive carbon formation affects the microstructure and conventional wisdom advises that any carbon formed must be removed in such a way without inducing large scale structural change in the underlying anode. More specifically, in the case of Ni/YSZ anodes, the reforming agent used to remove carbon should not also promote widespread formation of nickel oxide (NiO). If NiO forms during carbon removal, the anode volume will increase (due to

lattice expansion) and add mechanical stress to the anode.[45, 47] The three phase boundary (TPB) length will also shrink limiting the amount of charge transfer.[45]

Work presented below utilizes in situ vibrational Raman spectroscopy to study the rate of carbon formation on Ni/YSZ anodes held at open circuit voltage (OCV) and exposed to dry CH_4 for 10 min. Time-resolved spectra (10 s resolution) monitor this growth of carbon. Carbon removal under subsequent exposure to common gas-phase reforming agents (or oxidants) ($H_2O_{(g)}$, CO_2, or O_2) was also monitored with Raman spectra. All experiments were performed near 730 °C. Data show that H_2O is the most effective agent and removes carbon deposits within ~10−20 s. Removal by CO_2 is much longer, ~120 s, and removes carbon deposits quantitatively, presumably through reverse Boudouard chemistry. Surprisingly, the rate of carbon removal by O_2 is intermediate between these two limits. O_2, however, is the most aggressive agent in terms of subsequently oxidizing the anode Ni to form NiO. H_2O and CO_2 only partially oxidize the Ni. Spectroscopic data correlate closely with changes in open circuit voltage (OCV) illustrating a direct coupling between the chemical condition of the SOFC anode observed spectroscopically and the electrochemical condition of the device. Results from this comparative study should prove useful for scientists and engineers working to improve the carbon tolerance and reconstitution of SOFC anodes through modifications to incident fuel composition, anode materials, and/or operating conditions.

Experimental Section

SOFC Construction and Device Assembly

Two types of electrolyte-supported membrane electrode assemblies (MEA) were constructed using slightly different procedures to test the generality of our findings. As will be discussed below, data show consistent behavior in terms of the relative carbon removal rates by different gas phase reforming agents.

For type A cells, the anode powder was prepared by mixing NiO (50.6 wt %, Alfa Aesar) with YSZ (43.1 wt %, TZ-8Y; Tosoh Co, Japan) and graphite (6.3 wt %, Alfa Aesar) by ball milling in acetone for 24 h. The powders were dried and sieved to particle sizes less than 150 μm. The anode powder was then mixed with glycerol to make a slurry suitable for brush painting. The electrolyte was fabricated by uniaxially die pressing YSZ powder to a pressure of 53 MPa and then sintering at 1450 °C for 2 h. The anode slurry was brush painted on the electrolyte and sintered in air at 1450 °C for 2 h. The cathode powder was prepared by mixing $La_{0.8}Sr_{0.2}MnO_3$ (40 wt %, LSM, Praxair Specialty Ceramics) with YSZ (40 wt %) and graphite (20 wt %). The cathode powder was mixed with glycerol and applied on the other side of the electrolyte and sintered at 1250 °C for 2 h. The thickness of the anode (Ni/YSZ), cathode (LSM/ YSZ), and electrolyte (YSZ) for type A MEAs were 175, 80, and 600 μm, respectively. The areas of the anode and cathode were 0.9 cm^2.

The electrolytes used to manufacture type B cells were prepared similarly to cell A, except electrolytes were pressed at 115 MPa and sintered at 1450 °C for 3 h. Anode paste (Fuel Cell Materials, 66%/34% NiO/YSZ by mass) was painted onto the sintered

electrolyte and sintered (in air) at 1300 °C for 3 h. Cathode paste (Fuel Cell Materials, 50%/50% LSM/YSZ by mass) was painted onto the opposite side of the electrolyte and sintered at 1150 °C for 1 h. The thicknesses of the anode, cathode, and electrolyte were ~30, 30, and 800 μm, respectively. The areas of both the anode and cathode were ~1.0 cm^2.

The cathode side of each type of cell was attached to an alumina tube using ceramic paste (552 VFG, Aremco) to provide a gastight seal from the anode. A custom quartz tube (Quark Glass) was fitted over the alumina tube/MEA assembly and sealed with a silicon stopper at the base. The device was fitted inside a tube furnace and heated to ~730 °C at a rate ≤1 °C/min with low flow rates of H_2/Ar (anode) and air (cathode). Further details of the high temperature SOFC rig may be found in previous publications.[52, 61]

Raman Vibrational Spectroscopic Measurements

Vibrational Raman spectra were acquired in situ by directing a ~24 mW, 488 nm Ar ion excitation source through a quartz tube onto the anode surface (using a 10× long-working distance objective) and collecting the backscattered light. The objective was attached to a custom-designed optical assembly and cooled with compressed air. The 488 nm Rayleigh scattered light was removed by an edge filter (150 cm^{-1} cutoff) while the backscattered Stokes radiation was dispersed onto a CCD detector of a Renishaw InVia spectrometer.[52, 93] When measuring kinetic data, spectra were acquired continuously with 10 s exposures per spectrum.

Electrochemical Diagnostic Measurements

Linear sweep voltammetry (LSV) and electrochemical impedance spectroscopy (EIS) data were acquired with a Princeton Applied Research VersaStat MC. Voltammetry measurements were carried out by measuring cell potential as current load increased from 0 *mA* (or OCV, Figure 5.1a). The current "sweep" was not carried out to maximum current (I_{max}) in order to avoid excessive electrochemical loading of the cell and device damage. EIS measurements (Figure 5.1b) measured the MEA's impedance with ac amplitude of 10 *mV* in the frequency range of 100 000−0.1 Hz at OCV. Voltammetry and EIS measurements served as benchmarks to identify correlations between material changes and the higher resistances that signify cell degradation. Both were used to assess the condition of cell A after each experiment and initially for cell B that first deposited carbon on the Ni/YSZ cermet anode, followed by removal via gas phase oxidants. Fuel flows during all electrochemical benchmark tests for cell A were 18 ± 1 mL/min H_2 and 106 ± 2 mL/min Ar to the anode and 13 ± 1 mL/min air to the cathode. Fuel flows during initial electrochemical benchmark tests for cell B were 31 ± 1 mL/min H_2 and 200 ± 2 mL/min Ar to the anode and 143 ± 2 mL/min air to the cathode.

Graphite Formation and Removal
via Gas Phase Oxidants

Individual MEAs were subject to repeated cycling. A timeline for one cycle is illustrated in Figure 5.2. The Ni cermet anode was anode was exposed first to a flow of 20 mL/min methane (diluted with 106 mL/min Ar and 200 mL/min Ar for cells A and B, respectively) for 565 s in order for carbon deposits to form. The anode was then flushed with 106 mL/min and 200 mL/min Ar for cells A and B, respectively, for 265 s before

introducing the oxidant and monitoring the disappearance of carbon and growth of NiO. The oxidants used were H_2O, CO_2, or O_2 (Table 5.1), and exposures were usually limited to 565 s to minimize the risk of excessive anode oxidation.

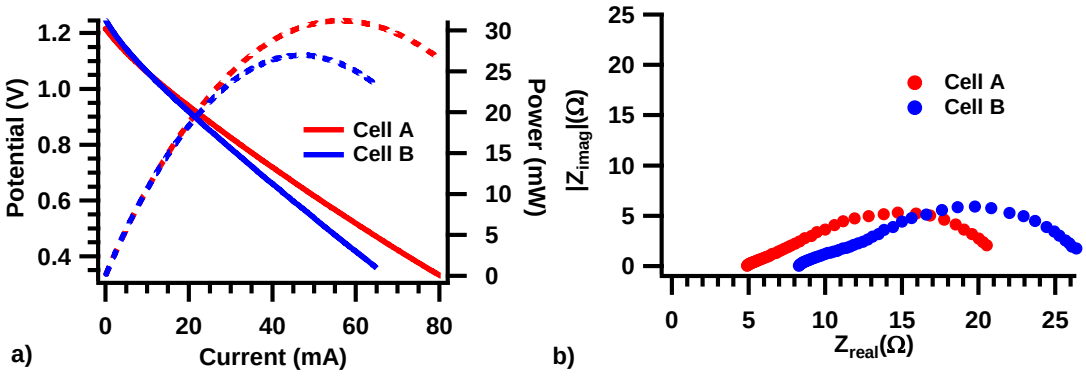

Figure 5.1. Initial electrochemical benchmark measurements made on cells A and B. In (a), the $V-I$ traces are represented as solid lines; the corresponding $P-I$ traces are represented as dashed lines. P_{max} can be seen as the peak in the $P-I$ traces. Electrochemical impedance data for each cell are shown in (b).

Every cycle was performed while the MEA was held at OCV. During the course of a cycle, OCV would vary to reflect changes in anode surface species and the gas phase composition above the anode. A MEA with a virgin Ni anode exposed to H_2 typically had an OCV of −1.21 *V*; during graphite formation under CH_4, the OCV would fall to −1.29 *V* and then would rise to −0.7 *V* or higher following the onset of observed Ni oxidation. For all experiments for which electrochemical measurements were made, the cathode was exposed to a continuous flow of air. Between the experiments performed with type A and B cells, small changes in the gas handling manifolds (intended to correct small disparities in oxidant partial pressures and residence times) led to slightly different exposure times.

The oxidant residence times at the anode varied between 0.5 and 2.0 s, much less than the spectroscopic temporal resolution of 10 s (Table 5.1).

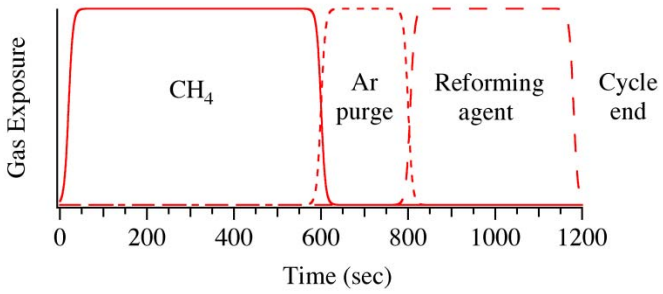

Figure 5.2. Schematic diagram showing the sequence of gas exposures during a single carbon formation/removal cycle. Both the CH_4 and reforming agent were present at low partial pressures in an Ar carrier gas. Quantitative details related to residence times and loads are reported in Table 5.1.

oxidant	number of trials	flow rate (mL/min)	oxidant in gas flow (%)	gas residence time (s)
Cell A				
H_2O	3	2 ± 0.1	2	1.1
CO_2	3	13.4 ± 0.5	11.2	1.9
O_2	2	12.0 ± 0.5	10.2	2.4
Cell B				
H_2O	1	4 ± 0.1	2	0.6
CO_2	2	13.4 ± 0.5	6.3	1.4
O_2	2	13.4 ± 0.5	6.3	1.9

Table 5.1. Flow parameters and number of trials for each particular measurement.

Results and Discussion

Spectroscopic Studies of Carbon Formation

Ex situ[121, 122] and *in situ*[52, 93, 118] measurements have shown clearly that methane forms carbon on Ni cermet anodes, especially when the SOFC is held at OCV. Furthermore, recent in operando studies[118] have identified that most of the carbon formed

initially from methane on porous Ni−YSZ anode surfaces consists of ordered graphite. Exposure to higher molecular weight fuels results in the formation of "disordered" graphite; in some cases this depended upon exposure length.[52, 98] This graphite by nature possesses a higher density of site defects and/or grain boundaries. At temperatures < 600 °C, methane can form filamentous carbon on Ni particles.[49, 134] The amount of carbon formed can be quantified in several ways. Oxidizing the carbon deposits in a temperature-programmed oxidation (TPO) experiment records the onset of carbon oxidation as a function of temperature, and quantifying the amount of CO_2 produced is accomplished with calibrated mass spectrometry. A second, independent means of quantifying the amount of carbon formed from coking couples data from electrochemical measurements with data from in situ vibrational spectroscopy.[118]

Figure 5.3 shows the growth of graphite on Ni cermet anodes at 730 °C exposed to 20 mL/min of CH_4 (in Ar). Prior to exposure, the Raman spectrum is featureless from 1200 to 1700 cm^{-1} (Figure 5.3a). In a matter of seconds following the introduction of CH4, a vibrational band appears in the Raman spectrum at 1556 cm^{-1} (Figure 5.3a,b). This signal is assigned to the "G" peak of highly ordered graphite.[69, 70, 135, 136] Over the course of ∼7−8 min, the graphite signal continues to grow before reaching an asymptotic limit. These data are consistent with previously reported work that compared the tendencies of different carbon containing fuels to form graphite on polarized and unpolarized Ni cermet anodes.[93] The limiting signal intensity is likely a measure of the penetration depth of the Raman excitation light. Furthermore, the carbon observed at the surface can differ from that further into the bulk near electrochemically active regions.[118,

[137] The amount and identity of deposited carbon will change with the identity of the fuel[61] and temperature.[37] We also cannot discount the possibility that if carbon blocks all of the active sites, then graphite accumulation may cease. However, other reports have indicated that in the limit of high carbon coverage nanotubes and fibers will begin to grow at lower temperatures (<700 °C),[55, 134] but at higher temperatures carbon diffusion into the bulk becomes significant.[55, 138, 139]

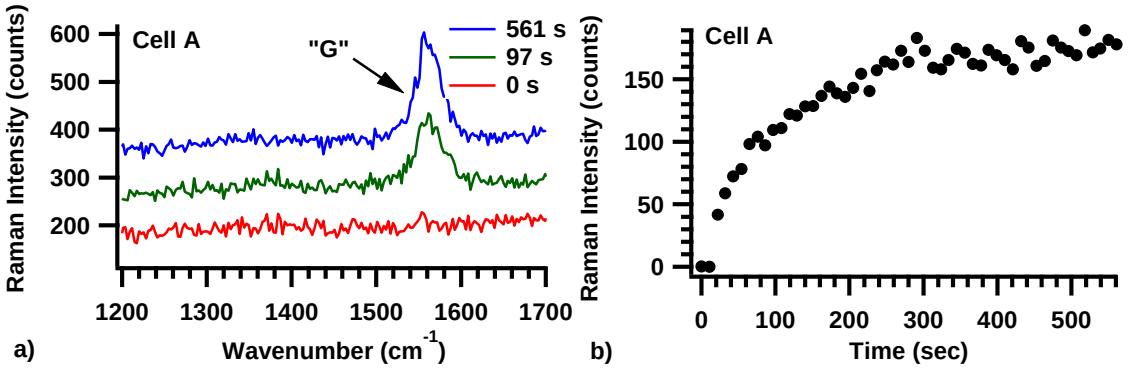

Figure 5.3. (a) Growth in the Raman "G" vibrational mode of graphite on a Ni/YSZ anode during 565 s of methane exposure at ~730 °C over cell A. Each spectrum represents 10 s accumulation. Spectra have been offset vertically for clarity. (b) Intensity of the G peak at 1556 cm^{-1} as a function of time (vertically offset).

Conspicuously missing in the spectra is any discernible intensity near 1360 cm^{-1}, indicating an absence of disordered (or "D") graphite that contains site defects, grain boundaries, or other noncrystalline structures.[69, 70, 136] Previous TPO analyses of Ni/YSZ anodes after exposure to methane suggest that amorphous carbon forms before graphitic carbon.[121] Samples analyzed with TPO, however, were subject to CH_4 exposures that were ~50 times longer than the CH_4 exposures used in the current studies. Longer exposures might enable additional carbon formation pathways to affect accumulation. A second source of differences between the TPO and spectroscopic results is sample

volume. TPO experiments collect information about carbon present throughout the entire anode structure, whereas Raman spectroscopy probes only 1−5 μm into the anode microstructure. Finally, samples measured with TPO have necessarily cooled from SOFC operational temperatures back to room temperature. If any structural changes occur during cooling, then the carbon sampled in a TPO experiment will be different from the carbon deposits probed by the in situ spectroscopic methods described above (see Figure B.1).

Spectroscopic Studies of Carbon Removal via Gas Phase H_2O, CO_2, and O_2.

Figure 5.4 shows the effects of introducing anode gas-stream reforming agents over anodes containing carbon deposits formed in the manner described above. Figure 5.4a reports representative spectra illustrating the removal of graphite by water from the anode of cell A. Water is very effective at removing the deposited carbon, and in fact, the graphite signal disappears almost as quickly as spectra can be acquired with no observable carbon remaining 30 s after H_2O has been introduced to the anode. These results are consistent for multiple MEAs tested of both types.

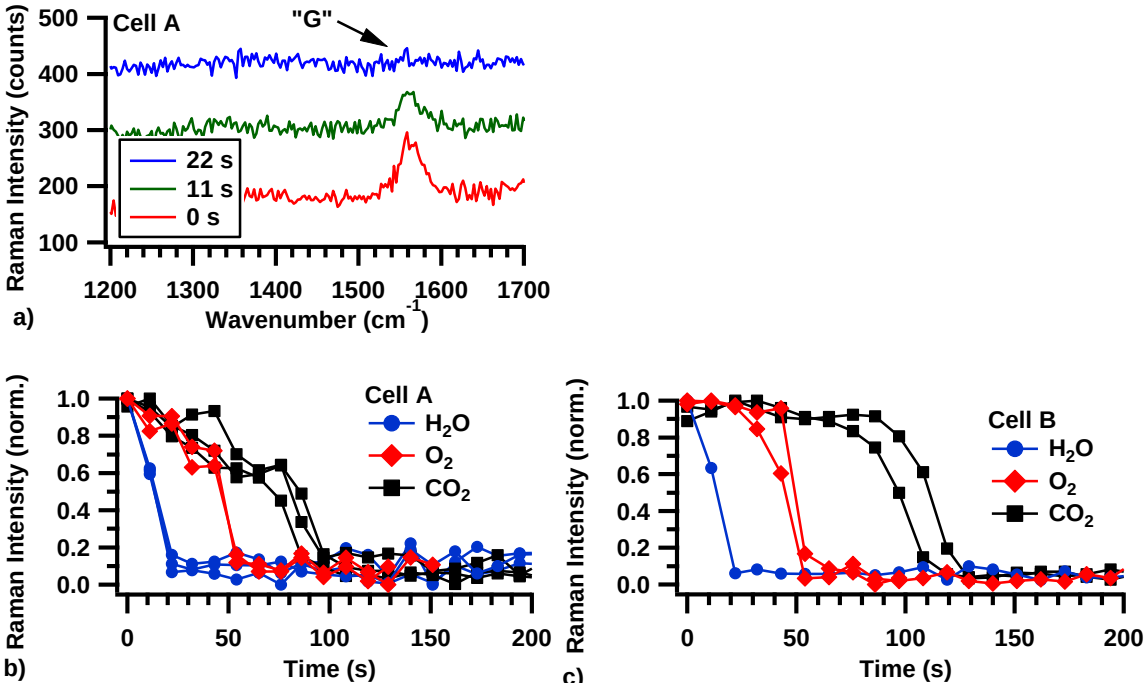

Figure 5.4. Decrease in Raman 1556 cm^{-1} "G" peak intensity as H_2O removes surface carbon in cell A (a). A comparison of the drop in vertically offset, normalized Raman 1556 cm^{-1} peak intensities can be seen in (b) in which H_2O(g) (three trials), CO_2(g) (three trials), and O_2(g) (two trials) oxidize graphite previously deposited on a Ni−YSZ MEA (cell A). Similarly, graphite is removed from cell B using H_2O(g) (one trial), CO_2(g) (two trials), and O_2(g) (two trials) in (c).

Figures 5.4b and 5.4c show the normalized spectroscopic graphite signal from cells A and B, respectively, as a function of time following the addition of H_2O, O_2, and CO_2. Several observations stand out. First, relative to the rate of graphite formation, removal of surface graphite deposits via gas phase additives occurs quickly. This result is exemplified during oxidation with water as noted above. Second, the data show clear differences in the time required for each gas phase reforming agent to remove graphite completely. Graphite disappears on a ~20−125 s time scale, depending on the gas phase reforming agent (see Table 5.2). H_2O removes graphite most quickly - within ~20 s - while removal by O_2 and CO_2 require longer exposures of ~60 and ~120 s, respectively.

Cell A			
reforming agent	$C_{(s)}$ oxidation time (s)[a] [sample size]	Ni oxidation time (s)[a] [sample size]	$\Delta t_{lapse\ time}$ (s)[b]
3% H_2O	20 [3]	205 ±40 [3]	185
10.2% O_2	55 [2]	75 [3]	23
11.2% CO_2	105 [3]	255±65 [2]	150
Cell B			
3% H_2O	20 [1]	160 [1]	140
6.3% O_2	60 [2]	60 [2]	0
6.3% CO_2	120 [2]	180 [2]	60

Table 5.2. Time required for the graphite intensity to return to base levels, and for NiO intensity to increase above base levels, with exposure to different gases at ~730 °C.
[a]Unless otherwise reported, uncertainties = ± 10 s (limited by spectra collection).
[b]$\Delta t_{lapse\ time}$ = interim period between loss of $C_{(s)}$ signal and onset of NiO signal.

Data reported in Figure 5.4 and Table 5.2 are consistent between the two types of cells, and the trends appear to be general. Assuming that adsorption of the gas phase reforming agent is not rate limiting and that all mechanisms responsible for carbon gasification require common final reactions to produce CO and/or CO_2, then observed differences in the relative rates of carbon removal will result from barriers to forming surface oxygen. Deutschmann and co-workers[57] have considered different mechanisms that examine carbon formation from methane and carbon gasification by both H_2O and CO_2. Rate constants used in these models predict that at 727 °C water will dissociatively chemisorb on Ni to form surface oxygen ≥3 times faster than CO_2. Carbon removal rates observed in the vibrational Raman data support this prediction. Molecular oxygen chemisorption and dissociation were not considered in the Deutschmann model, but King and co-workers[140] used calorimetry to study dissociative O_2 chemisorption on Ni[211] and discovered that adsorbed oxygen atoms are strongly bound initially by Ni step edges. Only after longer O_2 exposures do oxygen atoms adsorb to Ni terraces and begin to form oxides. If the first oxygen atoms formed on a polycrystalline Ni catalyst are tightly bound

to step edges, then the population of reactive oxygen species (on the terraces) will require time to grow leading to a delay between when O_2 is introduced to the sample and when carbon deposits begin to disappear. A second mechanism that can restrict carbon removal by chemisorbed oxygen atoms at early times is a lack of catalytically active Ni sites. A combined density functional theory and kinetic analysis[141] has shown that carbon preferentially forms at the step edges. If these edges are covered with carbon, the initial rate of oxygen dissociation (and carbon removal) will be reduced.

Other models have also proposed that the rate-limiting step of carbon gasification is the reaction of surface oxygen with carbon and that the rates of carbon gasification with CO_2 and H_2O should be similar at 500 °C.[132] Our results reported above do not support this prediction. If the rate-limiting step in carbon gasification is the creation of surface oxygen and not the reaction of surface oxygen with carbon, then the rate constant data calculated by Snoek et al. predict that carbon gasification should be ~10−100-fold faster with H_2O than with CO_2, a prediction more consistent with that of the Deutschmann model and supported by measurements reported in this work. Taken together, experimental observations described above coupled with existing kinetic models strongly suggest that the barrier to deposited carbon gasification in SOFCs arises from the creation of reactive surface oxygen from reforming agents adsorbed from the gas phase.

Spectroscopically Observed Ni
Oxidation via H_2O, CO_2, or O_2

Following removal of deposited graphite, continued exposure to the reforming agents led to the appearance of a new, broad feature in the Raman spectra at 1050 cm^{-1}

assigned to NiO. Figure 5.5a shows spectra acquired from the Ni cermet anode (cell A) exposed to O_2 as a function of time. Once the graphite has been removed, the NiO signal appears and grows quickly in the presence of O_2 and more slowly in the presence of H_2O and CO_2 (Figure 5.5b). Furthermore, the extent of Ni oxidation is greater with O_2 than with the other gases (see Figure B.5). The onset of NiO formation in each trial was determined by the spectrum which showed a signal at 1050 cm^{-1} above baseline levels. The data are reported in Table 5.2 for each trial. Coupled with electrochemical data presented below, these experiments show that while H_2O is more effective at removing graphite from the Ni anode, O_2 is much more aggressive in completely oxidizing the Ni cermet anode.

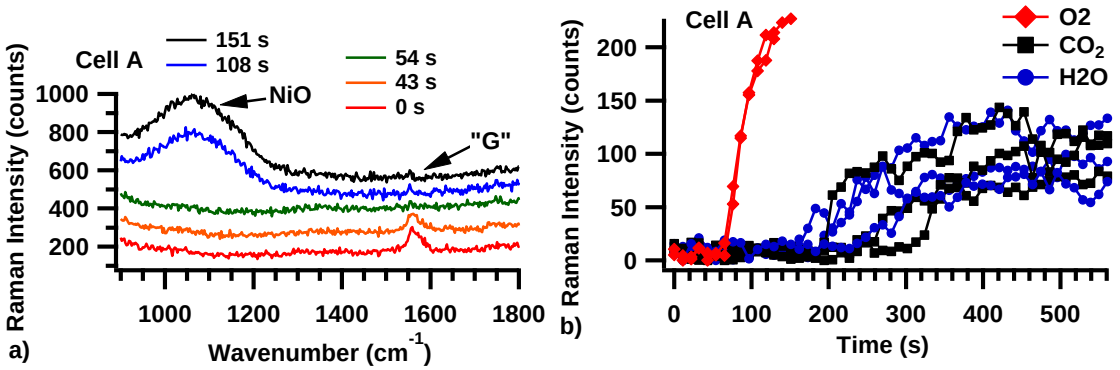

Figure 5.5. After carbon is removed from a cell A anode by O_2, NiO (1050 cm^{-1}) forms at 730 °C (a). NiO peak intensities are plotted as a function of time for anodes exposed to H_2O, CO_2, and O_2 at 730 °C (data have been vertically offset to bring lowest intensity point to zero) (b).

One additional observation can be made from the data in Figure 5.5 and Table 5.2. For each reforming agent, graphite removal always precedes Ni oxidation, but with O_2, the onset of NiO formation coincides closely with the disappearance of graphite. The mechanism proposed in the preceding section is consistent with this observation,

assuming that the initial chemisorbed oxygen sequesters to step edges and does not promote widespread Ni oxidation. Reactive oxygen that does form through dissociative chemisorption will first oxidize carbon and then Ni. With both H_2O and CO_2, a measurable delay separates the loss of carbon and the growth of NiO (Table 5.2). The appearance of NiO coincides with cell OCV approaching an asymptotic limit of −0.73 V characteristic of the NiO/Ni standard reduction potential[142] (*vide infra*). The observation that H_2O and CO_2 are both much less aggressive than O_2 as a Ni oxidant reflects the reversible nature of the chemistry responsible for Ni oxidation. The reactions responsible for Ni oxidation by the reforming agents used in this study are as follows:

5.4 $Ni + H_2O \leftrightarrow NiO + H_2$

5.5 $Ni + O_2 \leftrightarrow NiO + O$

5.6 $Ni + CO_2 \leftrightarrow NiO + CO$

The amount of NiO formed depends on the equilibrium for these reactions under the conditions of interest. Even allowing for uncertainties in the formation energies of adsorbed species, at 730 °C reactions 4 and 6 have small positive ΔG_{rxn} in the forward direction while reaction 5 has a large negative ΔG_{rxn}. These considerations predict that both H_2O and CO_2 will promote modest amounts of Ni oxidation while O_2 produces a "product" - adsorbed oxygen - that remains a strong oxidant capable of creating additional NiO. Additional studies by Kirtley et al.[108] used Raman spectroscopy to examine NiO/Ni redox chemistry at 715 °C as a function of particle size and conditioning history. While the measured kinetics showed subtle, size-dependent differences, all of the measurements demonstrated that NiO reduction by H_2 (in Ar) was very fast (on a 5−20 s

time scale). Nickel oxidation by O_2 required minutes before the Ni particle surfaces were fully oxidized. From these studies we conclude that small amounts of atomic or molecular hydrogen produced from water dissociation on a Ni surface will prevent Ni from oxidizing completely. CO can also serve as an effective reducing agent for NiO with a relatively low activation energy for CO oxidation of 56 kJ/mol and a strong dependence on the availability of surface oxides.[143] If CO_2 is assumed to have slow dissociative behavior on Ni based on the carbon removal data presented above, then we would expect a low concentration of surface oxides and correspondingly little observed Ni oxidation.

Open Circuit Voltage Measurements during Graphite Formation and Oxidation

Changes in the anode surface composition correlate closely with reproducible, systematic changes in the measured open circuit voltage of the device. Figure 5.6 shows representative OCV traces acquired as a function of time during experiments performed with H_2O, O_2, and CO_2. Figure 5.7 shows the individual OCV traces together with Raman intensities of the graphite and NiO features observed in a given cycle. The OCV traces for all three gases have several features in common, and these features correlate directly with changes observed in the spectroscopic data acquired for each system.

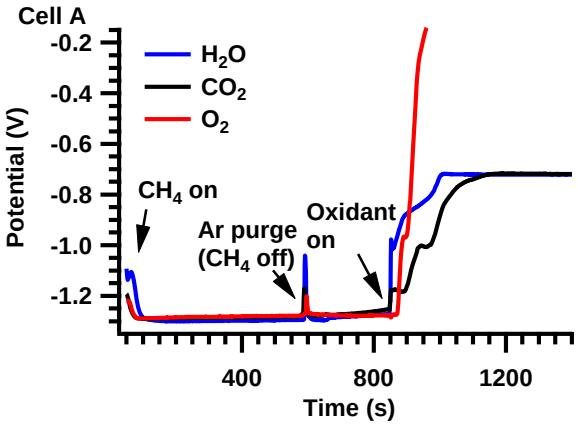

Figure 5.6. Comparison of changes in cell A OCV as graphite is first deposited via methane fuel, followed by purging, and subsequent removal via H_2O, CO_2, or O_2. Traces have been horizontally offset to coincide with introduction of oxidant gas.

First, the formation of graphite from gas phase CH_4 leads to an OCV of -1.29 ± 0.02 *V*, approximately 0.1 *V* larger in magnitude than OCV with hydrogen. Insofar as OCV represents a difference in free energies between reactants and products, a larger OCV shows that loading the anode with carbon improves the ability of the cell to generate electrical power. This conclusion is also supported by an improved P_{max} and OCV observed under methane fuel in other recent studies.[144, 145] Furthermore, these observed changes in OCV under CH_4 and subsequent solid carbon formation imply that carbon should be oxidized preferentially to Ni under oxidizing conditions. Only when carbon has been removed should any reforming agent begin to oxidize the Ni anode.

Second, the OCV rises steeply for all cells exposed to all reforming agents, but this increase is greatest and most abrupt for O_2. The magnitudes of these OCV increases are consistent from run to run and from cell to cell. The observed net change in OCV of cells exposed to O_2 is +1.15 *V*, and the voltage does not quite converge to an asymptotic

limit before the cycle is halted to prevent irreversible oxidative damage to the anode microstructure.

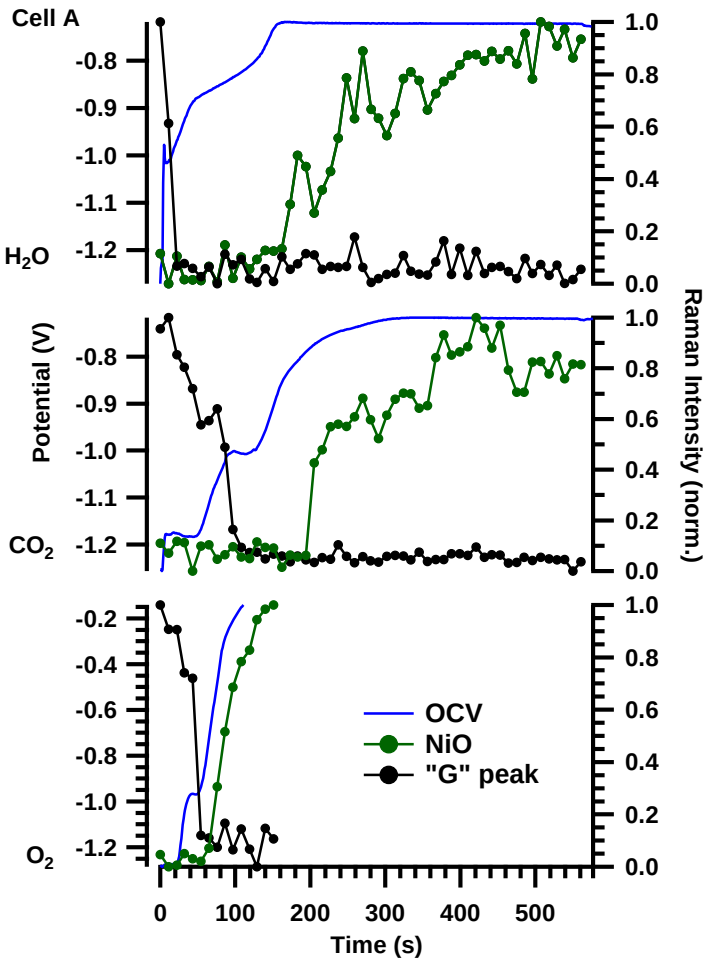

Figure 5.7. Correlation of OCV with spectroscopically observed graphite "G" and NiO as graphite deposits are removed via H_2O, CO_2, and O_2 in cell A. Each Raman trace has been vertically offset to bring lowest point to zero.

For cells exposed to either H_2O or CO_2, the total change in OCV is only +0.55 *V*, and in each system, the SOFC OCV approaches −0.73 ± 0.01 *V*. This potential coincides with the redox potential assigned to Ni/NiO equilibrium at 700 °C, adjusted for the partial pressures of O_2 on the cathode and H_2O or CO_2 on the anode. These data imply that after

carbon has been removed from the anode, both of these reforming agents partially oxidize nickel to make nickel oxide and establish a Ni/NiO equilibrium, a conclusion supported by spectroscopic data as well as thermodynamic considerations. Additional evidence that both H_2O and CO_2 are capable of maintaining a Ni/NiO equilibrium can be inferred from the relatively slow approach of OCV to its asymptotic limit.

The rise in OCV appears to occur in discrete steps for all three reforming agents. These steps correlate with well-defined changes in the spectroscopic data (Figure 5.7). Every experiment starts with a potential of $-1.29 \pm 0.02\ V$ following graphite formation from methane. Introduction of the reforming agent leads initially to a $0.30 \pm 0.04\ V$ decrease in OCV magnitude, and this change coincides with the disappearance of spectroscopically observable graphite. When O_2 is the reforming agent, this first rise is followed almost immediately by a second $+0.8\ V$ decrease to an OCV of $-0.15\ V$ measured at the end of the cycle. Accompanying this change in OCV is the appearance of NiO. For both H_2O and CO_2, the second rise is less dramatic and the approach to the OCV terminal limit of $-0.73\ V$ is more gradual. This slower, less pronounced change in OCV is reflected by the appearance and modest growth of NiO signal in the spectroscopic data.

The intermediate OCV of $-0.99 \pm 0.04\ V$ is more challenging to interpret. Given that this OCV result always accompanies the loss of observable carbon and given the transient nature of this $-0.99\ V$ result, we propose that this measured OCV reflects a temporary “equilibrium” where the relative redox partners on the anode surface are CO and CO_2.

5.7 $CO_{(g)} + O^{2-} \leftrightarrow CO_{2(g)} + 2e^-$

The standard potential of the CO/CO_2 equilibrium shown in reaction 5.7 at 700 °C is $-0.99\ V$,[48] matching exactly the value measured in our experiments. If this assignment is correct, then the result can be interpreted in terms of the carbon deposits being incompletely oxidized to form CO that then desorbed from the surface. The newly created CO now becomes the SOFC's "fuel". In a static system this newly created CO would establish an equilibrium between CO_2 (and solid carbon). However, because the anode is exposed to a continuous flow of Ar, CO is swept away so that the only redox couple that remains for the reforming agent is Ni/NiO and the OCV continues to climbs to its terminal limit.

Conclusions

Taken together, the spectroscopic and electrochemical data provide a compelling description of how reforming agents affect the condition of Ni-based cermet anodes in functioning SOFCs. Significant and reproducible discrepancies in carbon removal rates by H_2O, CO_2, and O_2 were observed in both spectroscopic graphite signatures and simultaneous changes in cell OCV. All three reforming agents tested in this work - H_2O, O_2, and CO_2 - remove carbon from SOFC anodes, but O_2 also behaves quite aggressively toward the anode, quantitatively oxidizing anode Ni surfaces within minutes. In contrast, H_2O and CO_2 both remove carbon deposits but only partially oxidize the Ni, showing that carbon removal by these two reforming agents is more benign on the anode than O_2.

Carbon removal rates were most rapid under H_2O, followed by O_2 and finally by CO_2. These results, when coupled with earlier work regarding oxygen dissociation on

catalytic Ni, are consistent with formation of adsorbed O intermediates as the rate-limiting step in carbon gasification. The consistently observed delay in carbon removal by oxygen may indicate that oxides stabilized by step edges must reach a threshold population before "spilling over" to react with adsorbed carbon. Once this spillover effect takes place, carbon oxidation happens rapidly. Subsequent Ni oxidation also occurs fastest and most extensively under O_2. Ultimately, these correlated spectroscopic and electrochemical results provide insights into the interactions of H_2O, CO_2, and O_2 with carbon species and the MEA anode structure, and these insights can drive better informed decisions in utilizing them as internal fuel reformates or carbon gasification agents.

CHAPTER 6

IN SITU OPTICAL STUDIES OF METHANE AND SIMULATED BIOGAS OXIDATION ON HIGH TEMPERATURE SOLID OXIDE FUEL CELLS

Contribution of Authors and Co-Authors

Manuscript in Chapter 6

Author: John D. Kirtley

Contributions: Contributed to most experiments in this work and led some, analyzed most data, wrote first draft and contributed to subsequent editions.

Co-Author: Dr. Daniel A. Steinhurst (Nova Research, Inc.)

Contributions: Assisted in many experiments, assisted in data collection and processing.

Co-Author: Dr. Jeffrey C. Owrutsky (Naval Research Laboratory)

Contributions: Provided helpful assistance through discussions and experimental advice, assisted in manuscript revisions.

Co-Author: Dr. Michael B. Pomfret (Naval Research Laboratory)

Contributions: Led and designed many of the experiments, analyzed some data, and assisted in manuscript revisions.

Co-Author: Dr. Robert A. Walker

Contributions: Provided helpful assistance through discussions and experimental advice, assisted in manuscript revisions.

Manuscript Information Page

John D. Kirtley, Daniel A. Steinhurst, Jeffrey C. Owrutsky, Michael B. Pomfret and Robert A. Walker
Physical Chemistry Chemical Physics
Status of Manuscript:
____ Prepared for submission to a peer-reviewed journal
____ Officially submitted to a peer-review journal
____ Accepted by a peer-reviewed journal
__x__ Published in a peer-reviewed journal

Published by © Royal Society of Chemistry
16, 2014

Introduction

Unlike internal combustion engines, electrochemical fuel cells are devices that produce electricity efficiently and, depending on cell design, from a wide variety of fuels.[10] These requirements of efficient energy conversion and fuel flexibility are central to any application intended to minimize carbon footprint and to accommodate variable operating conditions. Solid oxide fuel cells (SOFCs), in particular, show great promise because of operating efficiencies that can exceed 70% in combined heating and power applications as well as their ability to function with diverse fuel stocks including H_2, syngas, traditional hydrocarbon fuels and renewables.[10, 12, 146]

Of the renewable fuels that are potential sources of SOFC produced electrical power, biogas is relatively simple. Consisting primarily of CH_4 and CO_2, biogas is produced by anaerobic fermentation of organic matter. The relative amounts of CH_4 and CO_2 in a biogas supply can vary, but typical concentrations range from 50–70% CH_4 by volume. Other species such as hydrogen sulphide, ammonia, and nitrogen can be present in trace amounts.[32, 43, 146, 147]

One challenge associated with using biogas in SOFCs is uncertainty about the mechanism(s) responsible for chemical oxidation and those that lead to anode degradation and eventual device failure. Despite relatively simple chemical composition, biogas mixtures are capable of undergoing a number of reactions at the anode. In the limit of high CH_4 content with no CO_2 in the fuel stream, CH_4 will react within a SOFC anode under load with oxide ions diffusing through the electrolyte to form CO_2 and H_2O:

6.1a $\quad CH_4 + 2O_2 \rightarrow CO_2 + H_2O$ (net)

6.1b $CH_{4(ads)} + 4O^{2-} \rightarrow CO_{2(g)} + 2H_2O_{(g)} + 8e^-$ (anode)

6.1c $2O_{2(ads)} + 8e^- \rightarrow 4O^{2-}$ (cathode)

CH_4 will also dissociatively chemisorb on a Ni anode surface to form adsorbed carbon and hydrogen,[91, 148, 149] a problem exacerbated in the absence of current loading. The adsorbed hydrogen can then recombine and desorb as H_2, leaving the carbon on the surface.

6.2 $CH_{4(ads)} \rightarrow C_{(ads)} + 2H_{2(g)}$

Carbon formation (or ‘‘coking’’) on SOFC anodes is a primary cause of SOFC degradation.[91, 95, 150] Recent in operando optical studies of SOFCs operating with CH_4 have shown that this fuel forms primarily highly ordered graphitic carbon on Ni cermet anodes.[93, 118]

The addition of CO_2 to the fuel stream makes biogas chemistry more complicated. On the surface of a catalyst (e.g. Ni), CH_4 and CO_2 can react with each other to produce CO and H_2:[146]

6.3 $CH_{4(ads)} + CO_{2(ads)} \rightarrow 2CO_{(g)} + 2H_{2(g)}$

Adsorbed species may also react *via*:[91, 151]

6.4 $2CO_{(ads)} \rightarrow C_{(ads)} + CO_{2(g)}$

6.5 $C_{(ads)} + CO_{2(ads)} \rightarrow 2CO_{(ads)} \rightarrow 2CO_{(g)}$

Note that along with eqn 6.3 – 6.5 occurring, coking can still occur through CH_4 decomposition (eqn 6.2). CO can also form carbon through the well-known Boudouard reaction (eqn 6.4). However, CO_2 provides mechanisms for carbon deposited by CH_4 to be removed (eqn 6.5). Identifying how these individual processes affect SOFC

performance and durability requires being able to observe those species present on both the anode surface and in the gas phase while discovering how relative surface coverages and concentrations change with various operating conditions including fuel composition and device load. Kinetic models have been developed to describe the fate of biogas in functioning SOFCs, but conclusions from these studies are based solely on calculated quantities or from experimental data acquired from indirect measurements.[14, 57, 58, 152] Methods that probe directly the extent of surface reforming, electrochemical oxidation, and carbon deposition are limited.

A lack of experimental methods capable of observing chemical change directly in operando hampers efforts to quantify and predict the chemistry occurring on SOFC anode surfaces, largely because SOFCs operate at temperatures in excess of 700 °C under nonequilibrium conditions. Electrochemical techniques can probe reduction/oxidation potentials and monitor overall device performance.[65, 153] Temperature programmed oxidation/reduction experiments can identify ex situ species that evolved from chemistry occurring on the anode surface.[55, 90] Additional techniques such as scanning electron microscopy,[55, 154] X-ray nano tomography for 3D imaging,[155] and X-ray photoelectron spectroscopy (XPS)[156] can reveal post mortem changes in structure and composition that occurred during operation. A recent report has shown how XPS can measure changes in atomic oxidation states across the TPBs of functioning SOFCs, but these experiments are carried out at gas phase pressures of ~ 1–2 Torr.[100] None of these methods cited above are capable of identifying the chemical transformations that occur in devices operating

under typical conditions, which would provide information more directly related to device performance.

Recent advances in understanding SOFC chemistry have emerged from the development of in situ optical methods.[61, 62, 76] IR imaging of SOFC anodes was first demonstrated by Brett et al. In these experiments the authors used an InSb array detector with ~500 mm spatial resolution to observe the mid-IR emission from polarized and unpolarized gadolinium doped ceria pellets at 600 °C. More recently, Owrutsky and coworkers have employed Si-based cameras to monitor the near-IR (NIR) emission from SOFCs operating at temperatures up to 800 °C.[62] With spatial resolution of ~ 100 μm and the ability to resolve temperature differences of ~ 0.1 °C, NIR imaging experiments have monitored thermal gradients across SOFC anodes operating with hydrocarbon and oxygenated carbon-based fuels. These studies have identified and characterized a variety of reactions, including endothermic fuel cracking and reforming, and exothermic electrochemical oxidation. Additionally, thermal studies have been able to elucidate information about carbon growth on the anode through changes in apparent emission that lower the perceived anode surface temperature. As such, NIR imaging is a viable complement to other analytical tools used in the study of SOFCs.

The first report of vibrational Raman spectra from functioning SOFCs appeared in 2007, when Pomfret et al. measured the appearance and disappearance of carbon from Ni-cermet anodes operating with butane at 715 °C.[61] Since that report, the effects of other fuels on SOFC performance and anode stability have also been studied, including those for saturated and unsaturated low molecular weight hydrocarbons, methanol, and

molecular hydrogen.[52, 93, 118, 137] In related work, Brandon and coworkers have shown that Raman scattering is effective for probing the properties of materials commonly used in SOFC applications as a function of temperature and local redox conditions.[81] More recent applications of Raman scattering by Liu and coworkers have mapped the distribution of carbon formation on Ni anodes,[74] identified the effects of sulfur contaminants on SOFC anodes[157] and quantified how much coke forms on anodes as a function of exposure to different fuels.[74]

Due to the high operating temperatures of SOFCs, adsorbates and materials will have some fraction of their population in excited vibrational states that can produce state specific emission in the mid-IR. Liu and coworkers made Fourier transform IR emission spectroscopy (FTIRES) measurements of samarium and strontium doped cobalt oxide SOFC cathodes at 550 °C and reported the formation of O_2^- and O_2^{2-} as a function of cell polarization.[78] More recently, Pomfret and coworkers have observed IR emission from anode supported SOFCs and assigned features in the spectra to surface physisorbed CO_2 ($CO_{2(ads)}$) as well as gas phase CO and CO_2.[77] These studies illustrated the ability of FTIRES to provide insight into fuel utilization mechanisms. The assignment of the $CO_{2(ads)}$ species marked the first in situ identification of an anode oxidation intermediate in a working membrane electrode assembly (MEA), positioning FTIRES as one of the more important techniques for determining the carbon-based fuel mechanisms.

Experiments described below couple these three recently developed optical methods to examine the in situ chemistry occurring on SOFC Ni-cermet anodes operating with CH_4 and simulated biogas (CH_4–CO_2) mixtures at 800 °C. Specifically, vibrational

Raman scattering, NIR thermal imaging, and FTIRES all provide complementary information about the chemical composition and working condition of anodes exposed to fuel at open circuit voltage (OCV) and under polarization. Together, these techniques identify material changes occurring with ~ 10 s temporal resolution (Raman), thermal gradients across the surface with ~ 0.1 °C thermal resolution, 100 μm spatial resolution and 200 ms temporal resolution (NIR thermal imaging) and steady-state CO_x surface intermediates and products that appear while carbon is electrochemically oxidized (FTIRES). Coupling observations from these three different methods with electrochemical data that quantify cell performance lead to unprecedented insight into the effects that surface reforming, carbon deposition, and electrochemical oxidation have on SOFC performance.

Methodology

Experimental Assembly and Sample Preparation

MEAs were purchased from Materials and Systems Research, Inc. and are composed of a thick Ni/yttrium-stabilized zirconia (YSZ) anode support layer (~ 0.8–1 mm), a Ni/YSZ anode functional layer (12–25 mm), a 8–10 mm thick YSZ electrolyte, and a 15 mm lanthanum strontium manganite (LSM)/YSZ cathode functional layer and a 50 mm thick LSM/YSZ cathode. Further details regarding cell fabrication and characterization can be found elsewhere.[158] Gold electrode leads were attached with gold ink and gold mesh (Alfa Aesar) (BASF or Heraeus) to the anode and Pt ink (Heraeus) and Pt mesh (Alfa Aesar and Sigma Aldrich) to the cathode and MEAs were pasted to a 25.4 mm diameter alumina tube (Sentro Tech) using alumina paste (Aremco), as previously

reported.[159] Further preparations differed according to experimental technique. Those MEAs tested exclusively with NIR thermal imaging and with FTIRES were enveloped with a second alumina tube/sapphire window (Swiss Jewel Co.) assembly; the sapphire window was sealed to the alumina tube with alumina paste. The opposite end was sealed with RTV paste (Permatex, UltraCopper).[159] Those MEAs tested exclusively with Raman spectroscopy and sometimes simultaneously with NIR thermal imaging were surrounded by a quartz tube capped with a silicone stopper. Full details of the experimental systems used in these experiments have been described in previous reports.[52]

Electrochemical Measurements

Electrochemical measurements were performed using either a Gamry Reference 3000 Potentiostat/Galvanostat/ZRA or a Princeton Applied Research VersaStat MC. OCV measurements were made at various times throughout the experiment to test overall MEA condition and monitor for leaks between the cathode and anode. Initial benchmark measurements were performed with linear sweep voltammetry (LSV); subsequent tests were performed to assess cell performance prior to each experimental sequence (described below). LSV measurements were taken at 0.1 $V\ s^{-1}$ from OCV to 0 V (I_{max}). Fuel flows during all benchmark tests were 150 mL min^{-1} Ar and 100 mL min^{-1} H_2 at the anode. Operational cathode flows were held constant at either 85 mL min^{-1} air or 20 mL min^{-1} O_2 and 65 mL min^{-1} Ar throughout the entire experiment. Chronopotentiometric measurements were also acquired and compared directly to spectroscopic data.

Near-Infrared Thermal Imaging

High-resolution NIR thermal images were collected with a CCD camera (AVT, Stingray F033B ASG) equipped with an 18-108 mm focal length macro zoom lens (Navitar Zoom 7000). A long pass filter (Hoya R72) was used to block ambient and emitted visible light below 720 nm. Further details may be found in previous publications.[62, 159] In these experiments, individual images encompassing most or all of the MEA were collected at a repetition rate of 5 Hz, with ~100 μm resolution and ~0.1 °C temperature resolution. Images were collected concurrently with electrochemical measurements and in many experiments, Raman spectra and NIR images were collected simultaneously (Figure 6.1). Measured intensities were calibrated and converted to temperatures using LabView v8.5 and in-house software. A detailed image of the MEA with the components labelled is available in Appendix C, Figure C.1.

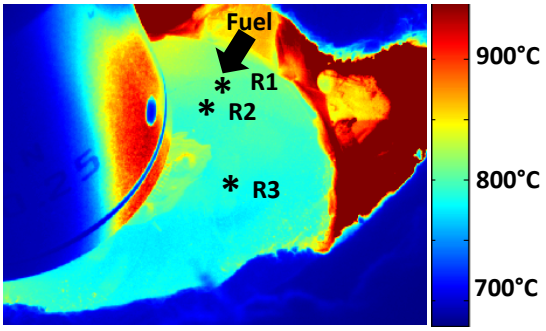

Figure 6.1 NIR thermal image collected simultaneously with Raman measurements. R1-3 depict representative regions where temperatures were averaged and tracked. All NIR thermal images have been false-colored.

Vibrational Raman Scattering

Raman measurements were collected in operando using customized optics described previously.[60] A 488 nm Ar-ion laser excitation source (~24 mW) was focused onto the anode surface via a 10x long working distance objective. The sampling area was approximately 2 mm in diameter. Backscattered light was passed into a Renishaw InVia spectrometer, through an edge filter and onto a CCD detector. In these studies, time-dependent spectra were acquired continuously in 10 s increments across a frequency window extending from 800 cm^{-1} to 1800 cm^{-1}.

Fourier Transform Infrared Emission Spectroscopy

Infrared radiation emitted from the hot MEA anode surface was measured directly by a FTIR spectrometer (Mattson Instruments, Inc., Model #: RS-1000) with the internal emission source disabled and removed from the optical path.[77] The MEA-furnace assembly is aligned such that emitted radiation passes directly from the MEA, through two sapphire windows onto the optical path of the spectrometer and to the detector. The entire optical path length is sealed and continuously purged with N_2 gas to eliminate as much ambient CO_2 interference as possible. Each FTIR spectrum shown in this work represents 16 averaged scans, with 0.5 cm^{-1} resolution, and was measured from 5000–500 cm^{-1} (we note, however, that the sapphire window interferes with spectra recorded below 1550 cm^{-1}). Spectra were recorded every 200 s to ascertain changing gas and surface species as a function of fuel flow and polarization. Prior to each experimental sequence, a reference spectrum was acquired and used as a baseline subtraction from experimental data. Further post-processing of the FTIRES spectra was required, because the N_2 purge

of the FTIR spectrometer was incomplete. Emission spectra showed interference due to absorption from a small amount of room temperature CO_2 (~1 ppm) remaining in the FTIR spectrometer. A standardized room temperature CO_2 spectrum was fit to the observed absorption – appearing as negative-going signal in emission spectra – and subtracted to eliminate the interference.

Experimental Sequence

In the studies presented below, an experiment describes measurements performed using a single MEA, and each experiment consisted of at least five individual trials. Observations were reproducible although absolute values (I_{max} with H_2, for example) might vary by < 10% between experiments. MEAs were heated to the operational temperature (800 °C) at 1 °C min^{-1} or slower with the anode under an Ar flow of 150 mL min^{-1} and the cathode under an air flow of ~85 mL min^{-1}. The specific sequence of measurements within a trial was as follows:

- Perform electrochemical LSV measurements under 100 mL/min H_2 and 150 mL/min Ar at the anode. Following benchmarks, H_2 flow was reduced to 20 mL/min and allowed to stabilize for 10 min.
- Initialize hydrocarbon fuel flow, terminate H_2 fuel flow, and maintain the hydrocarbon flow for 10 min while holding the cell load at OCV, 25 % I_{max}, 50 % I_{max}, or 75 % I_{max}. MEA electrochemical potential was monitored throughout the fuel flow while spectroscopic (Raman, NIR imaging, and/or FTIRES) signatures were monitored and recorded. Anode flows during sequences with methane (CH_4) fuels

were: 25 mL min^{-1} CH_4 and 150 mL min^{-1} Ar. Sequences with simulated biogas flows were: 25 mL min^{-1} CH_4, 25 mL min^{-1} CO_2, and 150 mL min^{-1} Ar.

- Initialize 20 mL min^{-1} H_2 flow, stop hydrocarbon fuel flow and restore cell to OCV. Continue to purge anode chamber with 150 mL min^{-1} Ar and 20 mL min^{-1} H_2 for 10 min.
- Stop H_2 flow, polarize the cell at 2/3 I_{max} for 10 min under 150 mL min^{-1} Ar to electrochemically oxidize carbon deposits.
- Restore the MEA to benchmark conditions.

The first fuel exposure was always performed at OCV. The sequence of operational loads (OCV, 25% I_{max}, 50% I_{max}, or 75% I_{max}) for the following four trials were chosen at random to prevent systematic errors due to MEA degradation.

Results

MEA Performance under Methane and Biogas

The performance of each MEA tested with CH4 and biogas was monitored using LSV. Fig. 6.2 shows representative LSV traces for both fuels. The most striking differences between the two fuels are the differences in OCV and the *V–I* slope at low currents. OCV with CH_4 is 1.30 *V* and ~0.2 *V* higher than that measured with biogas (1.12 *V*). Similarly, the measured maximum power (Figure 6.2, dashed traces) is higher with CH_4 (134 *mW*) than with biogas (119 *mW*). For reference we include data for the cell operating with dry hydrogen. OCV under dry hydrogen is 1.18 *V*.

Experiments performed with equivalent MEAs confirmed that these differences were real and not associated with variability of individual assemblies. Diminished OCV

values with increased CO_2 partial pressures have also been reported by Eguchi and coworkers.[160] We speculate that these differences may be due to the tendency of CH_4 to form modest amounts of carbon on SOFC anodes as CH_4–CO_2 mol fractions increase, particularly under OCV. Carbon deposition on a Ni cermet anode leads to a measured OCV of 1.30–1.32 *V*. Furthermore, a small amount of carbon within an anode's microstructure has been shown to temporarily improve cell performance by providing a conducting bridge between disconnected portions of the cermet network.[96, 97]

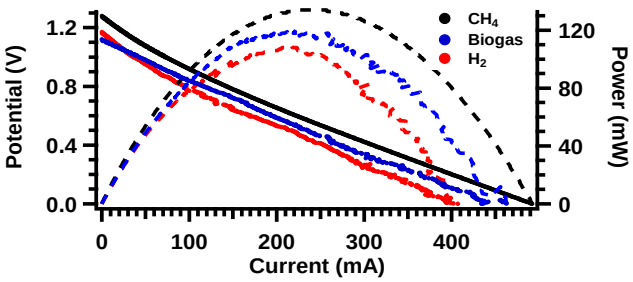

Figure 6.2. MEA performance under CH_4 and biogas fuels at 800 °C. The V-I trace (solid) and P-I trace (dashed) indicate slightly better performance under CH_4 fuels. A result under H_2 fuel is shown for reference.

Thermal Diagnostics of Oxidative Processes

Thermal images of anode surfaces exposed to the two fuel feeds reveal striking and detailed differences in the temperature profiles. Figure 6.3 shows temperature gradients present across the anode surface of an MEA held at OCV after ~600 s of exposure to CH_4 (a) or biogas (b). These images show minimal cooling under CH_4 while exposure to biogas led to pronounced cooling, especially near the inlet. These observations highlight two important results: first, fuel flow across the anode with this assembly is distinctly inhomogeneous[161] and second, the biogas fuel mixture appears to

be much more chemically active on the surface than CH_4, even when the device is held at OCV. We note that prior to passing over the anode, both gas fuel feeds are heated to in operando temperatures due to their passage through the furnace.[62]

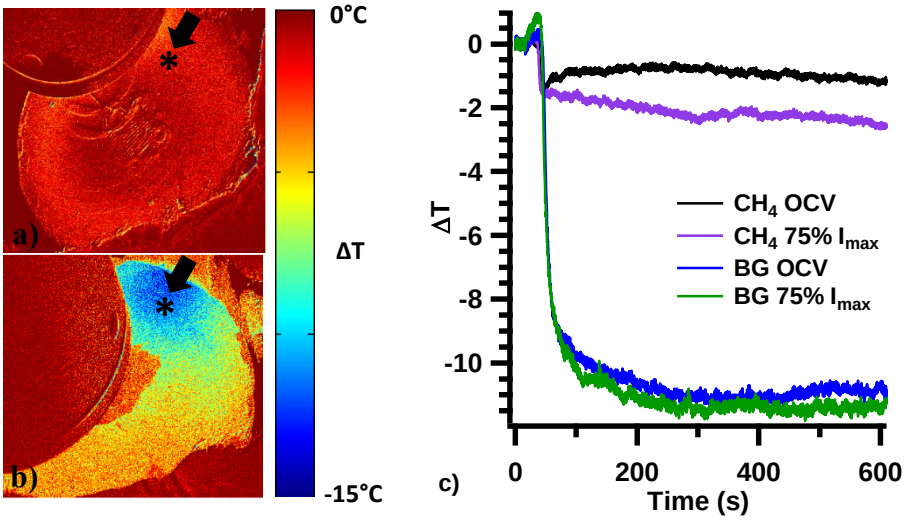

Figure 6.3. NIR thermal images of MEAs after ten minutes of operation at OCV with CH_4 (a) and biogas (b). Images were obtained by subtracting raw images (e.g. Fig. 6.1) from a baseline image collected before the addition of either fuel. Arrow represents directional fuel flow; asterisk represents sampling area. ΔT (center bar) indicates cooling relative to initial MEA temp, from 0 °C ΔT to -15 °C. In (c), ΔT is depicted as a function of time under different fuels and applied loads. Temperature drop (due to endothermic fuel oxidation) was measured near the inlet as indicated by the asterisk in (a-b).

To better quantify temperature changes as a function of MEA surface position, the average temperatures of several surface locations were monitored and recorded from each experiment. A representative collection of locations are noted in Fig. 6.1 and data from different locations are shown in Appendix C (Figure C.2), and are taken from the same trial as Fig. 6.3b. In general, the largest temperature differences were seen near the inlet for both fuels. Data reported in Fig. 6.4 were obtained by averaging temperatures measured in a small sample area between the inlet and gold current collector (see

asterisks, Fig. 6.3). These data exemplify the large cooling effect of biogas relative to CH_4. MEAs at OCV under CH_4 demonstrated a temperature drop of 1–4 °C. Under biogas, temperatures dropped 12–14 °C. These findings are consistent with recent reports that show CH_4 to be relatively inactive and biogas mixtures to be capable of inducing changes of up to 25 °C on SOFC anodes.[37, 75]

Interestingly, polarizing the cell to 75% I_{max} under CH_4 cooled the MEA surface 1–2 °C more than at OCV, but a similar cell polarization with biogas led to no measurable difference in anode surface temperature (Fig. 6.4). This behavior was reproducible: on average, an MEA experienced 1.4 °C more cooling at maximum current loading. The reason for this difference is unclear.

Electrochemical conversion of fuel to products is exothermic, so conversion of CH_4 to CO_2 and H_2O (drawing a current of 0.75 I_{max}) should lead to a net heating of the anode. Observed cooling implies more complicated surface chemistry than simple electrochemical oxidation at the anode three-phase boundary. Several possible explanations will be explored in the Discussion. Spectroscopic data presented below imply that differences in the effects of anode polarization on surface temperature result from incomplete carbon oxidation and extensive surface reforming.

In Situ Spectroscopic Evidence of Graphitic Carbon

Thermal imaging data shown above provide a component level perspective of changes that occur across a SOFC anode exposed to fuel and subject to polarization. Thermal imaging, however, cannot identify the material specific origins responsible for observed temperature gradients. Of particular concern is whether or not carbon

containing fuels are forming deposits within the anode microstructure. Given that carbon nucleation and growth can ultimately lead to MEA failure, the extent and reversibility of carbon formation are important considerations when evaluating SOFC durability.

Concurrent with the thermal imaging measurements presented above, vibrational Raman spectroscopy was used to acquire vibrational spectra of the SOFC anodes as a function of fuel identity and polarization. Fig. 6.4a shows spectra acquired from a typical Ni/YSZ MEA operating at OCV and 75% I_{max} with CH_4, biogas, and hydrogen fuels. The vibrational band that appears at 1556 cm^{-1} under continuous CH_4 exposure is assigned to highly ordered sp^2-hybridized graphitic domains and is labeled as the ‘‘G’’ vibrational mode in accordance with literature. Absent in the spectra is intensity near 1350 cm^{-1} that would correspond to the ‘‘D’’ mode and indicate a higher density of grain boundaries and/or site defects in the carbon deposits. Little or no detectable carbon is observed from anodes exposed to biogas, strongly implying that the steep gradients observed in the thermal imaging experiments arise from dry CH_4 reforming occurring on the anode surface. Further evidence of this phenomenon can be seen with FTIRES spectra presented in the next section; a more complete development of the observed phenomena is presented in the Discussion.

A plot of the ‘‘G’’ peak intensity from MEAs exposed to CH_4 and biogas at OCV and 75% I_{max} is shown in Fig. 6.4b. While G-peak intensities under CH_4 were independent of polarization and remained low relative to earlier studies performed at cooler temperatures[118] and with different MEAs, they stand in striking contrast to observations made under biogas. For all MEAs tested under biogas, Raman spectra

showed little if any observable carbon being formed on the anode surface. For comparative purposes, intensities of a 1556 cm^{-1} ‘‘peak’’ measured in the absence of carbon fuel are shown in Fig. 6.4a and b (H_2 traces). Subsequent FTIRES experiments described below provide evidence that biogas does lead to some carbon deposition, but the amount of carbon formed is below the detection limits of the vibrational Raman measurements.

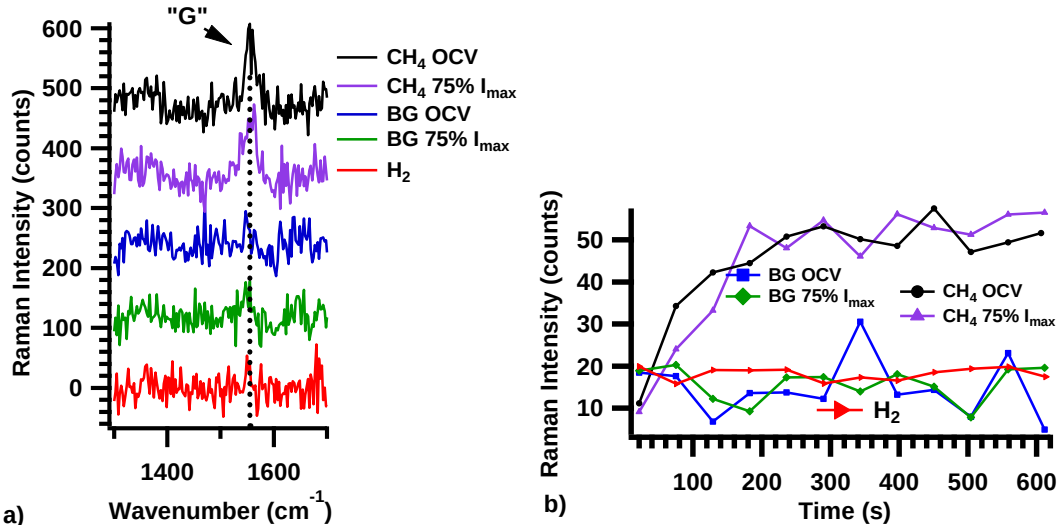

Figure 6.4 (a) Raman spectra of the graphite ‘‘G’’ peak acquired after ten minutes of CH_4 or biogas exposure at the anode (800 °C) under OCV and under polarization. Data have been vertically offset and baseline corrected for clarity; (b) the growth of the ‘‘G’’ peak during the ten minutes of fuel flow. Data have been smoothed for clarity.

One surprising observation from the vibrational Raman spectra is that the amount of carbon formed by CH_4 on the anode does not seem to depend on cell polarization. In principle, one might expect that drawing relatively high currents should inhibit deposit formation. Data from Fig. 6.4b, however, suggest otherwise. We propose that the carbon formed by CH_4 decomposition is being formed on the Ni surface away from an active

three phase boundary. These spectroscopic observations – CH_4 forms measurable amounts of carbon whereas biogas does not – correlate well with electrochemical data. Following trials with CH_4, MEA performance as measured by P_{max} dropped by up to 10% (especially under high current loading) whereas benchmark measurements of cell performance following biogas sequences showed no evidence of systematic degradation.

Gaseous and Physisorbed
Species Observed *In Situ*

While observations from NIR thermal imaging and Raman spectroscopy show correlations between anode surface temperatures, carbon formation, and reforming reactions, a detailed description of the mechanisms describing fuel oxidation and carbon formation from CH_4 and biogas remains speculative. FTIRES of functioning devices provides additional insight into gaseous species and intermediates physisorbed to the anode. Figure 6.5a shows emission intensities from species present on and near the anode while a MEA is operating at 75% I_{max} under CH_4. This spectrum contains features representative of gas species that can be observed in situ: CH_4 (3007 cm^{-1}), CO_2 (2365 cm^{-1}), and CO (2094 cm^{-1}). Reported frequencies refer to ro-vibrational band centers.

In addition to the gas phase species observed in the IR emission, the spectrum also contains signature emission assigned to $CO_{2(ads)}$ near 2290 cm^{-1}. We note this is physisorbed rather than chemically-bound-CO_2 interacting with Ni surfaces and likely corresponds to relatively small, steady state surface coverages; the amount of physisorbed CO_2 also depends both on cell polarization and composition of the anode gas stream. This assignment is based on the first report of Pomfret et al.[77] that observed this physisorbed intermediate on a Ni/YSZ anode *in situ*. Several literature reports also confirm this

assignment.[162-164] We note also that this band lacks rotational structure, indicative of surface species.

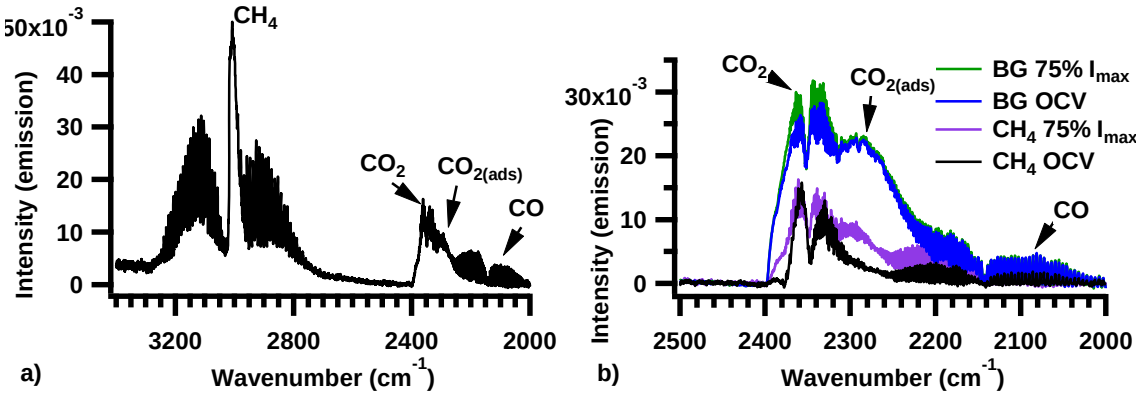

Fig. 6.5 Emission spectrum acquired during CH_4 fuel flow under 75% I_{max} at 800 °C (a). In (b), emission features changed with fuel and polarization at 800 °C in the CO_x region. Traces have been background corrected.

Focusing on the window from 2000 – 2400 cm^{-1} more clearly illustrates how SOFC anode chemistry depends upon fuel identity and polarization conditions. Figure 6.5b shows FTIRES data from devices operating with CH_4 and biogas under both polarized and OCV conditions.

Several observations from Figure 6.5b stand out. First, gas phase CO_2 and CO are present in all spectra, even in instances where these species are not expected (such as CH_4 at OCV). Second, physisorbed CO_2 shows no polarization-dependent change in surface coverage under biogas but increases noticeably under CH_4 when the device is polarized. Third, polarizing the anode leads to more gas phase CO_2 being produced from both CH_4 and biogas relative to OCV conditions, and significantly more gas phase CO produced from CH_4. These observations are summarized in Figure 6.6.

The most surprising observations in the FTIRES data in Fig. 6.5b are the signals from gas phase CO_2 and CO from anodes exposed to CH_4 at OCV. In the absence of any polarization, we would expect virtually all of the CH_4 to pass through the anode chamber unchanged and what CH_4 did react (through catalytic C–H bond activation on Ni surfaces) should form carbon deposits. Several possible explanations may account for $CO_{2(g)}$ and $CO_{(g)}$ in the CH_4-OCV FTIRES spectra. In principle, CO_2 observed in the FTIRES data from CH_4 at OCV could reflect errors introduced by background corrections, but if this were the case spectra should not show similar results for CO because of the large differences in ambient CO_2 and CO concentrations. Gas phase CO_x species may be the result of surface chemistry. Nonspecific, heterogeneous surface chemistry may result from CH_4 reacting with available oxides on YSZ, alumina (paste), or window surfaces. If this mechanism is the source of CO_x species observed in the FTIRES data, then we expect that the CO_2 and CO responses will diminish over time as the amount of available surface oxides decreases. A second source of oxide that can lead to CO_x formation is the small oxide flux moving from the cathode to the anode due to the large P_{O2} gradient that exists between the two sides of the MEA. The absence of any $CO_{2(ads)}$ signal in the case of CH_4 at OCV implies that any surface chemistry that does occur must also result in rapid desorption of products so that the steady state surface coverage of intermediates remains low.

Figure 6.6 illustrates how the species' concentrations change under current loading and fuel. We note that trends indicated in each of the four panels show only results for tests under OCV and maximum polarization (75% I_{max}) for clarity. However,

trends noted below are consistent with those observed at intermediate polarizations (25% I_{max} and 50% I_{max}) as well. First, CH_4 intensity under a CH_4 feed is much higher relative to that observed under biogas fuel, despite the fact that the partial pressures of CH_4 in both systems are similar (Figure 6.6a). If the amount of CH_4 observed in the FTIRES data scaled with partial pressure, then the CH_4 signal with biogas should be ~85% of the signal with a simple CH_4 feed. Instead, the observed CH_4 signal in the biogas feed diminishes almost 3-fold, indicating that dry CH_4 reforming (with CO_2) plays an important role in controlling the fuel composition within the anode chamber. This observation agrees with findings from the thermal imaging experiments, where exposure to biogas resulted in significantly more MEA cooling at OCV. Both of these phenomena speak of the much higher conversion efficiency of CH_4 in biogas fuels relative to that in neat CH_4 fuels. Indeed, previous studies have shown that catalytic decomposition of CH_4 on a Ni/YSZ anode is on the order of only 0.3%.[118]

A second observation from polarized cells is that $CO_{2(ads)}$ intensities increased significantly when anodes under CH_4 fuel were polarized, but $CO_{2(ads)}$ intensity remained insensitive to anode polarization under biogas (Figure 6.6c). This observation is especially evident in Table 6.1, where intensities have been normalized to OCV conditions at 100 s of fuel exposure for each fuel. Note from Fig. 6.6 that $CO_{2(ads)}$ signals were much larger under all circumstances with biogas than with CH_4. Biogas $CO_{2(ads)}$ signals that are large and invariant to polarization imply that the CO_2 initially present in biogas saturates all available binding sites. Growth of $CO_{2(ads)}$ on polarized anodes under

CH_4 is evidence of electrochemical conversion and the growth of a steady state concentration of CO_2 intermediates on the Ni surface.

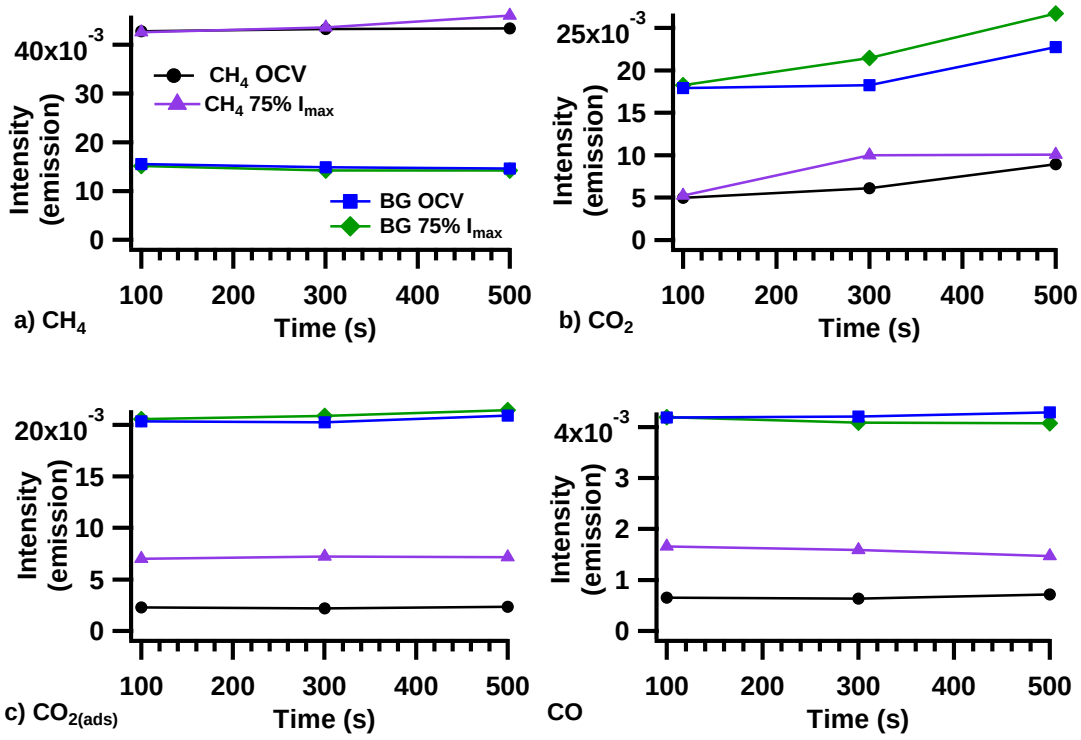

Figure 6.6. FTIR emission intensities of (a) CH_4, (b) $CO_{2(g)}$, (c) $CO_{2(ads)}$, and (d) $CO_{(g)}$ during SOFC operation at 800 °C with CH_4 at OCV (circles) and 75% I_{max} (triangles) and biogas at OCV (squares) and 75% I_{max} (diamonds).

Third, gas phase CO_2 intensities are higher with polarized anodes under both CH_4 and biogas (Figure 6.6b). This result can be understood in terms of fuel utilization. When polarized, anodes operating under either fuel produce CO_2 through electrochemical oxidation. However, while gas phase CO increases significantly when anodes are polarized under CH_4 fuel, gas phase CO signals from anodes under biogas show no polarization dependence (Table 6.1). Note again that the much higher $CO_{(g)}$ intensity observed under biogas relative to CH_4 fuel speaks to the much higher conversion

efficiency of CH_4 in biogas (Figure 6.6d). The behavior of the incompletely oxidized species serves as a clear indication that two distinguishable fuel utilization processes are occurring with the different fuels. With CH_4 the relative amounts of $CO_{2(ads)}$ and CO correlate directly with electrochemical oxidation. In contrast, the dominant contribution to CO production in biogas is dry reforming of CH_4.

IRSpecies (time)	Methane Fuel		Biogas Fuel	
CH_4	*OCV*	*75%*	*OCV*	*75%*
(100 s)	1.00	1.00	1.00	0.98
(300 s)	1.01	1.02	0.96	0.91
$CO_{2(g)}$				
(100 s)	1.00	1.06	1.00	1.02
(300 s)	1.23	2.01	1.02	1.20
$CO_{2(ads)}$				
(100 s)	1.00	3.08	1.00	1.01
(300 s)	0.96	3.17	1.00	1.03
$CO_{(g)}$				
(100 s)	1.00	2.54	1.00	1.01
(300 s)	0.97	2.43	1.01	0.98

Table 6.1. FTIRES intensity, normalized against intensity measured at OCV and 100 s. Normalized intensities of each species vary as a function of fuel, fuel exposure time, and polarization.

Electrochemical oxidation of graphitic deposits following fuel flow provides further evidence of extensive graphite formation under CH_4 fuel, and much less under biogas. FTIRES spectra collected during electrochemical oxidation of graphite show significant concentrations of CO_x produced by oxide reaction with $C_{(s)}$ (Figure 6.7a). Based on emission intensities, much more $CO_{2(g)}$ and $CO_{(g)}$ were produced following CH_4 exposure relative to biogas exposure. The dependence of $CO_{2(g)}$ intensities on previous fuel and polarization conditions can be seen more quantitatively in Figure 6.7b. In addition to the CH_4 vs. biogas comparison, the trends also show that more $CO_{2(g)}$ was produced after fuel exposure under polarization. This trend was often reversed for other

CO_x species. The reasons for these unexpected dependencies on polarization remain ambiguous but may indicate (1) that electrochemical operation promotes carbon formation in the active layer of the anode (where Raman spectroscopy cannot directly probe), or (2) different electrooxidative pathways are responsible for graphite removal, indicating different regimes of carbon formation that are polarization dependent.

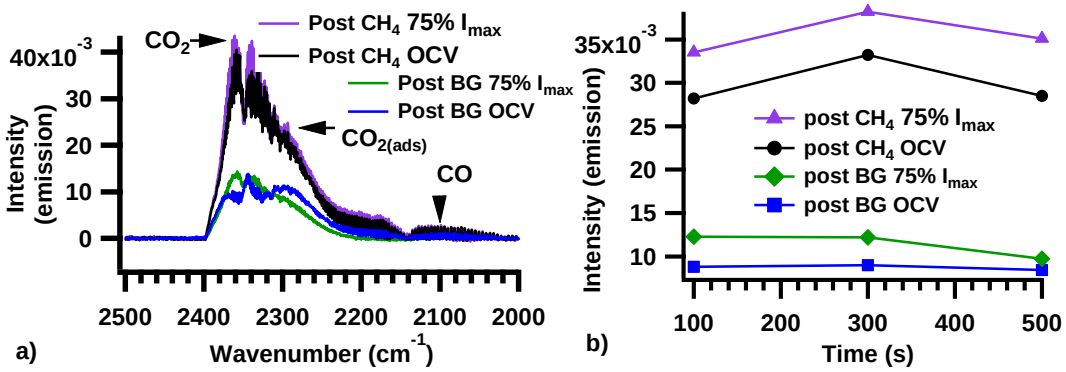

Figure 6.7. Qualitative differences in various CO_x species present can be seen when electrochemically oxidizing a pre-coked MEA (a). Gaseous CO_2 is the most pervasive, especially after exposure to CH_4 fuel at OCV (circles) and 75% I_{max} (triangles). Gaseous CO_2 levels were lower under BG fuel at OCV (squares) and 75% I_{max} (diamonds) (b).

Discussion

Complementary data from NIR imaging, Raman spectroscopy and FTIRES correlate changes in anode temperatures with changes in anode surface composition. Together these observations create a cohesive description of the mechanisms responsible for fuel utilization as a function of fuel composition. While NIR imaging is limited to reporting thermal changes without chemically specific information, Raman spectroscopy and FTIRES both identify chemical and material species present on the anode surface and in the gas-phase as a function of MEA polarization. Spectroscopic assignments allow

specific oxidation and reforming pathways to be assigned directly. These pathways, in turn, provide important confirmation of overall reaction schemes that describe how SOFCs operate with both CH_4 and biogas.

Thermal images acquired during fuel exposure reveal that the anode surface cools, meaning that endothermic reactions are dominant. These effects can be understood in terms of fuel utilization efficiencies and the thermodynamics of fuel conversion. Two types of chemistry are relevant for anodes exposed to CH_4 and biogas at OCV: carbon formation (or ‘‘coking’’) and dry CH_4 reforming (eqn 6.2 and 6.3 from Introduction).[75] The associated ΔH_{rxn} of these reactions at 1100 K are +90 kJ mol^{-1} and +259 kJ mol^{-1}, respectively.

Both reactions are endothermic, but biogas reforming should have a much stronger effect on anode temperature. The very minor surface cooling associated with CH_4 fuel decomposition is likely due in part to the low conversion of gas phase CH_4 to carbon deposits.[118, 165] We note that dry CH_4 reforming could also lead to carbon formation through the well-known Boudouard reaction (eqn 6.4), but this process is exothermic (-170 kJ mol^{-1}). The strong cooling effects observed with biogas suggest that most if not all, of the CO that forms from reactions between CH_4 and CO_2 desorbs from the surface. Another mechanism that would promote further cooling is reverse Boudouard chemistry. In this scenario, any carbon deposits that did form on the anode (from CH_4 decomposition, for example) could react with incident CO_2 to form two equivalents of CO, a process that would be 170 kJ mol^{-1} endothermic.

In cells operated with biogas, eqn (6.3) is likely to dominate the surface chemistry as Ni is known to be an outstanding CH_4 dry reforming catalyst. Previous work by Sumi and coworkers has shown steam reforming to be an effective strategy for mitigating carbon formation on Ni surfaces.[160] Furthermore, optical studies have provided strong evidence of exothermic oxidation reactions involving CO and H_2 from steam reformed fuels.[161] This chemistry does not dominate the dry reforming reactivity observed in our studies. Steam reforming is known to occur in the gas phase at high temperatures with a ΔHrxn of +226 kJ mol^{-1},[166] but dry reforming always requires a catalyst. Thus, we proposed that the endothermicity of dry reforming more directly affects the anode surface temperature and overcomes the heating effects of fuel oxidation when the cells are polarized. Equation 6.2 is the primary reaction that controls CH_4 fuel-anode chemistry under OCV conditions. Given that eqn 6.2 is less endothermic than both eqn 6.3 and the reverse Boudouard reaction, carbon formation from CH_4 leads to only a small amount of cooling. Once the cell is polarized, CO_2 and H_2O are produced electrochemically, and these can promote surface reforming reactions that further cool the anode surface.

Raman spectra show clear differences between CH_4 and biogas in terms of each fuel's tendency to form carbon deposits. CH_4 forms a small amount of carbon relative to the deposits observed with other hydrocarbon fuels, but these CH_4-formed deposits are more pronounced than any carbon formed from biogas. Carbon deposits formed by CH_4 are highly ordered graphite. The carbon that forms from CH_4 is insensitive to cell polarization, signifying that eqn 6.1 dominates surface chemistry. This observation also implies that most of the observable carbon is not localized near the electrochemically

active Ni-YSZ three-phase boundary. This result is consistent with the observation that polarizing the cell to 75% I_{max} leads to additional cooling of only 1–2 °C. In contrast, thermal imaging and Raman spectra together provide strong evidence that exposure of Ni anodes to biogas promotes dry reforming and reverse Boudouard chemistry. Both eqn 6.2 and the reverse of eqn 6.3 predict substantial cooling and a lack of observable carbon deposition.

FTIRES data also strongly support two different fuel utilization mechanisms. Unless the SOFC is polarized, exposure to CH_4 creates only very small amounts of observed CO_x species in the gas phase and no measurable $CO_{2(ads)}$. Polarizing the cell creates a measurable amount of $CO_{2(ads)}$ that is assigned as an electrochemically produced intermediate. Gas-phase CO produced by polarized cells operating with CH_4 is a product of incomplete fuel oxidation or a secondary reforming reaction. FTIRES spectra from cells exposed to biogas show substantial reforming as evidenced by less observed CH_4 and relatively high, steady-state concentrations of both gas-phase (CO) and surface ($CO_{2(ads)}$) incomplete oxidation products. Reforming reactions lead to less deposited carbon both during exposure and during subsequent electrochemical oxidation after the biogas has been purged from the anode atmosphere.

Conclusions

Optical data presented in this work have led to the development of a detailed, experimentally validated understanding of the chemistry occurring on the anode surface of SOFCs operating with both dry CH_4 and a simulated biogas mixture. Data acquired with three independent techniques show that nickel is a much more active catalyst for

biogas than for CH_4. Despite the substantial reactivity inferred from thermal images of Ni-YSZ cermet anodes exposed to biogas, this fuel is quite clean. Raman spectra acquired in operando show no detectable carbon formed on polarized and unpolarized SOFC anodes, and FTIRES spectra from polarized cells show measurably less CO_x being emitted from anodes exposed to biogas compared to CH_4. Because carbon growth has been well-implicated as deleterious to SOFC operation, these results point to the advantages associated with the naturally-occurring reforming in biogas– SOFC systems.

Questions remain about reactions occurring within the active region of the anode, but findings from in situ thermal imaging, vibrational Raman spectroscopy, and FTIRES inspire confidence that these techniques used in combination with novel anode designs and/or electrolyte supported assemblies will continue to uncover chemical mechanisms responsible for electrocatalytic oxidation in high temperature SOFCs. Coupled in operando optical studies are underway currently to test these ideas. Finally, further investigations are planned to test the impacts of other trace biogas constituents under SOFC operation, including hydrogen sulphides and aromatics.

CHAPTER 7

TOWARDS A WORKING MECHANISM OF FUEL OXIDATION IN SOFCS: IN SITU OPTICAL STUDIES OF SIMULATED BIOGAS AND METHANE

Contribution of Authors and Co-Authors

Manuscript in Chapter 7

Author: John D. Kirtley

Contributions: Contributed to most experiments in this work and led some, analyzed most data, wrote first draft and contributed to subsequent editions.

Co-Author: Dr. Michael B. Pomfret (Naval Research Laboratory)

Contributions: Led and designed many of the experiments, analyzed some data, and assisted in manuscript revisions.

Co-Author: Dr. Daniel A. Steinhurst (Nova Research, Inc.)

Contributions: Assisted in many experiments, assisted in data collection and processing, contributed to manuscript revisions.

Co-Author: Dr. Jeffrey C. Owrutsky (Naval Research Laboratory)

Contributions: Provided helpful assistance through discussions and experimental advice, assisted in manuscript revisions.

Co-Author: Dr. Robert A. Walker

Contributions: Provided helpful assistance through discussions and experimental advice, assisted in manuscript revisions.

Manuscript Information Page

John D. Kirtley, Daniel A. Steinhurst, Jeffrey C. Owrutsky, Michael B. Pomfret and Robert A. Walker
Journal of Physical Chemistry C
Status of Manuscript:
____ Prepared for submission to a peer-reviewed journal
__x__ Officially submitted to a peer-review journal
____ Accepted by a peer-reviewed journal
_____ Published in a peer-reviewed journal

Publication anticipated by the American Chemical Society
Submitted November 12, 2014

Introduction

As renewable energy generation increases globally, a need for developing technologies that provide stable electricity independent of seasonal and diurnal fluctuations has also grown.[6, 167] Solid oxide fuel cells (SOFCs) promise versatility in meeting this challenge by cleanly and efficiently producing electricity from bio-renewables. Fuels from biomass feed stocks are already being utilized for combustive applications within the transportation and stationary power sectors.[6, 167] Biogas in particular is a simple, easily derived fuel that is often "upgraded" to eliminate carbon dioxide and other, minor, constituents to create bio-methane; this mixture in turn can be fed into a natural gas grid or used as a fuel in the transportation sector.[6, 8, 168] However, these applications suffer from low efficiencies that are inherent to combustive energy conversion. On the other hand, SOFCs in combined heating and power systems can achieve efficiencies above 70%,[10, 12] and can cleanly produce electricity from biogas without the need for carbon dioxide removal.[146]

Biogas is particularly well suited for use in traditional, Ni-based SOFCs because the naturally occurring carbon dioxide helps mitigate deleterious carbon formation on anode Ni surfaces through internal reforming processes.[32, 54, 146] Methane composition in biogas can vary from 45-70% depending on the fuel source,[32, 168] and is balanced primarily by carbon dioxide. In addition, methane compositions near 50% have been shown to lead to optimal electrical power and stable operation (> 600 hours) in SOFCs[36] perhaps because carbon accumulation was less pervasive.[36, 54]

The performance and longevity of SOFCs can vary dramatically not only as a function of biogas fuel composition, but also according to temperature and anode composition.[36, 54, 146, 169] Understanding these relationships in terms of detailed, predictive mechanisms is critically important to developing optimal device design and operational protocols. Van Herle et al. modeled electrical and combined thermal efficiencies from a demonstration SOFC system at a farm biogas production site,[34] and Wongchanapai et al. performed a similar study;[37] both reports, however, stopped short of a mechanistic description predicting performance. Other studies have also provided qualitative and even quantitative insights into biogas fuel chemistry occurring on SOFC anode surfaces or in related, simpler systems through experimental observation; some studies have also included a modelling component. These studies utilized techniques such as temperature programmed oxidation (TPO),[54] thermogravimetric analysis (TGA),[132] gas chromatography,[56] mass spectrometry,[54, 57, 170] electrochemical characterization,[58, 160] and scanning electron microscopy (SEM)[54] to assess observables such as exhaust composition, anode composition and microstructure, and electrochemical performance. For example, Lanzini et al. reported on the quantity and structure of carbon deposits in SOFCs operating with different simulated biogas compositions, and also described fuel chemistry associated with electrochemical performance.[54] A thorough study by Wei and Iglesia utilized isotopically-labeled reactants to determine that the kinetics for dry reforming of methane is mediated by C-H bond activation and reaction of adsorbed oxygen with adsorbed carbon.[56] However, each of these studies lacked the direct,

molecularly specific *in operando* observations needed to identify the mechanisms responsible for the electrochemical oxidation of biogas in SOFCs.

The production of oxides at the cathode and transport of these oxides through the solid, ceramic electrolyte involve high activation energies that require SOFCs to operate at high temperatures (650 °C – 800 °C). While these temperatures also allow SOFCs to operate with a large collection of compatible fuels – a distinct advantage over other, lower temperature fuel cells,[10] this requirement presents challenges in designing experiments and techniques that probe electrode chemistry directly. Consequently, studies and techniques capable of providing direct observations of species present during SOFC operation are few, especially with regards to biogas fuels or their constituents. Yu et al. have used "ambient" pressure X-ray photoelectron spectroscopy to examine the mechanisms responsible for high temperature CO_2 electrolysis on Ce-based devices with research-level power outputs.[171] Near-infrared (NIR) thermal imaging was first used to monitor temperature changes *in operando* across an anode surface of a functional SOFC by Pomfret, *et al*[62]. and the method has been used in similar studies by others.[75, 76] Pomfret, Owrutsky, and Walker[60] first utilized vibrational Raman spectroscopy to directly monitor SOFC anode surface changes during SOFC operation, and demonstrated that this technique is especially sensitive to carbon formation. The technique has been employed by others to study gadolinium-doped ceria as an inhibitor to carbon formation,[73] the potential application of *in situ* surface-enhanced Raman to SOFCs,[172] and carbon accumulation across an anode surface.[74] Most recently, Fourier transform

emission spectroscopy (FTIRES) has been used by Pomfret et al.[77] to monitor gas phase and adsorbed species directly in real time over an operational anode surface.

Recently, Kirtley et al. utilized a combination of these optical methods (NIR thermal imaging, vibrational Raman spectroscopy, and FTIRES), coupled with electrochemical measurements, to examine electrochemical processes on a Ni-based anode in a SOFC operating with simulated biogas at 800 °C.[145] This work demonstrated that the combination of these techniques provide data capable of distinguishing between mechanisms responsible for fuel oxidation and carbon accumulation as a function of fuel type. In particular, exposing the SOFC anode to the biogas surrogate resulted in substantial anode cooling (ΔT = -13 ^{o}C) but minimal carbon accumulation. This result is consistent with the recognized endothermic dry reforming of methane,[75, 173] but appears to contrast with earlier work that associated cooling from larger hydrocarbon fuels to carbon formation.[93, 159] Catalytic decomposition of methane (in the absence of CO_2) to form carbon is less endothermic than the dry reforming processes that occur with biogas, and cooling was also measurably less (ΔT = -3 °C). Both Raman spectroscopy and FTIRES measurements indicated that more carbon was formed from operating on methane relative to the biogas surrogate. These data illustrated how different, proposed chemical processes may be responsible for these phenomena.

This current study seeks to expand upon these findings by exploring how different processes such as the catalytic decomposition of methane, dry reforming, water-gas shift reactions and Boudouard chemistry vary as a function of operational temperature, fuel, and electrochemical load, in an operational SOFC. Electrochemical and direct optical

observations provide a self-consistent, mechanistic picture that describes, in particular, why carbon formation is more extensive under methane fuel at 800 °C relative to 700 °C, and why the reverse is true for simulated biogas. This work also details how carbon formation is much more pervasive under methane fuel and explores reasons for possible structural differences between carbon formed under methane, relative to simulated biogas.

Experimental

SOFC Sample Preparation and Test Assembly

Anode-supported SOFCs (or membrane electrode assembly) were purchased from Materials and Systems Research, Inc. (MSRI) and are composed of a Ni/yttrium stabilized zirconia (YSZ) anode support (~800 μm), Ni/YSZ functional layer (12-25 μm), YSZ electrolyte (8-10 μm), and lanthanum strontium manganate (LSM)/YSZ cathode functional layer (15 μm), and 50 μm thick LSM/YSZ cathode. Fabrication and characterization methods of similar cells can be found elsewhere.[158] Gold and platinum current collectors were attached to the anode and cathode, respectively, in a procedure similar to that described previously.[145, 159] Each SOFC is about 25.4 mm diameter and pasted onto an alumina tube (Sentro Tech) of similar diameter using alumina paste (Aremco). An alumina fuel tube is attached to the assembly, with a flute attached at the anode end to direct flow fuel across the anode. Two test assemblies were used, each optimized to transmit visible and infrared light in the Raman and NIR thermal imaging/FTIRES experiments, respectively. Full details of each assembly, as well as other construction details, can be found in previous publications.[52, 145, 159]

Electrochemical Measurements

Electrochemical characterization and control was performed by a Princeton Applied Research VersaStat MC or by a Gamry Reference 3000 Potentiostat/Galvanostat/ZRA. Linear Sweep Voltammetry (LSV) was performed under methane or simulated biogas fuels and before each trial under benchmark hydrogen fuel flows (detailed below) to assess cell performance. In an LSV measurement, current was measured while potential was varied at 0.1 *V*/s, beginning near open circuit voltage (OCV) and ending near 0 *V*, which is typically the maximum current (I_{max}) (under biogas or methane, this value averaged near 425 *mA*). Power (in *mW*) was computed by multiplying *I,V* ordered pairs; P_{max} is the maximal power calculated near the midpoint of the *I,V* trace (Figure 7.1). Chronopotentiometric and OCV measurements monitored cell voltage under a constant current load (ranging from 25-75% I_{max}) and under zero current load, respectively, during fuel flow. Chronopotentiometric measurements were also used to subsequently electrochemically oxidize any deposited carbon following fuel flow. Further details may be found in a previous publication.[145]

Vibrational Raman Spectroscopic Measurements

Raman spectra were acquired *in operando* by directing a 488 nm Ar-ion laser beam (~24 mW) through a custom optical assembly and focusing with a 10x long-working distance objective onto an SOFC anode surface with spot diameter of ~2 μm; the sample region was usually chosen about half way between a central current collector and the MEA edge at the fuel inlet. Stokes backscatter was passed through an edge filter and diffracted onto a CCD detector. Further details of the custom Raman measurement

assembly may be found in earlier publications.[60, 145] Raman spectra reported here were acquired *in operando* over a range of 100-3200 cm^{-1} with 10 sec acquisitions and 2 or 3 accumulations.

Fourier Transform Infrared Emission
Spectroscopic (FTIRES) Measurements

Infrared light emitting from hot gas phase species over the anode, the anode surface itself, and furnace assembly was passed through two sapphire windows and onto the detector of an infrared spectrometer (Mattson Instruments, Inc., Model #: RS-10000, adapted by removing the internal emission source).[77, 145] The furnace cavity and spectrometer was vigorously purged with argon and/or nitrogen to remove ambient CO_2 (residual CO_2 was ~1 ppm or less). Each FTIR spectrum was collected from 500 cm^{-1} to 5000 cm^{-1} with 0.5 cm^{-1} resolution and 16 accumulations. We note that in the spectral range below 1800 cm^{-1}, the sapphire windows attenuate and interfere with any emitted light. Spectra were acquired in 200 s intervals during each experimental sequence (fuel flow, a subsequent purge and electrochemical cleaning-detailed below). Prior to each sequence, a single beam spectrum was collected as a background reference and subtracted from each subsequent spectrum. Additional processing was implemented to further correct for a non-zero baseline and absorbance from a small amount of room temperature, ambient CO_2, as detailed previously.[145] This correction most strongly influenced the $CO_{2(g)}$ region, with minimal influence upon $CO_{2(ads)}$ and none upon $CO_{(g)}$.

Near Infrared (NIR) Thermal Imaging

High resolution near infrared images from most or the entire anode surface emitting infrared radiation were captured by a CCD camera (AVT, Stingray F033B ASG) and 18-108 mm focal length zoom lens (Navitar Zoom 7000).[62, 145, 159] A long pass filter was placed over the lens to block visible light below 720 nm. Images were collected with LabView v8.5 simultaneously with electrochemical measurements and under different fuel flows (see experimental procedure section). Temporal resolution was > 4 Hz, with ~100 μm spatial resolution. Emission intensity was calibrated with temperature using a thermocouple near the anode, and post-experiment processing that converted intensity to temperature was accomplished using in house software. Typical temperature resolution was ~0.1 °C.

Experimental Procedure

A particular experiment consisted of multiple trials with a single membrane electrode assembly (MEA). Experiments were performed at least in duplicate under a particular combination of optical measurement(s), temperature, and fuel. Observations did vary from run to run, but were generally reproducible, and where possible, results were normalized and averaged to better represent trends. In general, 5 trials were performed with each MEA to vary electrochemical loading during fuel exposure. Each MEA, held under an Ar gas flow at the anode and air (or 20 mL/min O_2/65 mL/min Ar) at the cathode, was heated at ≤ 1°C/min to nominal operational temperature nears 700 °C, 750 °C, or 800 °C. The actual anode surface temperature generally varied by ≤ ±10 °C

from the target temperature under hydrogen fuel. At temperature, the Ni/YSZ anode was reduced with H_2 and Ar until a stable OCV reading was reached.

One trial consisted of a general sequence detailed in a previous publication.[145] Each trial consisted of a ~10 minute fuel exposure (either biogas or methane, diluted with Ar) to the MEA at varying polarizations (OCV- 75% I_{max}, relative to that particular fuel), a purge under hydrogen fuel (diluted with Ar), and a polarization at 0.67% I_{max} (relative to hydrogen fuel, for data reported here). This polarization step served to electrochemically "clean" any carbon deposits. Optical data were collected, in general, throughout the entire trial.

Together, these measurements provided insight into phenomena such as surface temperature changes, surface carbon formation, bulk carbon formation, surface intermediates, gas phase species, and electrochemical performance--all originating from electrochemical and catalytic processes occurring on an anode surface. These results were complementary and pointed to a self-consistent description of these chemical processes.

Results

SOFC Electrochemical Benchmarks

The electrochemical performance of an SOFC was tested with LSV throughout each experiment on a single MEA, and also during methane or simulated biogas fuel flows. Single measurements collected under biogas at three temperatures are shown in Figure 1a. Measurements under specific operational conditions (temperature and fuel) demonstrated some variability, so diagnostics such as OCV, P_{max}, and I_{max} from individual runs should be compared cautiously. However, the averages and standard

deviations of these values are insightful. Figure 7.1b shows clearly that the OCV observed under hydrogen did not systematically vary with temperature, though OCV is expected to increase with operational temperature.[174] The average OCV from simulated biogas increased 60 mV over 100 °C, whereas under methane this value changed less with temperature and was within experimental uncertainty. Figure 1b also shows a clear separation of OCV between the two fuels at all temperatures. Neither P_{max} nor I_{max} indicated a temperature or fuel dependence, and calculations relating current at P_{max} to fuel efficiency indicated that SOFCs operated at 800 °C with methane and simulated biogas demonstrated similar values.[174]

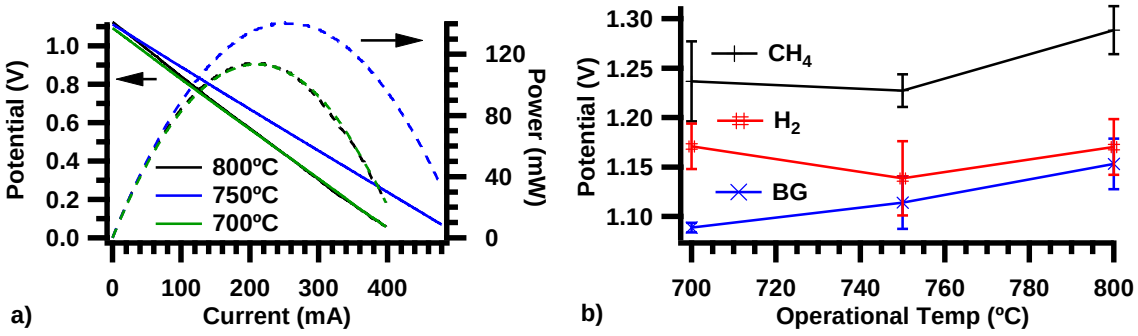

Figure 7.1. Representative Linear Sweep Voltametry (LSV) traces collected during simulated biogas fuel flow at 800°C, 750°C, and 700°C. Solid V-I and dashed P-I traces are assigned to the left and right axis, respectively (a). A more complete representation of averaged open circuit voltages (OCVs) with error bars (experimental variation) are shown in (b) for CH_4, simulated biogas (BG) and H_2 as a reference.

Raman Spectroscopy During Fuel Exposure

Raman spectra collected from the Ni/YSZ anode surface during methane and biogas fuel exposure provide a clear description of carbon formation as a function of fuel and temperature on the anode surface, particularly within the first 1 μm below the

surface. From Figure 7.2a, Raman spectra acquired at OCV most prominently show differences between an anode surface exposed to methane fuel and one exposed to simulated biogas fuel. At all temperatures, SOFC anodes exposed to methane fuel showed evidence of carbon accumulation as indicated by the D (1341 cm^{-1}), G (1558 cm^{-1}), and 2D (2696 cm^{-1}) features.[69, 71] The strong G and 2D features indicate an ordered graphitic structure, but the presence of the D feature (strongest at 700 °C) also indicates site defects and grain boundaries within the graphite network.[70, 75] Simulated biogas exposure did not result in spectroscopically-observable carbon at 800 °C, and only intermittently at lower temperatures. In those instances where carbon was observed, additional trials completed under current load did not indicate that Raman carbon signatures systematically decreased with polarization, as might be expected.[93] This result was surprising, and points to the possibility that carbon accumulation may vary across an anode cross section, especially when the SOFC is polarized.[73]

These results indicate that simulated biogas was associated with much less carbon accumulation on the anode surface relative to methane. Related work by Lanzini et al demonstrated that carbon formed on (unpolarized) Ni/YSZ anode supports exposed to methane near 800 °C for ~2 hours.[54] An equivalent amount of methane mixed with the same amount of carbon dioxide also resulted in carbon filament growth, though to a lesser extent. Indeed, for catalysts of equivalent mass, their study indicated that the total amount of carbon formed from methane being 30-fold greater than that formed from the biogas mixture.

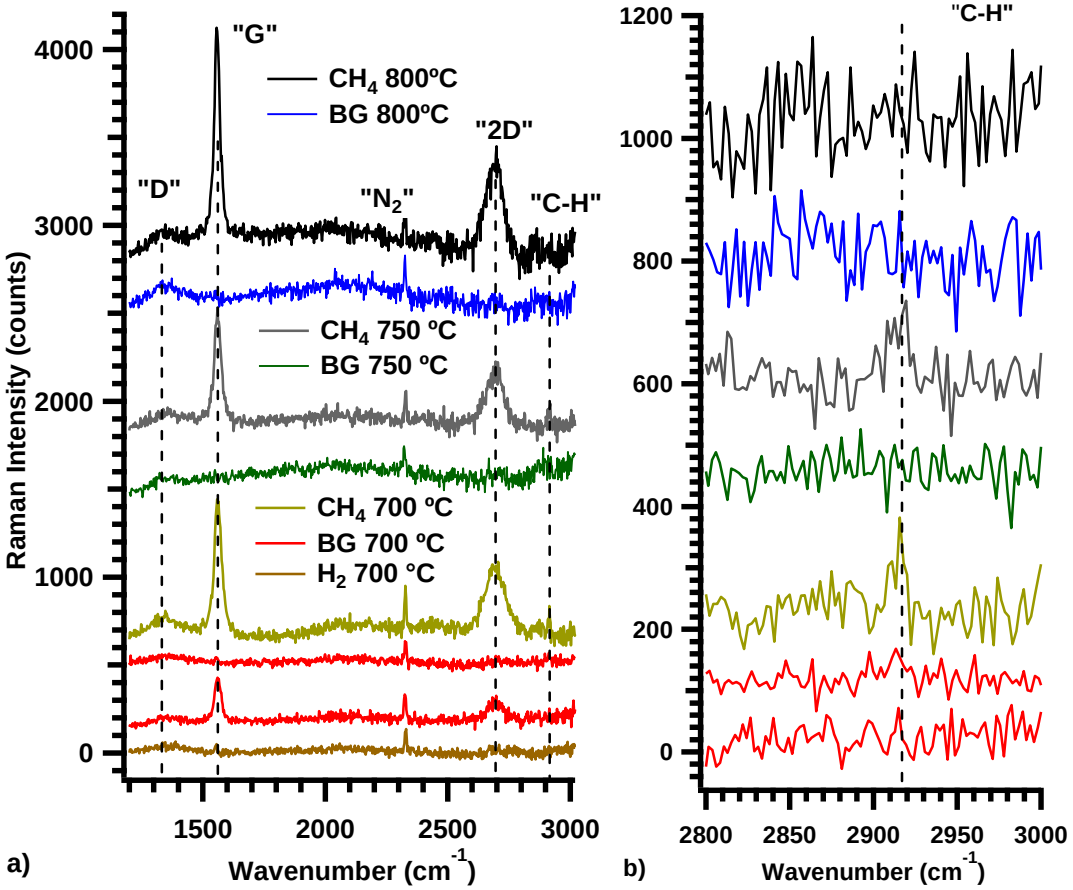

Figure 7.2. Survey of Raman vibrational carbon signatures present on an MEA anode surface during methane, simulated biogas fuel, and hydrogen (for reference) exposure at OCV and ~700 °C – 800 °C. All traces represent 2 or 3 accumulations, and have been corrected to provide a linear baseline; most have been offset vertically for clarity (a). A more detailed representation of a $-CH_x$ signature is shown in (b). There are two traces for biogas at 700 °C to show the variability in carbon accumulation with biogas at this temperature.

In operando vibrational Raman spectra also indicate an additional, weak feature at 2920 cm^{-1} from spectra of SOFC anodes exposed to methane (Figure 7.2b). This feature was readily apparent under methane fuel at 700 °C and 750 °C, but it did not appear consistently under simulated biogas. Because this peak was always observed when methane was present in the fuel stream, was independent of a graphite signature, and was

influenced by CO_2 in the fuel stream (that only reacts with methane heterogeneously[146]), a plausible assignment is a Ni surface-adsorbed CH_x stretching mode, most likely either Ni-CH or Ni-CH_2.[72] We note that this assignment marks the first ever report of a –CH vibrational feature in functioning SOFCs and suggests that careful selection of fuel conditions and cell polarization may be able to isolate specific intermediates formed during electrochemical oxidation of hydrocarbons in SOFCs.

FTIRES Measurements During Fuel Exposure

During fuel exposure, infrared radiation emitted from hot gas species was monitored by FTIRES to identify and quantify gas and surface species over the anode surface. The same species were observed in the headspace with both methane and biogas SOFC operation but with different mole fractions. Figure 7.3 shows emission spectra from anodes at 700 ˚C that include signatures from $CH_{4(g)}$ (3007 cm^{-1} band center), $CO_{2(g)}$ (2350 cm^{-1}), and $CO_{(g)}$ (2144 cm^{-1}).[77] As expected and as observed at the higher temperature,[145] the ratio of $CH_{4(g)}$:$CO_{2(g)}$ was higher under methane flows relative to biogas.

Figure 7.3 reveals a fourth feature near 2290 cm^{-1} that is present in both spectra. This feature has been attributed to a steady-state population of CO_2 physisorbed ($CO_{2(ads)}$) to the Ni surface as a reaction intermediate.[77] This assignment is plausible because dry reforming of methane and electrochemical oxidation of carbon must each occur on the Ni surface, leading to adsorption of CO_2 reactants or desorption of CO_2 products, respectively.

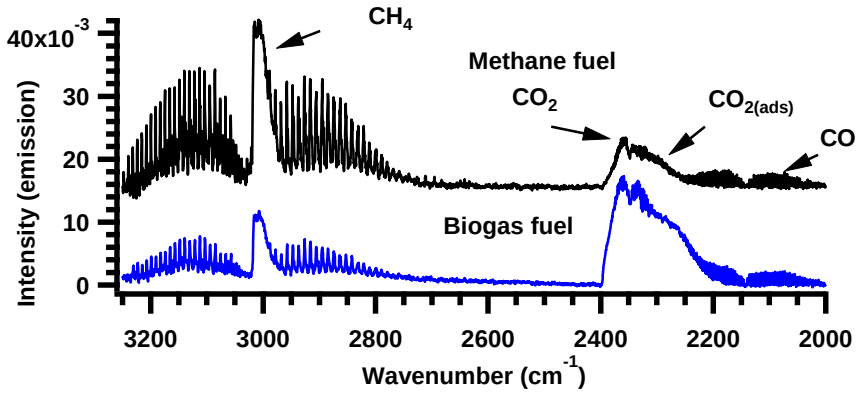

Figure 7.3. Survey of signatures from gas phase and physisorbed species observed with FTIRES from a Ni/YSZ SOFC anode collected during methane and biogas fuel flow at 700 °C and OCV. The baseline has been zeroed and corrected to account for absorbance from trace amounts of room temperature, ambient CO_2 in the spectrometer.

The relative concentrations of $CO_{2(ads)}$ and $CO_{(g)}$ were characterized under different cell operating conditions to gain insight into the underlying chemical mechanisms. Data in Figure 7.4a-f show how $CO_{2(ads)}$ (measured at 2290 cm^{-1}) and $CO_{(g)}$ (measured at the v_1 , *J(11)* → v_0 , *J(12)* rovibrational transition, 2094 cm^{-1}) varied as a function of electrochemical potential. Values were normalized to a common point (100 s) for each trial to account for system-dependent variations between experiments, and averaged over duplicate experiments. These data show that when the cell was polarized with methane fuel, $CO_{2(ads)}$ and $CO_{(g)}$ intensities increased relative to similar trials at OCV. Interestingly, at 700 °C, the $CO_{(g)}$ emission intensity experienced less polarization dependence relative to $CO_{2(ads)}$. At 800 °C, $CO_{(g)}$ experienced more polarization dependence. Though experimental uncertainties are large, this result may reflect a Boudouard equilibrium (Reaction 7.1) or water-gas shift equilibrium that predicts at high temperatures, electrochemically-produced CO_x products should favor $CO_{(g)}$ over

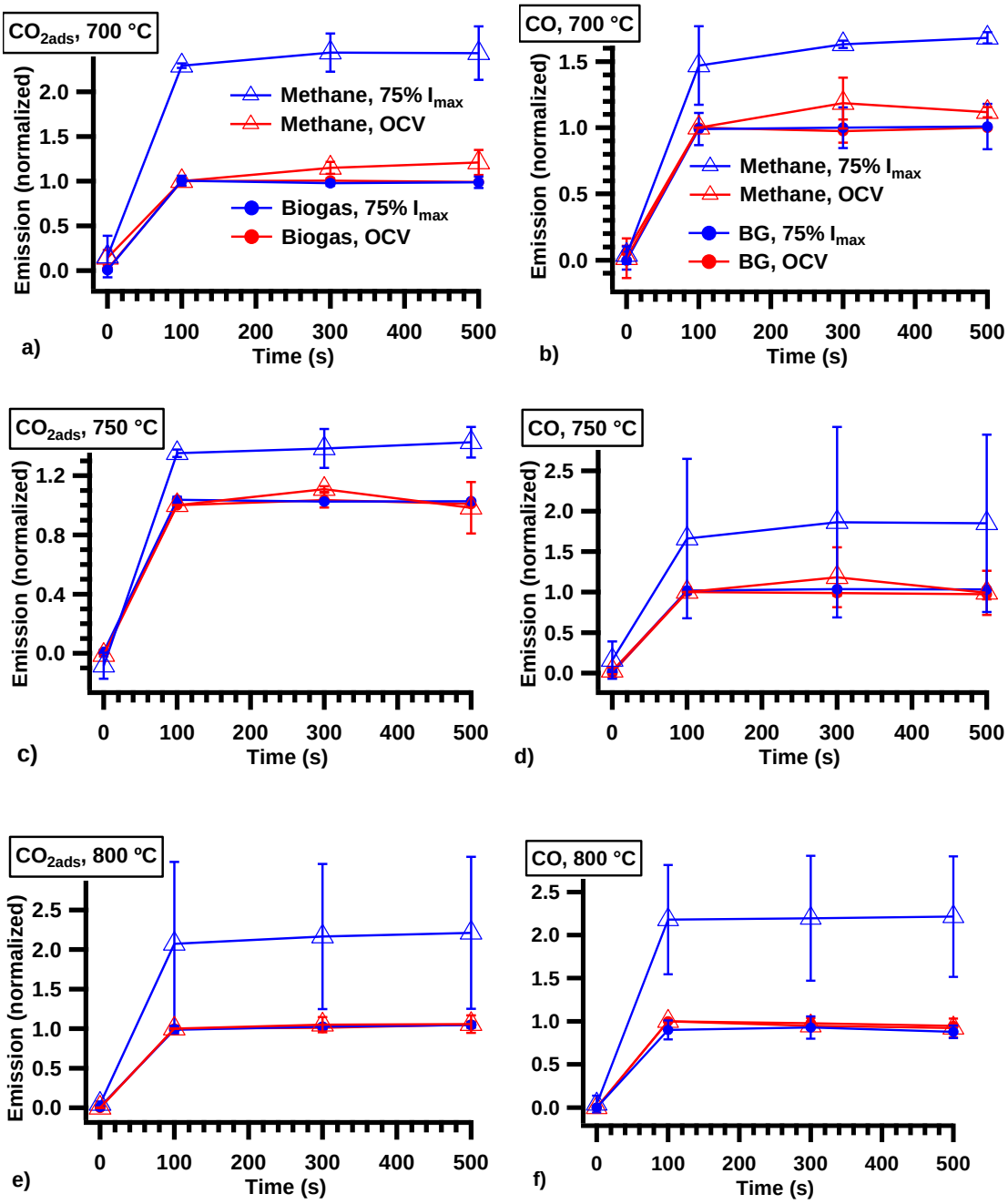

Figure 7.4. Comparison of $CO_{2(ads)}$ (a, c, e) and CO (b, d, f) species observed *in situ* during SOFC operation with simulated biogas (circles) and methane fuel flow (triangles) at 700 °C (a-b), 750 °C (c-d), and 800 °C (e-f) at OCV (red) and 75 % I_{max} (blue). Intensities from a particular experiment were normalized to the 100 s mark taken during exposure at OCV. Data points indicate averages from duplicate experiments, and error bars indicate uncertainties.

$CO_{2(g)}$.[175, 176] Under biogas fuel this polarization dependence was not observed at any temperature.

NIR Thermal Imaging

Measurements During Fuel Exposure

Endothermic and exothermic catalytic reactions on the anode affect its surface temperature and consequently the spectral profile of the emitted near infrared light. Changes in the anode's emissivity due to processes such as carbon growth can also contribute to apparent temperature changes. Differentiating between changes in temperature and emissivity has been discussed previously.[159] For the biogas studies described in this work, changes in emissivity were found to have minimal influence on the reported results. Data in Figure 7.5 show the temperature change that occurred relative to an initial hydrogen fuel flow (0 sec) following the introduction of methane or simulated biogas for cells at OCV. These temperature changes reflected surface chemistry and were, in general, largely reversible at the end of each trial. Several observations stand out: 1) exposing the anode at OCV to simulated biogas resulted in significantly more cooling (ΔT of -4.5 °C to -11 °C) than was observed when operating on methane (ΔT of -1 °C to -2 °C), and 2) the cooling (ΔT) with biogas increased sharply, and non-linearly, with the anode's surface temperature. Under biogas, cooling was most pronounced near the fuel entrance, as documented in earlier work.[145] Temperature measurements are reported from this region. Polarizing SOFCs under biogas and methane led to a small, additional amount of cooling relative to operation under OCV (Appendix D). Furthermore, at 800 °C, this electrochemically-induced cooling under methane was greater relative to biogas.

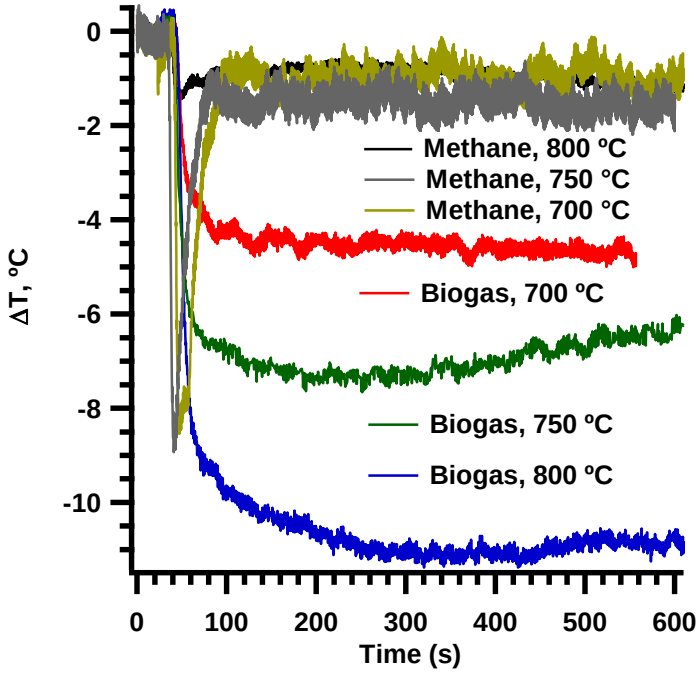

Figure 7.5. Comparison of anode temperature losses (ΔT) during methane and simulated biogas exposure at OCV and at 700 °C, 750 °C, and 800 °C.

FTIRES during Chronopotentiometry

In addition to using Raman spectroscopy to directly monitor the carbon, we used chronopotentiometry and FTIRES to indirectly quantify how much carbon had been deposited during SOFC operation with methane and biogas under different operating conditions. This technique has been used previously to directly correlate, in real time, chronopotentiometric data with Raman spectra to quantify carbon formation and detail electrochemical mechanisms during its removal.[118, 137] The present study demonstrates that combining chronopotentiometric measurements with FTIR emission spectra can also provide detailed and quantitative insight into carbon accumulation within the Ni cermet anode and the effects of carbon accumulation on electrochemical performance. In these measurements an electrochemical polarization was applied to the SOFC exposed to an Ar

flow to maintain a constant current (67% of I_{max}). Under these conditions, the only 'fuel' present was the solid carbon that had already accumulated within the anode microstructure. The initial electrochemical potential required to maintain a constant current led to a value more positive relative to OCV, and continued polarization required that the potential rise to maintain a constant current as electrochemically-accessible carbon was oxidized to form CO_2 and CO (Figure 7.6a,b). This increasing potential reflected the oxidation of a diminishing reserve of any carbon in the Ni/YSZ matrix, and finally, the anode Ni itself. Previous work has described a cell potential that rises sharply before reaching a relatively flat region is generally attributed to a 'Nernst equivalence point' signifying the removal of electrochemically accessible carbon.[118, 137] Of the three optical measurements collected, here we report only FTIRES results that show $CO_{2(ads)}$ produced during the course of the electrochemical oxidation (e.g. Figure 7.6c, d).

The combination of chronopotentiometric measurements with simultaneous measurements of CO_x species demonstrated that the amount of carbon deposited by biogas varied as a function of temperature and cell polarization during operation. The *t-V* traces in Figures 7.6a and 7.6b indicate clearly that the cell potential's rise through the equivalence point *after* exposure to simulated biogas depended sensitively on the electrochemical load *during* fuel exposure. Furthermore, in Figures 7.6c and 7.6d, the intensity of the $CO_{2(ads)}$ emission band decreased more rapidly in a manner that correlates closely with cell potential. Similar trends were observed with $CO_{(g)}$. These two observations confirm first that carbon *did* form in the electrochemically active region of

the anode and second, that less carbon was electrochemically oxidized following exposure to simulated biogas with the anode under polarization.

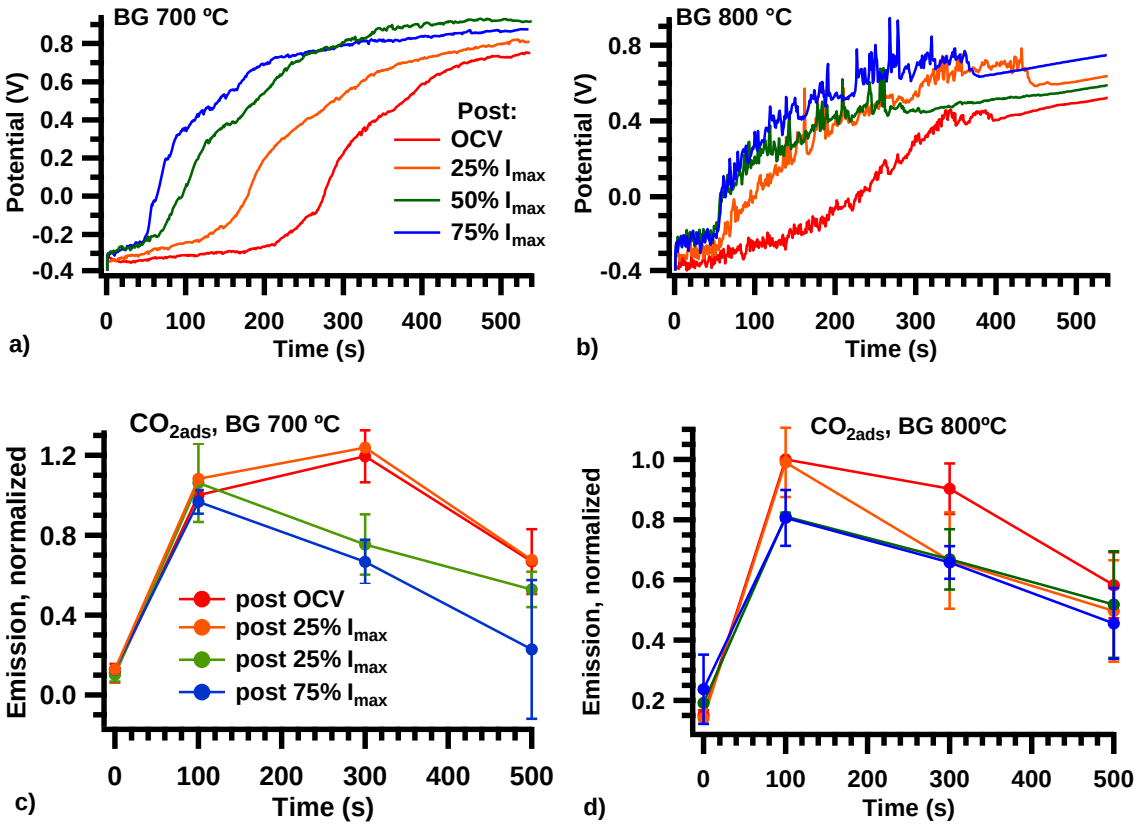

Figure 7.6. Chronopotentiometric removal of anode carbon deposits at a current of ~67% I_{max}, *following* exposure to simulated biogas fuel at 700 °C (a) and 800 °C (b) and 0-75% I_{max}. FTIRES measurements simultaneously monitored $CO_{2(ads)}$ signals *in operando* during these and duplicate measurements taken after fuel exposure at 700 °C (c) and 800 °C (d) and 0-75% I_{max}. Emission intensities from a particular experiment were normalized to the 100 s mark taken during "cleaning" after fuel exposure at OCV. All trials were repeated at with different MEAs and the reported data show averages from the ensemble of measurements. Error bars show experimental range of data.

Finally, Figure 7.6 indicates that more carbon was electrochemically oxidized at 700 °C than at 800 °C. This result is most easily seen by comparing normalized intensities along the x-axis in Figures 7.7c and 7.7d, especially at 300 s. Furthermore, an

electrochemical equivalence point was reached on average at 350 s and 260 s at 700 °C and 800 °C, respectively, from experiments conducted with the Gamry Reference potentiostat. Similar measurements completed at 750 °C showed behavior intermediate between the 700˚C and 800˚C experiments.

In contrast with the anode behavior under biogas, the electrochemically-accessible carbon deposited during methane exposure did not depend upon the applied current load (Figure 7.7). This result is surprising, especially when recalling that CO_x signatures *did depend* upon the current load during methane fuel flow (Figure 7.4). Contrasting with biogas experiments, less carbon was electrochemically oxidized following methane exposure at 700 °C relative to 800 °C. (Average electrochemical equivalence points from experiments conducted with the Gamry Reference potentiostat were 300 s and > 480 s, respectively.) Furthermore, at 800 °C significantly more carbon was electrochemically removed after methane exposure, relative to simulated biogas exposure (Figure 7.7).

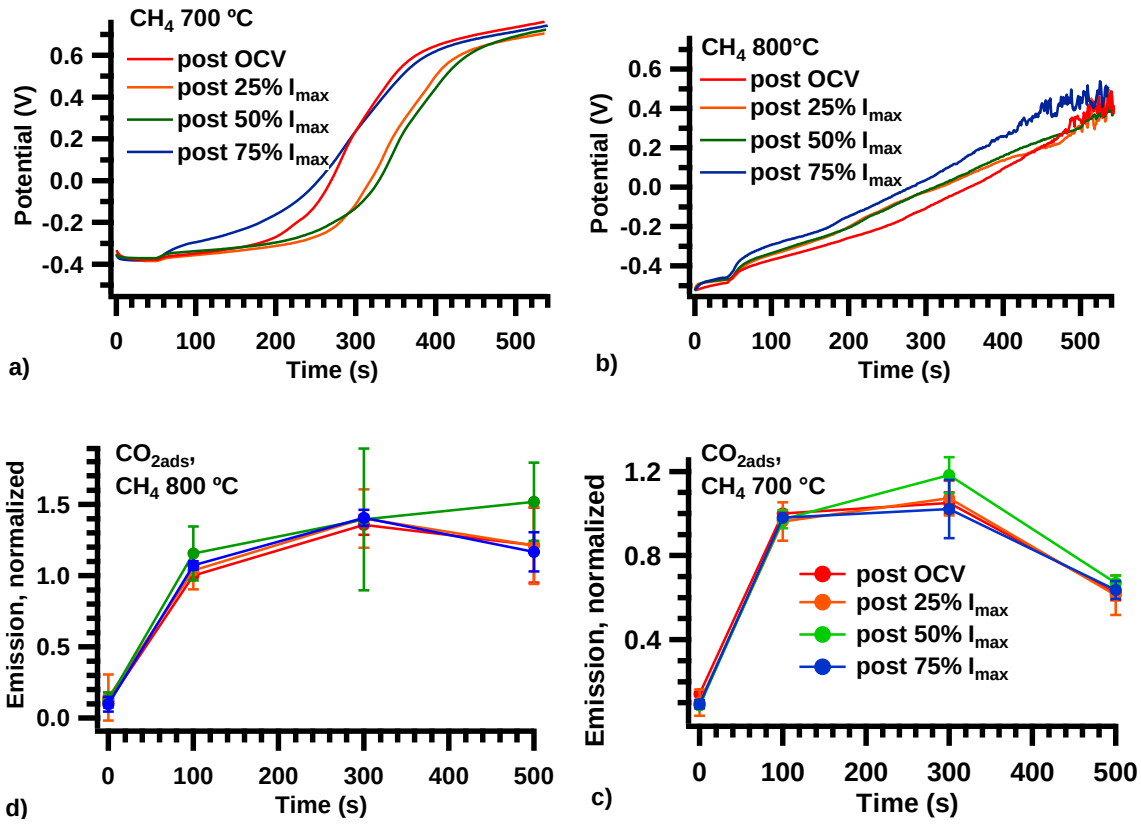

Figure 7.7. Chronopotentiometric removal of anode carbon deposits at a current of ~67% I_{max}, *following* exposure to methane fuel at 700 °C (a) and 800 °C (b) and 0-75% I_{max}. FTIRES measurements simultaneously monitored $CO_{2(ads)}$ signals *in operando* during these and duplicate measurements taken after fuel exposure at 700 °C (c) and 800 °C (d) and 0-75% I_{max}. Emission intensities from a particular experiment were normalized to the 100 s mark taken during "cleaning" after fuel exposure at OCV. All trials were represented in duplicate; data points indicate averages and error bars indicate standard deviations.

Discussion

We discuss two considerations important to SOFC operation with a biogas surrogate relative to methane: first, the origins of deleterious carbon accumulation and, second, heterogeneous mechanisms responsible for electrocatalysis that vary according to fuel composition, operational temperature, and electrochemical polarization. We note

that, unlike with higher molecular weight, carbon containing fuels, gas phase chemistry with both methane and biogas is not expected, largely because methane is difficult to activate without a catalyst.[57, 146, 177] For this reason some of the tendencies of methane and biogas differ from those observed from SOFCs operated with higher molecular weight hydrocarbons and alcohols.[62, 93, 159, 161]

Some modeling and experimental studies have provided a basis for evaluating the heterogeneous reactions responsible both for carbon accumulation and for reforming pathways within a Ni-based SOFC anode. Lanzini et al.[54] determined that carbon growth under CH_4 was ~ 30 times greater than with a 1:1 CO_2:CH_4 fuel mixture, and showed that the CH_4 catalytic decomposition rate increased with temperature. Ginsburg et al.[178] modeled methane dry reforming over a nickel catalyst and attributed carbon formation to two mechanisms: the catalytic decomposition of methane and the Boudouard reaction that accounts for the influence of the water-gas shift equilibrium. Carbon formation was predicted to decrease with increasing temperature and with increasing CO_2:CH_4 ratios in this system. Girona et al.[58] modeled a similar dry reforming system and showed that gas species vary spatially across and within the anode, and that near the electrolyte/anode interface, CO and H_2 are the dominant species. Walker and coworkers similarly observed cooling from simulated biogas mixtures to preferentially occur near the anode's fuel inlet and attributed this behavior to the endothermic dry reforming reaction.[145] Anisotropic, chemistry-induced cooling has long been thought to be detrimental to cell performance.[75, 173]

Detailed, kinetic insights have proven more difficult to ascertain. Wei and Iglesia[56] observed that CH_4 conversion rates slowed with prolonged fuel exposure, but that *initial* rates were comparable to rates observed with CO_2 and H_2O co-reactants. Hecht et al.[57] arrived at a similar conclusion via modeling and experiments. Wei and Iglesia deduced that initial CH_4 reforming rates are mediated solely by C-H bond activation leading to complete dehydrogenation, but Wang et al. asserted that CHO is instead a key intermediate.[152] Deutschmann and coworkers[59] later described the importance of surface oxygen in mediating the reforming reaction.

Carbon Formation

Several *in operando* techniques utilized in the current study provide important perspective about carbon formation from methane and surrogate biogas. Raman data show that graphitic carbon growth on the anode surface is much more pervasive with methane fuel compared to simulated biogas, especially at the highest temperatures tested in this work (800 °C), and is consistent with the findings of Lanzini et al. However, since Raman spectroscopy is limited to studying only the surface species present in a functioning SOFC, other techniques are needed that probe carbon deposition in the electrochemically active region.

In operando chronopotentiometric and FTIRES measurements taken *after* fuel flow (Figures 7.6 and 7.7) indicate the relative amounts of carbon formed near the electrochemically active interface between the anode and electrolyte, about 800 μm below the anode surface. The carbon sampled in these measurements is different from that sampled by Raman spectroscopy given that the Raman laser penetration depth

restricts measurements to only < 50 nm below the anode surface (accounting for porosity).[73] When SOFCs consist of either electrolyte - or cathode - supported membrane electrode assemblies and the entire anode (~20 μm depth) is electrochemically active, top surface Raman data can be representative of processes occurring throughout the anode. With anode supported cells, however, the top anode surface will likely promote different chemistry than what occurs close to the electrolyte-electrode boundary. Chronopotentiometry and FTIRES imply that carbon is deposited during biogas exposure near the electrochemically active region at all temperatures but accumulates most heavily at the lowest temperature (700 °C). This result contrasts with Raman spectra which indicate intermittent carbon growth only on anodes exposed to biogas at 700 °C and no observable carbon growth at 800˚C. In contrast, in the case of MEAs run with methane, chronopotentiometry and FTIRES indicate that *less* electrochemically accessible carbon forms at 700 °C relative to 800 °C. This interesting result suggests that different processes leading to carbon accumulation accompany each fuel, and that the temperature dependence of these processes are also different.

Finally, these chronopotentiometric and FTIRES experiments indicate that carbon formation is also sensitive to the electrochemical load (polarization) *during* biogas fuel flow, but not *during* methane fuel flow. Once again, this difference is important, pointing to different processes responsible for carbon formation near the electrochemically active region, and implying that these processes proceed at different rates.

Electrochemical Mechanisms

In operando observations presented in this work show trends that help isolate mechanisms associated with carbon accumulation, carbon dry reforming, and how these processes are modulated by electrochemical control. In our system, these observations will be also influenced by heat flow, fluid dynamics, and mass transport over and through the anode. The influence of these parameters and how these might influence thermodynamic and kinetic contributions to the chemistry is not well resolved. However, measurements described above provide information that, when examined from the perspective of earlier studies, supports several proposed mechanisms.[54, 56-59, 145, 152, 178]

First, NIR thermal images of an operational anode surface show a substantial decrease in the surface temperature during simulated biogas flow but a much smaller temperature change during methane flow under all reaction conditions. This important result likely suggests different mechanisms (with differing reaction enthalpies) governing anode chemistry, though a difference in methane conversion rates may also contribute to these observations. Methane is known to endothermically decompose on nickel to produce hydrogen leaving behind carbon deposits:[54, 56]

7.1. $CH_{4(g)} \rightarrow C_{(s)} + 2H_{2(g)} \quad \Delta H_{r,800\,^{\circ}C} = 83$ kJ/mol[b]

However, the heterogeneous dry reforming reaction (2) is even more endothermic:[146]

7.2. $CH_{4(g)} + CO_{2(g)} \rightarrow 2CO_{(g)} + 2H_{2(g)} \quad \Delta H_{r,800\,^{\circ}C} = 260$ kJ/mol

The different observed cooling trends under methane and biogas surrogate are consistent with the enthalpies of reactions (1) and (2), respectively. The significant cooling near the fuel entrance at the anode suggests that reaction (2) is most rapid in this region.

[b] Reaction enthalpy for the graphitic form of carbon

The temperature-dependence indicated by NIR thermal images in the biogas system suggests that the Boudouard and water-gas shift (WGS) reactions also contribute. Lending additional support to this hypothesis is the observation that OCV increases with temperature under biogas, suggesting an anode gas composition that varies with temperature (Figure 7.1). The exothermic, forward Boudouard reaction may contribute to some of these observations. This reaction's equilibrium varies with temperature, with $C_{(s)}$ thermodynamically favored at temperatures below 727 °C:[179]

7.3. $2CO_{(g)} \rightarrow CO_{2(g)} + C_{(s)} \quad \Delta H_{r,800\,^{\circ}C} = -177$ kJ/mol

(Interestingly, at room temperature, the equilibrium constant for the standard state gas phase reaction 7.3 is near 1×10^{21}.) Though not directly contributing to carbon formation, the water-gas shift reaction is likely relevant, though its contribution(s) to the experimental observations is unclear.[178]

7.4. $CO_{(g)} + H_2O_{(g)} \rightarrow CO_{2(gas)} + H_{2(g)} \quad \Delta H_{r,800\,^{\circ}C} = -34$ kJ/mol

The WGS reaction on a catalyst surface has been shown to favor the forward direction as reaction temperature decreases.[175] However, post-fuel FTIRES/chronopotentiometry measurements indicate that carbon growth from biogas near the anode/electrolyte interface becomes more important as temperature decreases, an observation consistent with the equilibrium for reaction 7.3 shifting toward the right (more $CO_{2(g)}$ and $C_{(s)}$). This behavior contrasts with the temperature dependence of carbon growth from methane.

Reaction 7.3 can also influence electrochemical products when the SOFC is polarized. Although the uncertainties are large, Figure 7.4 indicates that electrochemical products favor $CO_{(g)}$ as operational temperature increases under methane fuel. Additional

electrochemically-induced cooling is also observed under methane at 800 °C (Appendix D), consistent with the endothermicity of reverse Boudouard chemistry. Neither phenomenon shows a polarization dependence in cells operated with biogas fuel, indicating that reactions 7.2 and 7.3 are modulated largely by $CO_{2(g)}$ in the fuel stream, rather than the electrochemical oxide flux.

The current studies also provide some insight into pertinent heterogeneous chemical mechanisms. Raman spectra collected from the nickel surface indicate that Ni-CH_x is present during methane exposure only at the lower operating temperatures but disappears at 800 °C (Figure 7.2b). From a thermodynamically-based model developed by Deutschmann and coworkers, complete dehydrogenation of CH_4 to $C_{(s)}$ and H_2 on nickel should occur according to the following series of elementary reactions:[59]

7.5. $CH_{4(s)} + Ni_{(s)} \rightarrow CH_{3(s)} + H_{(s)}$ $\mathbf{k_{,800°C}}$ ($k_{,700°C}$) = **5.7 x 10^{18}** (3.0 x 10^{18})[c]

7.6. $CH_{3(s)} + Ni_{(s)} \rightarrow CH_{2(s)} + H_{(s)}$ $\mathbf{k_{,800°C}}$ ($k_{,700°C}$) = **5.0 x 10^{19}** (1.6 x 10^{19})

7.7. $CH_{2(s)} + Ni_{(s)} \rightarrow CH_{(s)} + H_{(s)}$ $\mathbf{k_{,800°C}}$ ($k_{,700°C}$) = **6.9 x 10^{19}** (2.3 x 10^{19})

7.8. $CH_{(s)} + Ni_{(s)} \rightarrow C_{(s)} + H_{(s)}$ $\mathbf{k_{,800°C}}$ ($k_{,700°C}$) = **4.5 x 10^{20}** (3.6 x 10^{20})

From these rate constants, we calculate that the forward reaction rate of CH_2 decomposition increases by more than a factor of three as temperature increases from 700 °C to 800 °C. This result may explain the loss of the weak (S/N ~2) Raman 2920 cm^{-1} signature at 800 °C under methane. Under biogas, this signature was rarely observed at 700 °C, implying that $O_{(ads)}$ might assist the dissociation of $CH_{x(s)}$, as well as react with $C_{(s)}$, in the reforming process[152], contrasting with assertions made by others.[56, 59]

[c] Rate Constant Units: cm, mol, s

Conclusions

The direct, *in operando* optical measurements described here highlight behaviors that implicate anode dry reforming processes as dominating SOFC anode surface chemistry. For example, NIR thermal imaging has demonstrated that surface cooling strongly varies as a function of temperature for biogas. On the other hand, methane decomposition to carbon and hydrogen showed very little cooling - a trend contrasting with larger fuels and alcohols. Carbon growth was seen to increase with temperature under this fuel, but dry reforming led to less carbon growth and higher CO mole fractions at high temperatures, which is thought to be modulated by the Boudouard reaction. Raman spectroscopy has indicated that intermediate Ni-CH_x species are influenced by the dry reforming process, but more rigorous studies that explore the kinetic and mechanistic relevance of this signature remain to be completed.

Collectively, these techniques provide data to elucidate a consistent portrait of heterogeneous Ni-based anode chemistry that is based upon direct, molecularly specific observations. These techniques promise utility in corroborating experimental models that often lack *in operando*, molecularly specific observation. However, further studies that begin to account for system-dependent parameters need to be completed to help identify both thermodynamic and kinetic contributions to optical and electrochemical observations to extract more detailed interpretations.

CHAPTER 8

FINAL REMARKS

Conclusions

Taken as a whole, studies described in this dissertation have demonstrated that SOFC operation with biogas has a bright future, particularly because biogas is associated with much less deleterious carbon accumulation relative to other hydrocarbon fuels.[52, 54, 93] This work has shown that carbon dioxide naturally present in biogas transforms methane (also present in this fuel) into simpler products (CO and H_2) that inhibit (but don't prevent) carbon formation on functioning SOFC anodes. This work has also demonstrated that methane fuel (i.e. biogas scrubbed of CO_2), leads to significant carbon accumulation. This result is not a surprise and has been documented elsewhere,[54] though not with direct, *in operando* observation.

However, this result alone does not account for the complex electrochemical and catalytic processes that take place within the Ni/YSZ anode when a SOFC is operated with biogas. Understanding these processes on a fundamental level is important to understand chemical mechanisms that can be associated with device degradation—ultimately enabling informed operational and design decisions that lead to maximal performance and longevity.

For example, Chapters 6 and 7 demonstrated that carbon can still form on a SOFC anode operated with biogas according to the Boudouard reaction:

8.1. $2CO_{(g)} \leftrightarrow CO_{2(g)} + C_{(s)}$

The *in operando* optical and electrochemical techniques utilized in these studies independently demonstrated that the equilibrium of this reaction in an operational SOFC is strongly influenced by temperature as well as by the operational current, and that carbon accumulation occurs more prevalently at lower operational temperatures and lower current loads.

Several studies[57, 59, 152, 178] have modeled the elementary kinetic reactions on the surface to predict mechanistically how these processes take place. A few have described the dry reforming reaction (equation 8.2) as the coupling of equations 8.1 and 8.3:

8.2. $CH_{4(g)} + CO_{2(g)} \rightarrow 2CO_{(g)} + 2H_{2(g)}$

8.3. $CH_{4(g)} \rightarrow C_{(s)} + H_{2(g)}$

Interestingly, Chapter 5 demonstrated that surface carbon could be removed via the reverse of equation 8.1. This result suggests that this reaction plays an important role in alleviating carbon formation when Ni/YSZ anodes are operated with biogas. However, a Ni-CH_x Raman signature observed *in operando* under CH_4 fuel (without CO_2) but not under biogas fuel (first reported in Chapter 7) suggesting that CO_2 may not only react with $C_{(s)}$ as in equation 8.1, but also with a Ni-CH_x intermediate. These results mark some of the first direct mechanistic insights during SOFC operation and provide a starting point for future studies that are needed to further test model predictions.

Some of the insights above regarding carbon accumulation required a technique capable of quantifying these deposits *in operando*. Raman spectroscopy alone will provide a measure of the *relative* amounts of deposited carbon, but this technique samples the surface only (where the penetration depth[73] is limited to the first several

hundred nm, accounting for porosity) — and experimental variability limits quantitative comparisons between multiple experiments. Chapters 3 and 4 describe the development of a technique coined "Spectrochronopotentiometry" (SCP), an integration of chronopotentiometric measurements with Raman spectra collected in real time. These studies ascertained that within pristine anodes having ample TPBs, virtually all previously deposited carbon could be electrochemically oxidized. The SOFCs used were ideal for these measurements—possessing thin Ni/YSZ anodes (~30 μm) of homogenous composition. In these cells, the anode surface carbon sampled by Raman spectroscopy was relatively close to the carbon sampled by chronopotentiometry (preferentially electrochemically oxidized first nearer the electrolyte interface).

Chapters 3 and 4 describe an important, additional conclusion made from these SCP measurements. Electrochemical oxidation of carbon requires proximity near a TPB as well as connectivity of each phase throughout the entire microstructure. Once a cell began to deteriorate (specifically, decreased TPB length/cermet volume), less carbon was "electrochemically accessible." This understanding was important in interpreting chronopotentiometric results in Chapter 7. These measurements showed a clear difference in the carbon sampled by Raman spectroscopy and that sampled by chronopotentiometric measurements—differences accentuated by a thick anode (~800 μm). Indeed, for SOFCs operated with biogas, Raman measurements did not generally indicate carbon accumulation on the surface, but chronopoteniometry indicated that carbon did form nearer the electrolyte interface. This result suggests different chemistry that depends upon location within the anode cross section.

Finally, Chapter 5 also demonstrated that prolonged exposure of a nickel-based anode to CO_2 can oxidize the nickel itself, an important consideration when operating an SOFC with excessively lean fuel mixtures. From Chapter 2, nickel oxidation (from O_2 and H_2O) caused morphological changes within the anode microstructure, and others have associated this phenomenon with irreversible degradation. Lanzini et al. attributed MEA power losses under excessively lean biogas fuel mixtures to nickel oxidation.[54] However, Chapter 5 demonstrated that CO_2 only partially oxidized the nickel, a significant advantage relative to O_2 exposure that completely oxidizes nickel. However, this understanding is important in the context of designing MEAs that effectively operate with biogas sources containing lean CO_2:CH_4 ratios.

Collectively, this work has demonstrated the importance of directly observing chemical processes occurring in SOFCs and corroborating *in operando* data with predictions from theoretical studies and data from other, indirect measurements. These studies also inspire confidence that continued development of direct, optical techniques and experimental methods will enable quantitative validation of model-based electrochemical oxidation mechanisms.

Future Direction

Investigations of Biogas Fuel Chemistry on Electrolyte Supported MEAs

Because the MEAs tested in Chapters 6 and 7 were anode supported, the optically-observed surface phenomena were relatively far removed from the electrochemically active region near the electrolyte, ~800 μm below the anode surface.

Girona et al. determined that gas composition and reaction rates vary sharply according to location through the anode cross section,[58] even in the absence of electrochemistry. Furthermore, the surface support layer in the MEAs tested in this work was of a different density from the functional layer nearer the electrolyte.[158] We also note that Raman spectroscopy in particular only penetrates about 10-20 nm into pure solid nickel, and the porous microstructure only extends total penetration to several hundred nm.[73] FTIR emission spectroscopy suffers from similar limitations.

To more directly probe anode chemistry nearer the electrolyte interface, studies similar to those performed in Chapters 6 and 7 have been initiated, but on MEAs with thin (~50 μm) Ni/YSZ anodes. The optical diagnostics from these MEAs should be more representative of electrochemistry occurring near the electrolyte interface. Figure 8.1 describes measurements collected using FTIR emission spectroscopy and NIR thermal imaging from these alternative MEAs. In each experiment, an SOFC was operated with three different fuel mixtures (1:1 CO_2:CH_4 (BG), 4:25 H_2O:CH_4 and CH_4, diluted with Ar) and at OCV and 75% I_{max} and at 700 °C or 800 °C. These studies have begun testing an additional fuel mixture, wet CH_4, to understand the effects of humidity on the reforming process and carbon accumulation. In general, a comparison of results from MEAs operated with BG and CH_4 show trends similar to those depicted in Chapter 7.

A few subtle differences do exist, however, and warrant further investigation into how surface observables might change as a function of anode thickness and/or composition. First, surface cooling under biogas is much more pronounced in these new MEAs—this contrast is most significant at the lower operating temperature (700 °C).

Second, methane demonstrates less cooling relative to the MEAs with thick anodes. Our research group and our collaborators at NRL continue to examine these effects to test their generality of these findings.

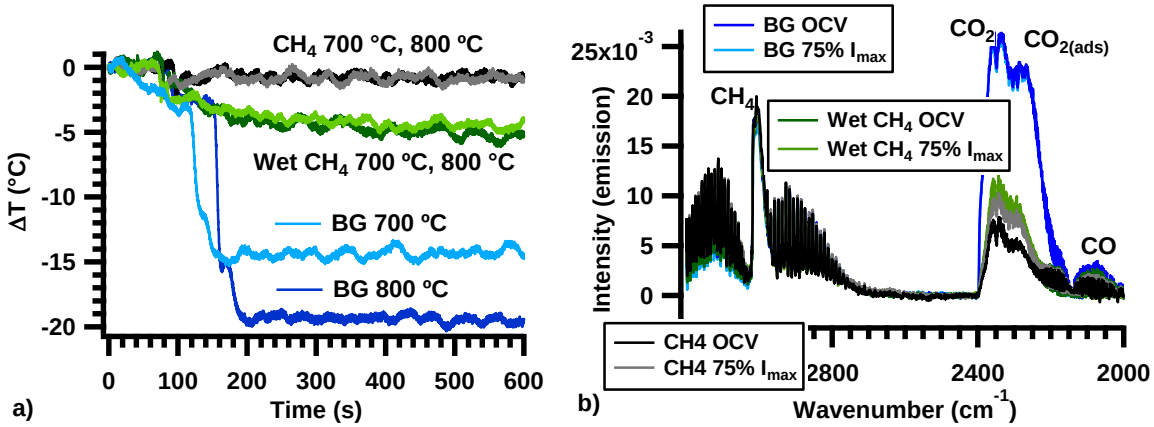

Figure 8.1. NIR thermal images collected during SOFC operation at 700 and 800 °C with different fuel flows at OCV on electrolyte-supported MEAs with ~50 µm thick Ni/YSZ anodes are shown in (a). FTIR emission spectra collected from similar MEAs and fuel flows (800 °C) but at OCV *and* 75% I_{max} are shown in (b).

Operation of SOFCs with *n*-Butanol

Bio-derived butanol has recently attracted interest as a viable product from agricultural feedstocks, using technology similar to that used for ethanol production.[5, 180] Investigations assessing the viability of SOFC operation with butanol are almost absent in the literature. Sasaki et al. monitored the electrochemical behavior and exhaust compositions of Ni/YSZ based SOFCs and showed that larger alcohols (in particular butanol) experienced less complete conversion to more labile products such as CO and H_2 and instead formed more deleterious species such as C_2H_4 and C_6H_6.[181] Green and coworkers demonstrated that n-butanol experiences complex gas-phase chemistry en

route to wide spectrum of simpler products in high temperature (807 °C maximum) pyrolysis experiments.[182]

Studies by our research group and collaborators at NRL are currently underway to better understand the chemical origins of electrochemical performance of MEAs operating with n-butanol using *in operando* optical techniques and electrochemical measurements. In these experiments, a Ni/YSZ anode-supported SOFC is operated at 800 °C with plain n-butanol (4 mL/min BuOH, 146 mL/min Ar) as well as with humidified n-butanol (3 mL/min H_2O, 1 mL/min BuOH, 164 mL/min Ar and 4 mL/min H_2O, 4 mL/min BuOH, 326 mL/min Ar) at various polarizations. Humidified BuOH is included in these studies to understand if wet reforming might lessen or eliminate any carbon formation and lead to more viable SOFC operation.

During a ~10 minute test, an MEA operated with plain n-butanol offered improved power output relative to humidified BuOH and H_2 shown in Figure 8.2a. In this same experiment, Raman spectra collected during fuel exposure indicated that, at the anode surface, graphitic carbon (indicated by the "G" signal in Figure 8.2b) only formed under plain BuOH. This carbon appears to lead to severe anode degradation at the surface, though other measurements (not shown) indicate that deep within the anode and nearer the electrochemically active region, carbon formation is virtually absent.

In a similar experiment, an analysis of SOFC exhaust products demonstrated that some species and their mole fractions were dependent upon fuel, and in some cases the current load. Notably, virtually no n-BuOH signature (broad feature near 2950 cm^{-1}) is present in Figure 8.3. Direct observation (via FTIR emission spectroscopy) of gas species

(not shown) over an operating anode indicate that emission features vary according to fuel and polarization in a different manner—suggesting that gas composition over the anode is not identical to exhaust products.

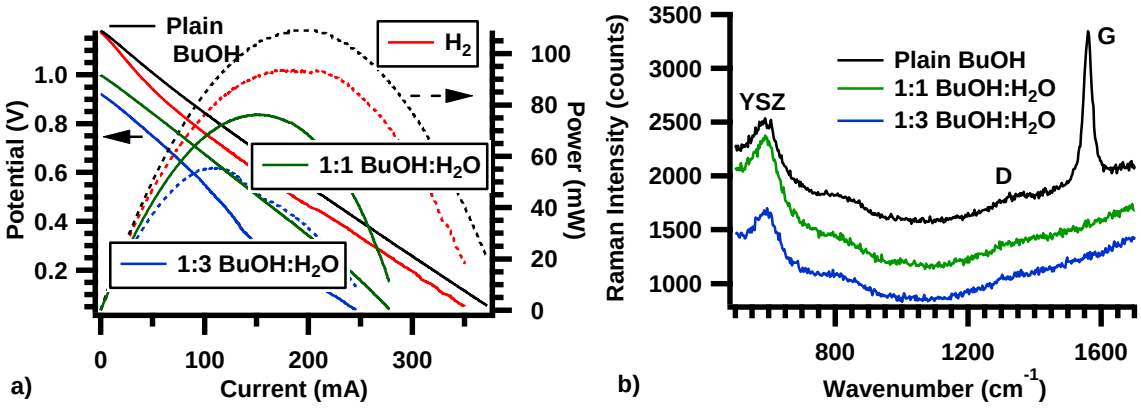

Figure 8.2. LSV measurements collected during SOFC operation under humidified BuOH, wet BuOH, and H_2 at 800 °C are shown in (a). Raman measurements collected while the same MEA is operated at OCV with the same fuels is shown in (b).

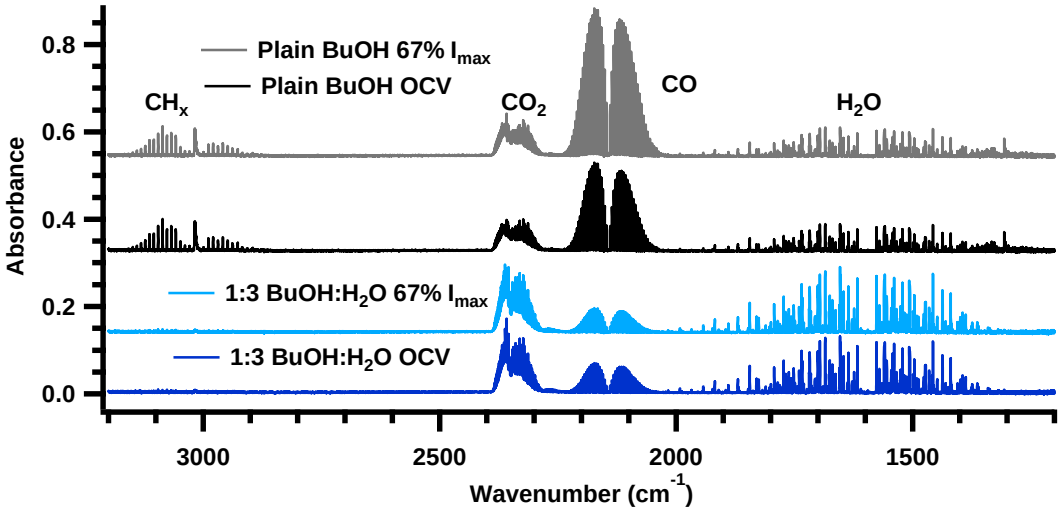

Figure 8.3. An FTIR analysis of exhaust products from plain and humidified n-Butanol exiting an SOFC operated at 800 °C.

Data shown here represent only a small subset of experiments that have utilized NIR thermal imaging, FTIR emission spectroscopy, Raman spectroscopy, and chronopotentiometry to better understand fuel chemistry. However, homogeneous and heterogeneous chemistry of BuOH in an operating SOFC is complex. To better understand how these vary with operational conditions, continued analysis of existing data is needed, coupled with additional experiments that delineate reactions in the gas and condensed phase. Experiments that equalize carbon loading and total flow rates, if possible, will be important. Furthermore, experiments using a combination of Raman spectroscopy, chronopotentiometry, and cross-sectional analysis (*ex situ*) may help isolate where within the anode carbon forms. These experiments will also help diagnose microstructural changes that evolve with carbon growth. This information will in turn provide insight into mechanisms responsible for MEA degradation from butanol.

REFERENCES CITED

(1) International Energy Agency. 2012. *World energy outlook 2012* [online] (Paris). www.worldenergyoutlook.org (accessed 08 Oct. 2014)

(2) Organization of the Petroleum Exporting Countries. 2014. *2014 world oil outlook* [online] (Vienna). http://www.opec.org/opec_web/static_files_project/media/downloads/publications/WOO_2014.pdf (accessed 08 Nov 2014)

(3) REN21. 2013. *Renewables 2013 global status report* [online] (Paris). http://www.ren21.net/ren21activities/globalstatusreport.aspx (accessed 08 Oct. 2014)

(4) Ho, D. P.; Huu Hao, N. and Guo, W. A mini review on renewable sources for biofuel. *Bioresour. Technol.* **2014**, *169*, 742-749.

(5) REN21. 2014. *Renwables 2014 global status report* [online] (Paris). http://www.ren21.net/ren21activities/globalstatusreport.aspx (accessed 08 Oct. 2014)

(6) Hahn, H.; Krautkremer, B.; Hartmann, K. and Wachendorf, M. Review of concepts for a demand-driven biogas supply for flexible power generation. *Ren. & Sust. En. Rev.* **2014**, *29*, 383-393.

(7) European Biogas Association. 2011. *Biogas: Simply the best* [online] (Brussels). http://european-biogas.eu/biogas/ (accessed 09 Oct. 2014)

(8) Fierro, J.; Gomez, X. and Murphy, J. D. What is the resource of second generation gaseous transport biofuels based on pig slurries in Spain? *Appl. Energy* **2014**, *114*, 783-789.

(9) Al Seadi, T.; Rutz, D. R.; Prassl, H.; Köttner, M.; Finsterwalder, T.; Volk, S. and Janssen, R. Utilisation of Biogas In *Biogas handbook* [online]*;* T. Al Seadi, University of Southern Denmark Esbjerg, Niels Bohrs Vej 9-10: Esbjerg, Denmark, 2008; www.lemvigbiogas.com (accessed Nov. 7, 2014)

(10) Song, C. Fuel processing for low-temperature and high-temperature fuel cells Challenges, and opportunities for sustainable development in the 21st century. *Cat. Today* **2002**, *77*, 17-49.

(11) Ormerod, R. M. Solid oxide fuel cells. *Chem. Soc. Rev.* **2003**, *32*, 17-28.

(12) Singhal, S. C. Advances in solid oxide fuel cell technology. *Solid State Ionics* **2000**, *135*, 305-313.

(13) Kee, R. J.; Zhu, H. and Goodwin, D. G. Solid-oxide fuel cells with hydrocarbon fuels. *Proc. Combust. Inst.* **2005**, *30*, 2379-2404.

(14) Liu, M.; Lynch, M. E.; Blinn, K.; Alamgir, F. M. and Choi, Y. Rational SOFC material design: new advances and tools. *Mater. Today* **2011**, *14*, 11, 534-546.

(15) Haile, S. M. Fuel cell materials and components. *Acta Mater.* **2003**, *51*, 19, 5981-6000.

(16) Lawlor, V. Review of the micro-tubular solid oxide fuel cell (Part II: Cell design issues and research activities). *J. Power Sources* **2013**, *240*, 421-441.

(17) Erning, J. W.; Hauber, T.; Stimming, U. and Wippermann, K. Catalysis of the electrochemical processes on solid oxide fuel cell cathodes. *J. Power Sources* **1996**, *61*, 1-2, 205-211.

(18) Goodenough, J. B. Oxide-ion electrolytes. *Annu. Rev. Mater. Res.* **2003**, *33*, 91-128.

(19) Devanathan, R.; Weber, W. J.; Singhal, S. C. and Gale, J. D. Computer simulation of defects and oxygen transport in yttria-stabilized zirconia. *Solid State Ionics* **2006**, *177*, 15-16, 1251-1258.

(20) Chater, R. J.; Carter, S.; Kilner, J. A. and Steele, B. C. H. Development of a novel SIMS technique for oxygen self-diffusion and surface exchange coefficient measurements in oxides of high diffusivity. *Solid State Ionics* **1992**, *53*, 859-867.

(21) Eguchi, K.; Setoguchi, T.; Inoue, T. and Arai, H. Electrical-properties of ceria-based oxides and their application to solid oxide fuel-cells. *Solid State Ionics* **1992**, *52*, 1-3, 165-172.

(22) Steele, B. C. H. Appraisal of Ce1-yGdyO2-y/2 electrolytes for IT-SOFC operation at 500 degrees C. *Solid State Ionics* **2000**, *129*, 1-4, 95-110.

(23) Sarat, S.; Sammes, N. and Smirnova, A. Bismuth oxide doped scandia-stabilized zirconia electrolyte for the intermediate temperature solid oxide fuel cells. *J.Power Source* **2006**, *160*, 2, 892-896.

(24) Yokokawa, H.; Sakai, N.; Horita, T.; Yamaji, K. and Brito, M. E. Electrolytes for solid-oxide fuel cells. *Mrs Bulletin* **2005**, *30*, 8, 591-595.

(25) Jacobson, A. J. Materials for solid oxide fuel cells. *Chem. Mater.* **2010**, *22*, 3, 660-674.

(26) Joos, J.; Ender, M.; Rotscholl, I.; Menzler, N. H. and Ivers-Tiffee, E. Quantification of double-layer Ni/YSZ fuel cell anodes from focused ion beam tomography data. *J. Power Source* **2014**, *246*, 819-830.

(27) Huang, Y. H.; Dass, R. I.; Xing, Z. L. and Goodenough, J. B. Double perovskites as anode materials for solid-oxide fuel cells. *Science* **2006**, *312*, 5771, 254-257.

(28) Childs, N. B.; Wesinstein, A.; Smith, R.; Sofie, S. and Key, C. Electrical conductivity of Sr2-xVMoO6-y (x=0.0, 0.1, 0.2) double perovskites. *J. Appl. Phys.* **2013**, *113*, 24, 243506-1 - 243506-9.

(29) Ruiz-Morales, J. C.; Canales-Vazquez, J.; Savaniu, C.; Marrero-Lopez, D.; Zhou, W. Z. and Irvine, J. T. S. Disruption of extended defects in solid oxide fuel cell anodes for methane oxidation. *Nature* **2006**, *439*, 7076, 568-571.

(30) Chen, X. J.; Liu, Q. L.; Chan, S. H.; Brandon, N. P. and Khor, K. A. High performance cathode-supported SOFC with perovskite anode operating in weakly humidified hydrogen and methane. *Electrochem. Commun.* **2007**, *9*, 4, 767-772.

(31) Mogensen, D.; Grunwaldt, J. D.; Hendriksen, P. V.; Dam-Johansen, K. and Nielsen, J. U. Internal steam reforming in solid oxide fuel cells: Status and opportunities of kinetic studies and their impact on modelling. *J. Power Source* **2011**, *196*, 1, 25-38.

(32) Balat, M. and Balat, H. Biogas as a renewable energy source: A review. *Energy Sources, A* **2009**, *31*, 14, 1280-1293.

(33) International Energy Agency. 2007. *Biomass for power generation and CHP* [online] (Paris). http://www.iea.org/techno/essentials3.pdf (accessed 08 Oct. 2014)

(34) Van herle, J.; Marechal, F.; Leuenberger, S. and Favrat, D. Energy balance model of a SOFC cogenerator operated with biogas. *J. Power Sources* **2003**, *118*, 1-2, 375-383.

(35) Gandiglio, M.; Lanzini, A.; Santarelli, M. and Leone, P. Design and balance-of-plant of a demonstration plant with a solid oxide fuel cell fed by biogas from waste-water and exhaust carbon recycling for algae growth. *Journal of Fuel Cell Science and Technology* **2014**, *11*, 3, 031003-1-031003-13.

(36) Papadam, T.; Goula, G. and Yentekakis, I. V. Long-term operation stability tests of intermediate and high temperature Ni-based anodes' SOFCs directly fueled with simulated biogas mixtures. *Int. J. Hydrogen Energy* **2012**, *37*, 21, 16680-16685.

(37) Wongchanapai, S.; Iwai, H.; Saito, M. and Yoshida, H. Performance evaluation of a direct-biogas solid oxide fuel cell-micro gas turbine (SOFC-MGT) hybrid combined heat and power (CHP) system. *J. Power Sources* **2013**, *223*, 9-17.

(38) McLarty, D.; Brouwer, J. and Samuelsen, S. Hybrid fuel cell gas turbine system design and optimization. *J. Fuel Cell Sci. Technol.* **2013**, *10*, 4,

(39) Dalrymple, O. K.; Halfhide, T.; Udom, I.; Gilles, B.; Wolan, J.; Zhang, Q. and Ergas, S. Wastewater use in algae production for generation of renewable resources: a review and preliminary results. *Aquatic biosystems* **2013**, *9*, 1, 2-2.

(40) Pittman, J. K.; Dean, A. P. and Osundeko, O. The potential of sustainable algal biofuel production using wastewater resources. *Bioresour. Technol.* **2011**, *102*, 1, 17-25.

(41) Hammad, M.; Badarneh, D. and Tahbouba, K. Evaluating variable organic waste to produce methane. *Energ. Conser. Manag.* **1999**, *40*, 1463-1475.

(42) Rasi, S.; Veijanen, A. and Rintala, J. Trace compounds of blogas from different blogas production plants. *Energy* **2007**, *32*, 8, 1375-1380.

(43) Weiland, P. Biogas production: current state and perspectives. *Appl. Microbiol. Biotechnol.* **2010**, *85*, 4, 849-860.

(44) Haga, K.; Adachi, S.; Shiratori, Y.; Itoh, K. and Sasaki, K. Poisoning of SOFC anodes by various fuel impurities. *Solid State Ionics* **2008**, *179*, 1427-1431.

(45) Laurencin, J.; Delette, G.; Sicardy, O.; Rosini, S. and Lefebvre-Joud, F. Impact of 'redox' cycles on performances of solid oxide fuel cells: Case of the electrolyte supported cells. *J. Power Sources* **2010**, *195*, 2747-2753.

(46) Zhang, Y.; Liu, B.; Tu, B.; Dong, Y. and Cheng, M. Understanding of redox behavior of Ni-YSZ cermets. *Solid State Ionics* **2009**, *180*, 1580-1586.

(47) Waldbillig, D.; Wood, A. and Ivey, D. G. Thermal analysis of the cyclic reduction and oxidation behaviour of SOFC anodes. *Solid State Ionics* **2005**, *176*, 9-10, 847-859.

(48) McIntosh, S. and Gorte, R. J. Direct hydrocarbon solid oxide fuel cells. *Chem. Rev.* **2004**, *104*, 10, 4845-4865.

(49) Finnerty, C. M.; Coe, N. J.; Cunningham, R. H. and Ormerod, R. M. Carbon formation on and deactivation of nickel-based/zirconia anodes in solid oxide fuel cells running on methane. *Cat. Today* **1998**, *46*, 137-145.

(50) Gorte, R. J.; Park, S.; Vohs, J. M. and Wang, C. H. Anodes for direct oxidation of dry hydrocarbons in a solid-oxide fuel cell. *Adv. Mater.* **2000**, *12*, 19, 1465-1469.

(51) Bartholomew, C. H. Carbon deposition in steam reforming and methanation. *Catal. Rev.-Sci. Eng.* **1982**, *24*, 1, 67-112.

(52) Pomfret, M. B.; Marda, J.; Jackson, G. S.; Eichhorn, B. W.; Dean, A. M. and Walker, R. A. Hydrocarbon fuels in solid oxide fuel cells: In situ Raman studies of graphite formation and oxidation. *J. Phys. Chem. C* **2008**, *112*, 13, 5232-5240.

(53) Baker, R. T. K.; Barber, M. A.; Waite, R. J.; Harris, P. S. and Feates, F. S. Nucleation and growth of carbon deposits from nickel catalyzed decomposition of acetylene. *J. Catal.* **1972**, *26*, 1, 51-62.

(54) Lanzini, A.; Leone, P.; Guerra, C.; Smeacetto, F.; Brandon, N. P. and Santarelli, M. Durability of anode supported Solid Oxides Fuel Cells (SOFC) under direct dry-reforming of methane. *Chem. Eng. J.* **2013**, *220*, 254-263.

(55) He, H. and Hill, J. M. Carbon deposition of Ni/YSZ composites exposed to humidified methane. *Appl Cat. A* **2007**, *317*, 284-292.

(56) Wei, J. M. and Iglesia, E. Isotopic and kinetic assessment of the mechanism of reactions of CH4 with CO2 or H2O to form synthesis gas and carbon on nickel catalysts. *J. Catal.* **2004**, *224*, 2, 370-383.

(57) Hecht, E. S.; Gupta, G. K.; Zhu, H. Y.; Dean, A. M.; Kee, R. J.; Maier, L. and Deutschmann, O. Methane reforming kinetics within a Ni-YSZ SOFC anode support. *Appl. Catal., A* **2005**, *295*, 1, 40-51.

(58) Girona, K.; Laurencin, J.; Fouletier, J. and Lefebvre-Joud, F. Carbon deposition in CH4/CO2 operated SOFC: Simulation and experimentation studies. *J. Power Sources* **2012**, *210*, 381-391.

(59) Maier, L.; Schaedel, B.; Delgado, K. H.; Tischer, S. and Deutschmann, O. Steam reforming of methane over nickel: Development of a multi-step surface reaction mechanism. *Top. Catal.* **2011**, *54*, 13-15, 845-858.

(60) Pomfret, M. B.; Owrutsky, J. C. and Walker, R. A. High-temperature Raman spectroscopy of solid oxide fuel cell materials and processes. *J. Phys. Chem. B* **2006**, *110*, 35, 17305-17308.

(61) Pomfret, M. B.; Owrutsky, J. C. and Walker, R. A. In Situ studies of fuel oxidation in solid oxide fuel cells. *Anal. Chem.* **2007**, *79*, 2367-2372.

(62) Pomfret, M. B.; Steinhurst, D. A.; Kidwell, D. A. and Owrutsky, J. C. Thermal imaging of solid oxide fuel cell anode processes. *J. Power Sources* **2010**, *195*, 257-262.

(63) Pomfret, M. B.; Owrutsky, J. C. and Walker, R. A. In situ optical studies of solid-oxide fuel cells. In *Annual Review of Analytical Chemistry, Vol 3;* E. S. Yeung and R. N. Zare, Eds.; **2010**; 151-174.

(64) Bard, A. and Faulkner, L. *Electrochemical methods: Fundamentals and applications;* 2nd ed.; John Wiley and Sons, Inc.: Hoboken, NJ, 2001; 383-387.

(65) Hofmann, P. and Panopoulos, K. Detailed dynamic solid oxide fuel cell modeling for electrochemical
impedance spectra simulation. *J. Power Source* **2010**, *195*, 5320-5339.

(66) Bieberle, A. M.; Meier, L. P. and Gauckler, L. J. The electrochemistry of Ni pattern anodes used as solid oxide fuel cell model electrodes. *J. Electrochem. Soc.* **2001**, *148*, 6, A646-A656.

(67) Harris, D. and Michael, B. *Symmetry and spectroscopy: An introduction to vibrational and electronic spectroscopy;* Dover Publications, Inc.: New York, 1978; 97-100.

(68) Xu, C. K.; Xu, G. D. and Wang, G. H. Preparation and characterization of NiO nanorods by thermal decomposition of NiC2O4 precursor. *J. Mater. Sci.* **2003**, *38*, 4, 779-782.

(69) Reich, S. and Thomsen, C. Raman spectroscopy of graphite. *Phil. Trans. R. Soc. Lond. A* **2004**, *362*, 1824, 2271-2288.

(70) Tuinstra, F. and Koenig, J. L. Raman spectrum of graphite. *J. Chem. Physics* **1970**, *53*, 3, 1126-1130.

(71) Wang, Y.; Alsmeyer, D. C. and McCreery, R. L. Raman spectroscopy of carbon materials: Structural basis of observed spectra. *Chem. Mater.* **1990**, *2*, 5, 557-563.

(72) Lin-Vien, D.; Colthup, N. B.; Fateley, W. G. and Grasselli, J. G. *The handbook of infrared and Raman characteristic frequencies of organic molecules;* Academic Press: San Diego, 1991; 9-13.

(73) Duboviks, V.; Maher, R. C.; Kishimoto, M.; Cohen, L. F.; Brandon, N. P. and Offer, G. J. A Raman spectroscopic study of the carbon deposition mechanism on Ni/CGO electrodes during CO/CO2 electrolysis. *Phys. Chem. Chem. Phys.* **2014**, *16*, 26, 13063-13068.

(74) Blinn, K. S.; Abernathy, H.; Li, X. X.; Liu, M. F.; Bottomley, L. A. and Liu, M. L. Raman spectroscopic monitoring of carbon deposition on hydrocarbon-fed solid oxide fuel cell anodes. *Energ. Environ. Sci.* **2012**, *5*, 7, 7913-7917.

(75) Takahashi, Y.; Shiratori, Y.; Furuta, S. and Sasaki, K. Thermo-mechanical reliability and catalytic activity of Ni-Zirconia anode supports in internal reforming SOFC running on biogas. *Solid State Ionics* **2012**, *225*, 113-117.

(76) Brett, D. J. L.; Aguiar, P.; Clague, R.; Marquis, A. J.; Schottl, S.; Simpson, R. and Brandon, N. P. Application of infrared thermal imaging to the study of pellet solid oxide fuel cells. *J. Power Sources* **2007**, *166*, 1, 112-119.

(77) Pomfret, M. B.; Steinhurst, D. A. and Owrutsky, J. C. Identification of a methane oxidation intermediate on solid oxide fuel cell anode surfaces with fourier transform infrared emission. *J. Phys. Chem. Lett.* **2013**, *4*, 8, 1310-1314.

(78) Lu, X. Y.; Faguy, P. W. and Liu, M. L. In situ potential-dependent FTIR emission spectroscopy - A novel probe for high temperature fuel cell interfaces. *J. Electrochem. Soc.* **2002**, *149*, 10, A1293-A1298.

(79) Chen, A.; Bourne, G.; Siebein, K.; DeHoff, R.; Wachsman, E. and Jones, K. Characterization of lanthanum zirconate formation at the A-site-deficient strontium-doped lanthanum manganite cathode/yttrium-stabilized zirconia electrolyte interface of solid oxide fuel cells. *J. Am. Ceram. Soc.* **2008**, *91*, 8, 2670-2675.

(80) Cheng, Z.; Abernathy, H. and Liu, M. Raman spectroscopy of nickel sulfide Ni3S2. *J. Phys. Chem. C* **2007**, *111*, 49, 17997-18000.

(81) Maher, R. C. and Cohen, L. F. Raman spectroscopy as a probe of temperature and oxidation state for gadolinium-doped ceria used in solid oxide fuel cells. *J. Phys. Chem. A* **2008**, *112*, 7, 1497-1501.

(82) Finnerty, C. M. and Ormerod, R. M. Internal reforming over nickel/zirconia anodes in SOFCS oparating on methane: influence of anode formulation, pre-treatment and operating conditions. *J. Power Sources* **2000**, *86*, 1-2, 390-394.

(83) Tikekar, N. N.; Armstrong, T. J. and Virkar, A. V. Reduction and reoxidation kinetics of nickel-based SOFC anodes. *J. Electrochem. Soc.* **2006**, *153*, 4, A654-A663.

(84) Fouquet, D.; Mueller, A. C.; Weber, A. and Ivers-Tiffee, E. Kinetics of oxidation and reduction of Ni/YSZ cermets. *Ionics* **2003**, *8*, 103-108.

(85) Stathis, G.; Simwonis, D.; Tietz, F.; Moropoulou, A. and Naoumides, A. Oxidation and resulting mechanical properties of Ni/8Y2O3-stabilized zirconia anode substrate for solid-oxide fuel cells. *J. Mater. Res.* **2002**, *17*, 5, 951-958.

(86) Zhu, H. and Kee, R. J. Modeling electrochemical impedance spectra in SOFC button cells with internal methane reforming. *J. Electrochem. Soc.* **2006**, *153*, 9, A1765-A1772.

(87) Karmhag, R.; Nicklasson, G. and Nygren, M. Oxidation kinetics of small nickel particles. *J. Appl. Phys.* **1999**, *85*, 2, 1186-1191.

(88) Carter, R. E. Kinetic model for solid state reactions. *J. Chem. Phys.* **1961**, *34*, 2010-2015.

(89) Brett, D. J. L.; Atkinson, A.; Brandon, N. P. and Skinner, S. J. Intermediate temperature solid oxide fuel cells. *Chem. Soc. Rev.* **2008**, *37*, 1568-1578.

(90) Baker, R. T. and Metcalfe, I. S. Study of the activity and deactivation of Ni-YSZ cermet in dry CH4 using temperature-programmed techniques. *Ind. Eng. Chem. Res.* **1995**, *34*, 1558-1565.

(91) Trimm, D. L. The formation and removal of coke from nickel catalyst. *Cat. Rev. Sci. Eng.* **1977**, *16*, 2, 155-189.

(92) Alzate-Restrepo, V. and Hill, J. M. Carbon deposition on Ni/YSZ anodes exposed to CO/H2 feeds. *J. Power Sources* **2010**, *195*, 1344-1351.

(93) Eigenbrodt, B. C.; Pomfret, M. B.; Steinhurst, D. A.; Owrutsky, J. C. and Walker, R. A. Direct, in situ optical studies of Ni-YSZ anodes in solid oxide fuel cells operating with methanol and methane. *J. Phys. Chem. C* **2011**, *115*, 2895-2903.

(94) Lin, Y.; Zhan, Z. and Barnett, S. A. Improving the stability of direct-methane solid oxide fuel cells using anode barrier layers. *J. Power Sources* **2006**, *158*, 2, 1313-1316.

(95) Lin, Y.; Zhan, Z.; Liu, J. and Barnett, S. A. Direct operation of solid oxide fuel cells with methane fuel. *Solid State Ionics* **2005**, *176*, 1827-1835.

(96) McIntosh, S.; Vohs, J. M. and Gorte, R. J. Role of hydrocarbon deposits in the enhanced performance of direct-oxidation SOFCs. *J. Electrochem. Soc.* **2003**, *150*, 4, A470-A476.

(97) McIntosh, S.; He, H. P.; Lee, S. I.; Costa-Nunes, O.; Krishnan, W.; Vohs, J. M. and Gorte, R. J. An examination of carbonaceous deposits in direct-utilization SOFC anodes. *J. Electrochem. Soc.* **2004**, *151*, 4, A604-A608.

(98) Pomfret, M. B.; Owrutsky, J. C. and Walker, R. A. A mechanistic understanding of solid oxide fuel cell chemistry through in-situ Raman spectroscopy. *Electrochem. Soc. Trans.* **2008**, *11*, 99-109.

(99) Li, X.; Blinn, K.; Fang, Y.; Liu, M.; Mahmoud, A. M.; Cheng, S.; Bottomley, L. A.; El-Sayed, M. and Liu, M. Application of surface enhanced Raman spectroscopy to the study of SOFC electrode surfaces. *Phys. Chem. Chem. Phys.* **2012**, *14*, 5919-5923.

(100) Zhang, C.; Grass, M. E.; McDaniel, A. H.; DeCaluwe, S. C.; Gabaly, F. A.; Liu, Z.; McCarty, K. F.; Farrow, R. L.; Linne, M. A.; Hussain, Z.; Jackson, G. S.; Bluhm, H. and Eichhorn, B. W. Measuring fundamental properties in operating solid oxide electrochemical cells by using in situ X-ray photoelectron spectroscopy. *Nat. Mater.* **2010**, *9*, 944-949.

(101) Eigenbrodt, B. C. High temperature mapping of surface electrolyte oxide concentration in solid oxide fuel cells with vibrational Raman spectroscopy. *Anal. Methods* **2011**, *3*, 7, 1478.

(102) Abernathy, H. W.; Koep, E.; Compson, C.; Cheng, Z. and Liu, M. Monitoring Ag-Cr interactions in SOFC cathodes using Raman spectroscopy. *J. Phys. Chem. C* **2008**, *112*, 13299-13303.

(103) Fee, J. A. and DiCorleto, P. E. Observations on the oxidation-reduction properties of bovine erythrocyte superoxide dismutase. *Biochemistry* **1973**, *12*, 4893-4899.

(104) Stombaugh, N. A.; Sundquist, J. E.; Burris, R. H. and Orme-Johnson, W. H. Oxidation-reduction properties of several low potential iron-sulfur proteins and of methylviologen. *Biochemistry* **1976**, *15*, 2633-2641.

(105) Sakmeche, N.; Aeiyach, S.; Aaron, J.; Jouni, M.; Lacroix, J. C. and Lacaze, P. Improvement of the electrosynthesis and physicochemical properties of poly(3,4-ethylenedioxythiophene) using a sodium dodecyl sulfate micellar aqueous medium. *Langmuir* **1999**, *15*, 2566-2574.

(106) Finnerty, C. M.; Coe, N. J.; Cunningham, R. H. and Ormerod, R. M. Development of a novel test system for in situ catlaytic, electrocatalytic and electrochemical studies of internal fuel reforming in solid oxide fuel cells. *Cat. Letters* **2000**, *66*, 221-226.

(107) Nikiel, L. and Jagodzinski, P. W. Raman spectroscopic characterization of graphites: A re-evaluation of spectra/structure correlation. *Carbon* **1993**, *31*, 8, 1313-1317.

(108) Kirtley, J. D.; Eigenbrodt, B. C. and Walker, R. A. In situ optical studies of oxidation kinetics of Ni/YSZ cermet anodes. *J. Electrochem. Soc. Trans.* **2011**, *33*, 40, 25-37.

(109) Offer, G. J. and Brandon, N. P. The effect of current density and temperature on the degradation of nickel cermet electrodes by carbon monoxide in solid oxide fuel cells. *Chem. Eng. Sci.* **2009**, *64*, 2291-2300.

(110) Rothman, L. S.; Gordon, I. E.; Barbe, A.; Benner, D. C.; Bernath, P. E.; Birk, M.; Boudon, V.; Brown, L. R.; Campargue, A.; Champion, J. P.; Chance, K.; Coudert, L. H.; Dana, V.; Devi, V. M.; Fally, S.; Flaud, J. M.; Gamache, R. R.; Goldman, A.; Jacquemart, D.; Kleiner, I.; Lacome, N.; Lafferty, W. J.; Mandin, J. Y.; Massie, S. T.; Mikhailenko, S. N.; Miller, C. E.; Moazzen-Ahmadi, N.; Naumenko, O. V.; Nikitin, A. V.; Orphal, J.; Perevalov, V. I.; Perrin, A.; Predoi-Cross, A.; Rinsland, C. P.; Rotger, M.; Simeckova, M.; Smith, M. A. H.; Sung, K.; Tashkun, S. A.; Tennyson, J.; Toth, R. A.; Vandaele, A. C. and Vander Auwera, J. The HITRAN 2008 molecular spectroscopic database. *J. Quant. Spectrosc. Radiat. Transfer* **2009**, *110*, 9-10, 533-572.

(111) Shao, Z.; Zhou, W. and Zhu, Z. Advanced synthesis of materials for intermediate-temperature solid oxide fuel cells. *Progress in Materials Science* **2012**, *57*, 804-874.

(112) Gorte, R. J. and Vohs, J. M. Novel SOFC anodes for the direct electrochemical oxidation of hydrocarbons. *J. Catal.* **2003**, *216*, 1-2, 477-486.

(113) McIntosh, S.; Vohs, J. M. and Gorte, R. J. Impedance spectroscopy for the characterization of Cu-Ceria-YSZ anodes for SOFCs. *J. Electrochem. Soc.* **2003**, *150*, 10, A1305-A1312.

(114) Hibino, T.; Hashimoto, A.; Asano, K.; Yano, M.; Suzuki, M. and Sano, M. An intermediate-temperature solid oxide fuel cell providing higher performance with hydrocarbons than with hydrogen. *Electrochem. Solid-State Lett.* **2002**, *5*, 11, A242-A244.

(115) Yang, L.; Choi, Y.; Qin, W. T.; Chen, H. Y.; Blinn, K.; Liu, M. F.; Liu, P.; Bai, J. M.; Tyson, T. A. and Liu, M. L. Promotion of water-mediated carbon removal by nanostructured barium oxide/nickel interfaces in solid oxide fuel cells. *Nature Communications* **2011**, *2*, 1-9.

(116) Tao, S. W. and Irvine, J. T. S. A redox-stable efficient anode for solid-oxide fuel cells. *Nat. Mater.* **2003**, *2*, 5, 320-323.

(117) Pomfret, M. B.; Walker, R. A. and Owrutsky, J. C. High-temperature chemistry in solid oxide fuel cells: In situ optical studies. *J. Phys. Chem. Lett.* **2012**, *3*, 3053-3064.

(118) Kirtley, J. D.; Halat, D. M.; McIntyre, M. D.; Eigenbrodt, B. C. and Walker, R. A. High-temperature "spectrochronopotentiometry": Correlating electrochemical performance with in situ Raman spectroscopy in solid oxide fuel cells. *Anal. Chem.* **2012**, *84*, 22, 9745-9753.

(119) Buccheri, M. A.; Singh, A. and Hill, J. M. Anode- versus electrolyte-supported Ni-YSZ/YSZ/Pt SOFCs: Effect of cell design on OCV, performance and carbon formation for the direct utilization of dry methane. *J. Power Sources* **2011**, *196*, 3, 968-976.

(120) Singh, A. and Hill, J. M. Carbon tolerance, electrochemical performance and stability of solid oxide fuel cells with Ni/yttria stabilized zirconia anodes impregnated with Sn and operated with methane. *J. Power Sources* **2012**, *214*, 0, 185-194.

(121) Alzate-Restrepo, V. and Hill, J. M. Effect of anodic polarization on carbon deposition on Ni/YSZ anodes exposed to methane. *Appl. Catal., A* **2008**, *342*, 1-2, 49-55.

(122) Singh, A.; Islam, S.; Buccheri, M. A. and Hill, J. M. Influence of experimental conditions on reliability of carbon tolerance studies on Ni/YSZ SOFC anodes operated with methane. *Fuel Cells* **2013**, *13*, 703-711.

(123) Kan, H.; Hyun, S. H.; Shul, Y. G. and Lee, H. Improved solid oxide fuel cell anodes for the direct utilization of methane using Sn-doped Ni/YSZ catalysts. *Catal. Commun.* **2009**, *11*, 3, 180-183.

(124) Nikolla, E.; Schwank, J. and Linic, S. Direct electrochemical oxidation of hydrocarbon fuels on SOFCs: Improved carbon tolerance of Ni alloy anodes. *J. Electrochem. Soc.* **2009**, *156*, 11, B1312-B1316.

(125) Kan, H. and Lee, H. Sn-doped Ni/YSZ anode catalysts with enhanced carbon deposition resistance for an intermediate temperature SOFC. *Appl. Cat., B.* **2010**, *97*, 1-2, 108-114.

(126) Gavrielatos, I.; Drakopoulos, V. and Neophytides, S. G. Carbon tolerant Ni-Au SOFC electrodes operating under internal steam reforming conditions. *J. Catal.* **2008**, *259*, 1, 75-84.

(127) Triantafyllopoulos, N. C. and Neophytides, S. G. Dissociative adsorption of CH4 on NiAu/YSZ: The nature of adsorbed carbonaceous species and the inhibition of graphitic C formation. *J. Catal.* **2006**, *239*, 1, 187-199.

(128) Gavrielatos, I.; Montinaro, D.; Orfanidi, A. and Neophytides, S. G. Thermogravimetric and electrocatalytic study of carbon deposition of Ag-doped Ni/YSZ electrodes under internal CH4 steam reforming conditions. *Fuel Cells* **2009**, *9*, 6, 883-890.

(129) Nikolla, E.; Schwank, J. and Linic, S. Comparative study of the kinetics of methane steam reforming on supported Ni and Sn/Ni alloy catalysts: The impact of the formation of Ni alloy on chemistry. *J. Catal.* **2009**, *263*, 2, 220-227.

(130) Singh, A. and Hill, J. M. Evaluation of Sn-modified Ni/YSZ SOFC anodes for the direct utilization of methane. *J. Electrochem. Soc. Trans.* **2011**, *35*, 1, 1397-1406.

(131) Brett, D. J. L.; Kucernak, A. R.; Aguiar, P.; Atkins, S. C.; Brandon, N. P.; Clague, R.; Cohen, L. F.; Hinds, G.; Kalyvas, C.; Offer, G. J.; Ladewig, B.; Maher, R.; Marquis, A.; Shearing, P.; Vasileiadis, N. and Vesovic, V. What happens inside a fuel cell? Developing an experimental functional map of fuel cell performance. *ChemPhysChem* **2010**, *11*, 13, 2714-2731.

(132) Snoeck, J. W.; Froment, G. F. and Fowles, M. Steam/CO2 reforming of methane. Carbon filament formation by the boudouard reaction and gasification by CO2, by H-2, and by steam: Kinetic study. *Ind. Eng. Chem. Res.* **2002**, *41*, 17, 4252-4265.

(133) Takenaka, S.; Kato, E.; Tomikubo, Y. and Otsuka, K. Structural change of Ni species during the methane decomposition and the subsequent gasification of deposited carbon with CO2 over supported Ni catalysts. *J. Catal.* **2003**, *219*, 1, 176-185.

(134) Toebes, M. L.; Bitter, J. H.; Jos van Dillen, A. and de Jong, K. P. Impact of the structure and reactivity of nickel particles on the catalytic growth of carbon nanofibers. *Cat. Today* **2002**, *76*, 33-42.

(135) Calizo, I.; Bejenari, I.; Muhammad, R.; Guanziong, L. and Balandin, A. A. Ultraviolet Raman microscopy of single and multilayer graphene. *J. Appl. Phys.* **2009**, *106*, 043509-1-043509-5.

(136) Chhowalla, M.; Ferrari, A. C.; Robertson, J. and Amarantunga, G. A. J. Evolution of sp^2 bonding with deposition temperature in tetrahedral amorphous carbon studies by Raman spectroscopy. *Appl. Phys. Lett.* **2000**, *76*, 11, 1419-1421.

(137) Kirtley, J. D.; McIntyre, M. D.; Halat, D. M. and Walker, R. W. Insights into SOFC Ni/YSZ anode degradation using in situ spectrochronopotentiometry. *J. Electrochem. Soc. Trans.* **2013**, *50*, 44, 3-15.

(138) Endo, M.; Kim, Y. A.; Takeda, T.; Hong, S. H.; Matusita, T.; Hayashi, T. and Dresselhaus, M. S. Structural characterization of carbon nanofibers obtained by hydrocarbon pyrolysis. *Carbon* **2001**, *39*, 2003-2010.

(139) Cantoro, M.; Hofmann, S.; Mattevi, C.; Pisana, S.; Parvez, A.; Fasoli, A.; Ducati, C.; Scardaci, V.; Ferrari, A. C. and Robertson, J. Plasma restructuring of catalysts for chemical vapor deposition of carbon nanotubes. *J. Appl. Phys.* **2009**, *105*, 064304, 064304-1-064304-10.

(140) Karmazyn, A. D.; Fiorin, V. and King, D. A. Direct sticking and differential adsorption heats as probes of structural transitions: O-2 on the stepped Ni{211} surface. *J. Am. Chem. Soc.* **2004**, *126*, 43, 14273-14277.

(141) Bengaard, H. S.; Nørskov, J. K.; Sehested, J.; Clausen, B. S.; Nielsen, L. P.; Molenbroek, A. M. and Rostrup-Nielsen, J. R. Steam reforming and graphite formation on Ni catalysts. *J. Catal.* **2002**, *209*, 2, 365-384.

(142) Faes, A.; Hessler-Wyser, A.; Zryd, A. and Van Herle, J. A review of redox cycling of solid oxide fuel cells anode. *Membranes* **2012**, *2*, 3, 585-664.

(143) Parravano, G. The catalytic oxidation of carbon monoxide on nickel oxide. 1. Pure nickel oxide. *J. Am. Chem. Soc.* **1953**, *75*, 6, 1448-1451.

(144) Royer, S. and Duprez, D. Catalytic oxidation of carbon monoxide over transition metal oxides. *Chem. Cat. Chem.* **2011**, *3*, 1, 24-65.

(145) Kirtley, J. D.; Steinhurst, D. A.; Owrutsky, J. C.; Pomfret, M. B. and Walker, R. A. In situ optical studies of methane and simulated biogas oxidation on high temperature solid oxide fuel cell anodes. *Phys. Chem. Chem. Phys.* **2014**, *16*, 1, 227-236.

(146) Staniforth, J. and Ormerod, R. M. Running solid oxide fuel cells on biogas. *Ionics* **2003**, *9*, 336-341.

(147) Alves, H. J.; Bley, C.; Niklevicz, R. R.; Frigo, E. P.; Frigo, M. S. and Coimbra-Araujo, C. H. Overview of hydrogen production technologies from biogas and the applications in fuel cells. *Int. J. Hydrogen Energy* **2013**, *38*, 13, 5215-5225.

(148) Trimm, D. L. Catalysts for the control of coking during steam reforming. *Cat. Today* **1999**, *49*, 3-10.

(149) Burghgraef, H.; Jansen, A. P. J. and van Santen, R. A. Theoretical investigation of CH4 decomposition on Ni: Electronic structure calculations and dynamics. *Faraday Discuss.* **1993**, *96*, 337-347.

(150) Gorte, R. J. and McIntosh, S. Directy hydrocarbon solid oxide fuel cells. *Chem. Rev.* **2004**, *104*, 4845-4865.

(151) Jalan, B. P. and Rao, Y. K. A study of the rates of catalyzed boudouard reaction. *Carbon* **1978**, *16*, 175-184.

(152) Wang, S.; Liao, X.; Hu, J.; Cao, D.; Li, Y.; Wang, J. and Jiao, H. Kinetic aspect of CO2 reforming of CH4 on Ni(111): a density functional theory calculation. *Surf. Sci.* **2007**, *601*, 5, 1271-1284.

(153) Hauch, A. and Mogensen, M. Ni/YSZ electrode degradation studied by impedance spectroscopy: Effects of gas cleaning and current density. *Solid State Ionics* **2010**, *181*, 15-16, 745-753.

(154) Kim, Y.; Kim, J. H.; Bae, J.; Yoon, C. W. and Nam, S. W. In situ analyses of carbon dissolution into Ni-YSZ anode materials. *J. Phys. Chem. C* **2012**, *116*, 13281-13288.

(155) Chen-Wiegart, Y. K.; Cronin, J. S.; Yuan, Q.; Yakal-Kremski, K. J.; Barnett, S. A. and Wang, J. 3D Non-destructive morphological analysis of a solid oxide fuel cell anode using full-field X-ray nano-tomography. *J.Power Sources* **2012**, *218*, 348-351.

(156) Vert, V. B.; Melo, F. V.; Navarrete, L. and Serra, J. M. Redox stability and electrochemical study of nickel doped chromites as anodes for H-2/CH4-fueled solid oxide fuel cells. *Appl. Catal., B* **2012**, *115*, 346-356.

(157) Cheng, Z.; Wang, J. H.; Choi, Y. M.; Yang, L.; Lin, M. C. and Liu, M. L. From Ni-YSZ to sulfur-tolerant anode materials for SOFCs: Electrochemical behavior, in situ characterization, modeling, and future perspectives. *Energy Environ. Sci.* **2011**, *4*, 11, 4380-4409.

(158) Zhao, F. and Virkar, A. V. Dependence of polarization in anode-supported solid oxide fuel cells on various cell parameters. *J. Power Sources* **2005**, *141*, 1, 79-95.

(159) Pomfret, M. B.; Steinhurst, D. A. and Owrutsky, J. C. Methanol and ethanol fuels in solid oxide fuel cells: A thermal imaging study of carbon deposition. *Energy Fuels* **2011**, *25*, 6, 2633-2642.

(160) Sumi, H.; Lee, Y. H.; Muroyama, H.; Matsui, T. and Eguchi, K. Comparison between internal steam and CO2 reforming of methane for Ni-YSZ and Ni-ScSZ SOFC anodes. *J. Electrochem. Soc.* **2010**, *157*, 8, B1118-B1125.

(161) Pomfret, M. B.; Steinhurst, D. A. and Owrutsky, J. C. Ni/YSZ solid oxide fuel cell anodes operating on humidified ethanol fuel feeds: An optical study. *J. Power Sources* **2013**, *233*, 331-340.

(162) Bouwman, R. and Freriks, I. L. C. In situ fourier-transform infrared spectroscopic study of the interaction of CO with Ni/SO2 in the absence and presence of H2 at 70 - 180C. *Appl. Surf. Sci.* **1980**, *4*, 1, 21-36.

(163) Seiferth, O.; Wolter, K.; Dillmann, B.; Klivenyi, G.; Freund, H. J.; Scarano, D. and Zecchina, A. IR investigations of CO2 adsorption on chromia surfaces: Cr2O3 (0001)/Cr(110) versus polycrystalline alpha-Cr2O3. *Surf. Sci.* **1999**, *421*, 1-2, 176-190.

(164) Pollard, M. J.; Weinstock, B. A.; Bitterwolf, T. E.; Griffiths, P. R.; Newbery, A. P. and Paine, J. B., III A mechanistic study of the low-temperature conversion of carbon monoxide to carbon dioxide over a cobalt oxide catalyst. *J. Catal.* **2008**, *254*, 2, 218-225.

(165) Pomfret, M. B.; Demircan, O.; Sukeshini, A. and Walker, R. A. Fuel oxidation efficiencies and exhaust composition in solid oxide fuel cells. *Environ.Sci. Technol.* **2006**, *40*, 5574-5579.

(166) Ashcroft, A. T.; Cheetham, A. K.; Green, M. L. H. and Vernon, P. D. F. Partial oxidation of methane to synthesis gas using carbon dioxide. *Nature* **1991**, *352*, 6332, 225-226.

(167) REN21. 2012. *Renewables 2012 global status report* [online] (Paris). http://www.ren21.net/ren21activities/globalstatusreport.aspx (accessed 17 Feb. 2014)

(168) Jönsson, O.; Polman, E.; Jensen, J. K.; Eklund, R.; Schyl, H. and Ivarsson, S. Sustainable gas enters the European gas distrubution system, *Danish Gas Technology Center,* **2003**, http://www.dgc.eu/sites/default/files/filarkiv/documents/C0301_sustainable_gas.pdf (accessed 15 Dec. 2014).

(169) Sameshima, S.; Furukawa, N.; Hirata, Y. and Shimonosono, T. Cell performance of SOFC using CH4-CO2 mixed gases. *Ceram. Int.* **2014**, *40*, 6279-6284.

(170) Ruckenstein, E. and Hu, Y. H. Carbon dioxide reforming of methane over nickel alkaline earth metal oxide catalysts. *Appl. Catal., A* **1995**, *133*, 1, 149-161.

(171) Yu, Y.; Mao, B. H.; Geller, A.; Chang, R.; Gaskell, K.; Liu, Z. and Eichhorn, B. W. CO2 activation and carbonate intermediates: an operando AP-XPS study of CO2 electrolysis reactions on solid oxide electrochemical cells. *Phys. Chem. Chem. Phys.* **2014**, *16*, 23, 11633-11639.

(172) Li, X. X.; Lee, J. P.; Blinn, K. S.; Chen, D. C.; Yoo, S.; Kang, B.; Bottomley, L. A.; El-Sayed, M. A.; Park, S. and Liu, M. L. High-temperature surface enhanced Raman spectroscopy for in situ study of solid oxide fuel cell materials. *Energy & Environmental Science* **2014**, *7*, 1, 306-310.

(173) Leone, P.; Lanzini, A.; Delhomme, B.; Ortigoza-Villalba, G. A.; Smeacetto, F. and Santarelli, M. Analysis of the thermal field of a seal-less planar solid oxide fuel cell. *J. Power sources* **2012**, *204*, 100-105.

(174) Larminie, J. and Dicks, A. *Fuel cell systems explained;* 2nd; John Wiley and Sons, Ltd: West Sussex, England, 2003; 25-43.

(175) Ratnasamy, C. and Wagner, J. P. Water gas shift catalysis. *Catalysis Reviews-Science and Engineering* **2009**, *51*, 3, 325-440.

(176) Hunt, J.; Ferrari, A.; Lita, A.; Crosswhite, M.; Ashley, B. and Stiegman, A. E. Microwave-specific enhancement of the carbon-carbon dioxide (Boudouard) reaction. *J. Phys. Chem. C* **2013**, *117*, 51, 26871-26880.

(177) Tang, P.; Zhu, Q. J.; Wu, Z. X. and Ma, D. Methane activation: the past and future. *Energy & Environmental Science* **2014**, *7*, 8, 2580-2591.

(178) Ginsburg, J. M.; Pina, J.; El Solh, T. and de Lasa, H. I. Coke formation over a nickel catalyst under methane dry reforming conditions: Thermodynamic and kinetic models. *Ind. Eng. Chem. Res.* **2005**, *44*, 14, 4846-4854.

(179) Gur, T. M. Critical review of carbon conversion in "carbon fuel cells". *Chem. Rev.* **2013**, *113*, 8, 6179-6206.

(180) Gismatullin, E. and Lundgren, K. Branson's butanol heading to U.S. as ethanol substitute. http://www.bloomberg.com/news/2014-01-29/branson-s-butanol-heading-to-u-s-as-ethanol-substitute.html (accessed Oct. 8, 2014).

(181) Sasaki, K.; Watanabe, K. and Teraoka, Y. Direct-alcohol SOFCs: Current-voltage characteristics and fuel gas compositions. *J. Electrochem. Soc.* **2004**, *151*, 7, A965-A970.

(182) Harper, M. R.; Van Geem, K. M.; Pyl, S. P.; Merchant, S. S.; Marin, G. B. and Green, W. H. Comprehensive reaction mechanism for n-butanol pyrolysis and combustion. *Combust. Flame* **2011**, *158*, 10, 2075-2075.

APPENDICES

APPENDIX A

ADDITIONAL EXPERIMENTS: TO ACCOMPANY CHAPTER THREE

In Figure A.1 shown below, the correlated spectroscopic and electrochemical data are shown for each trial, along with the derivative plots corresponding to each. The time values associated with the maximum (electrochemical derivative) and first local minimum (spectroscopic derivative) in each plot are designated the electrochemical equivalence point and first spectroscopic equivalence point, respectively. These results are summarized in Table 3.1 in the text. All SCP measurements were taken at 725 °C ±10°C on the same MEA after graphite formed from a 20 mL/min flow of CH_4, 106 mL/min Ar gas mixture of either 10 minutes (Trials 1-5, 7) or 30 minutes. (Trial 6). Applied currents were 30 mA (Trials 1-5) and 20 mA (Trials 6-7). Flow rates during SCP measurements were 106 mL/min Ar.

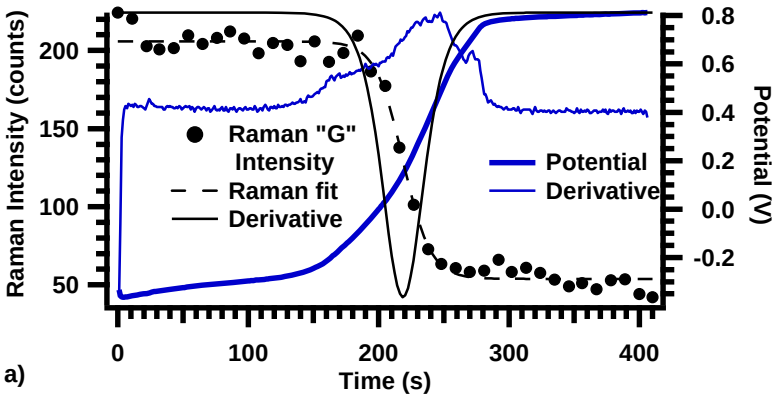

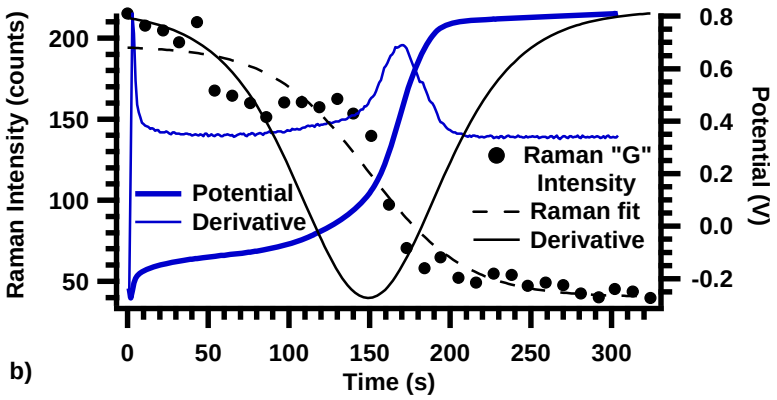

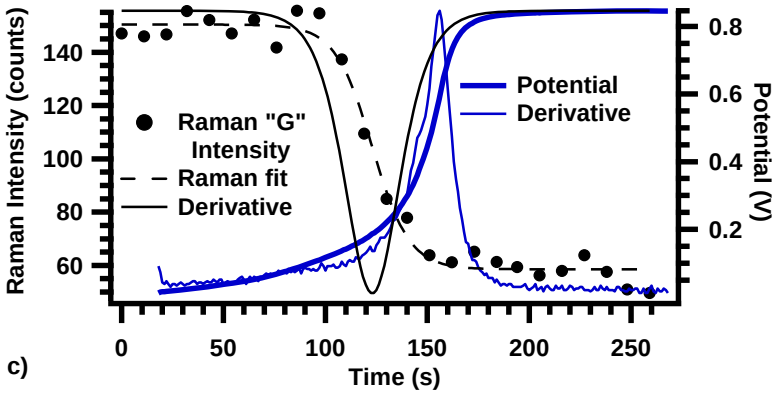
Raman Intensity (counts)
140
120
100
80
60
0
50
100
150
200
250
Time (s)
Potential (V)
0.8
0.6
0.4
0.2
Raman "G" Intensity
Raman fit
Derivative
Potential
Derivative

c)

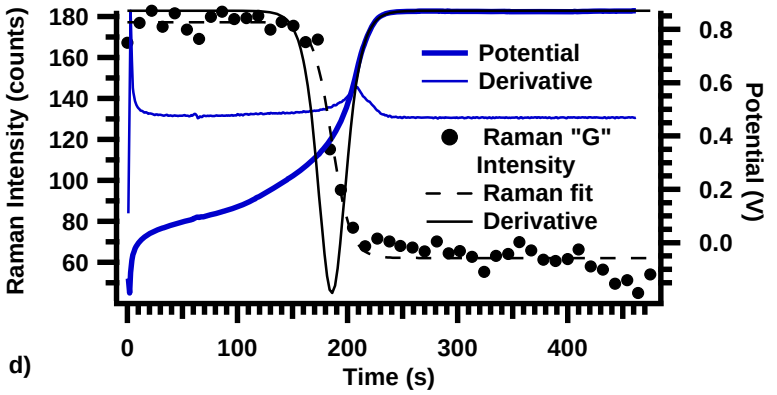
Raman Intensity (counts)
180
160
140
120
100
80
60
0
100
200
300
400
Time (s)
Potential (V)
0.8
0.6
0.4
0.2
0.0
Potential
Derivative
Raman "G" Intensity
Raman fit
Derivative

d)

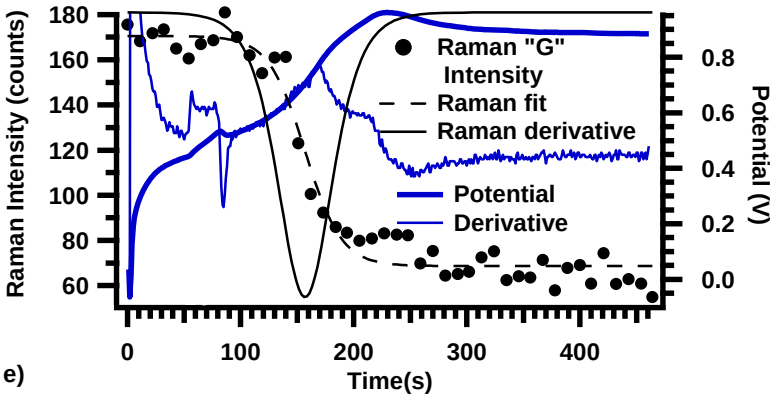
Raman Intensity (counts)
180
160
140
120
100
80
60
0
100
200
300
400
Time(s)
Potential (V)
0.8
0.6
0.4
0.2
0.0
Raman "G" Intensity
Raman fit
Raman derivative
Potential
Derivative

e)

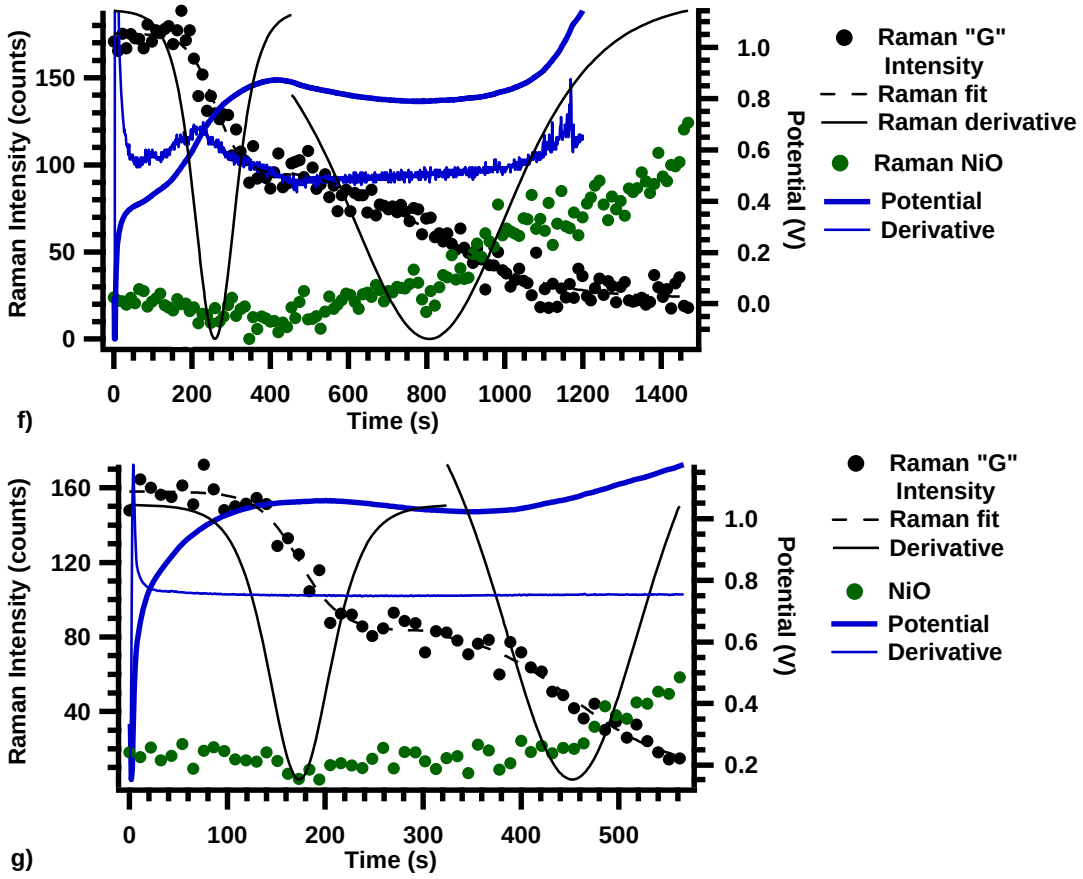

Figure A.1. Trials 1-7 in a-g, respectively.

The data shown in Figure A.2 below were collected in a fashion similar to that shown above. In this case however, hydrogen, rather than deposited carbon, served as the fuel source. These trials were conducted on a different MEA -- slightly smaller in diameter (1.2 cm diameter electrodes, 1.9 cm diameter electrolyte) -- but constructed in a similar manner. Flow rates during all benchmark and SCP tests were 18 mL/min H_2, 106 mL/min Ar at the anode, and 129 mL/min air at the cathode. Temperatures remained at 725 °C ±10 °C. To complete a H_2 SCP trial, the cell was polarized at ~70% I_{max} (80 mA) first under benchmark hydrogen flows (0 - ~210 s). In Figure A.2 below, it can be seen that cell potential approached a steady value of -250 mV before turning off H_2 while

continuing to polarize the cell at 80 mA. After this point, the cell potential rose slowly until H_2 fuel in the system either reacted at the anode or exited as exhaust. After this point, cell potential rose quickly (equivalence point ~465 s). Spectroscopically-observable NiO appeared about 40 s after this first jump. Cell potential stabilized briefly from ~500-535 s while NiO signal continued to rise. After 535 s, the cell potential jumped again (with a corresponding equivalence point at ~560 s).

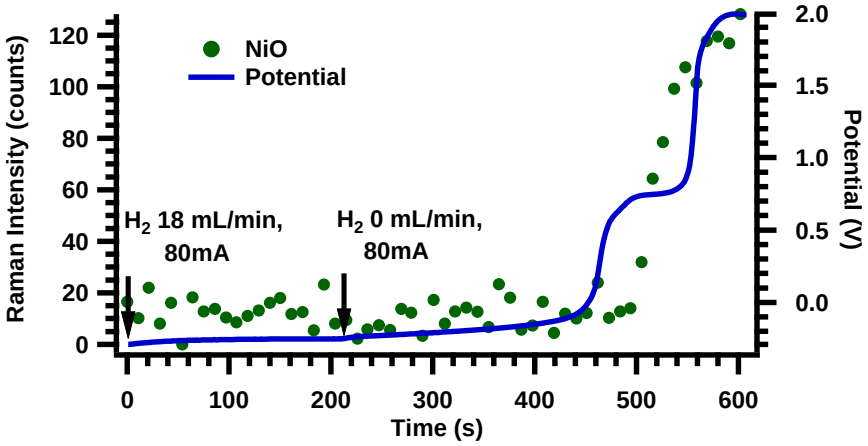

Figure A.2. SCP trial 4 with hydrogen at ~725 °C and under 80 mA. 0-210 sec: 18 mL/min H_2, 106 mL/min Ar; 210-605sec: 129 mL/min Ar. Raman Intensities have been offset to bring minimum point to zero.

APPENDIX B

ADDITIONAL FIGURES TO ACCOMPANY CHAPTER FIVE

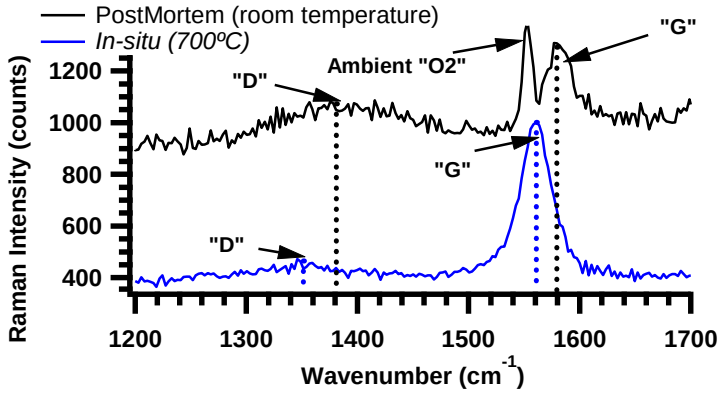

Figure B.1. Comparison of Raman spectra of "G" and "D" peaks acquired with 488nm excitation. Spectra were acquired *in situ* from an anode-supported MEA at 700 °C operating at OCV under 25 mL/min CH_4 and 150 mL/min Ar at the anode (blue) and from the same MEA at room temperature under ambient atmosphere (black). The sample location was identical for both measurements. A larger "D" peak indicates more disorder and altered structural morphology of graphitic deposits upon cool down relative to that measured *in situ*.

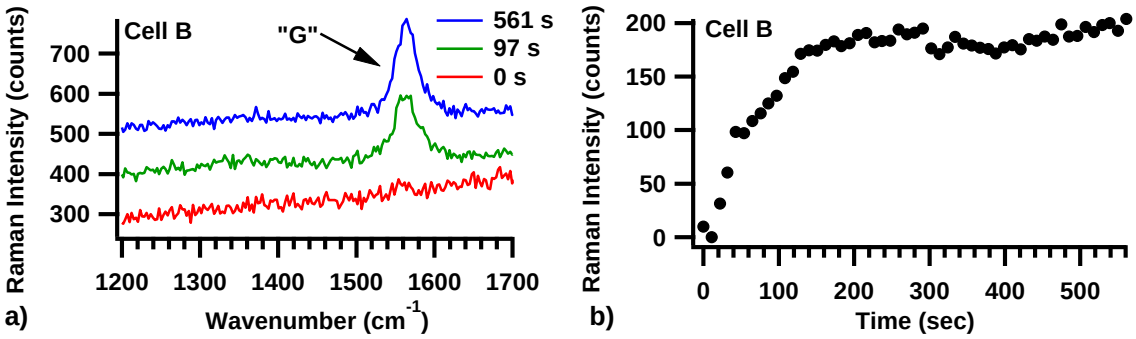

Figure B.2. (a) Growth in the Raman "G" vibrational mode of graphite on a Ni/YSZ anode during 565 s of methane exposure at ~730 °C over Cell B. Each spectrum represents a 10 sec accumulation. Spectra have been offset vertically for clarity. (b) Intensity of the G peak at 1556 cm^{-1} as a function of time, offset to bring minimum point to zero. This figure mimics closely the figure shown for Cell A in chapter 5 (Figure 5.3).

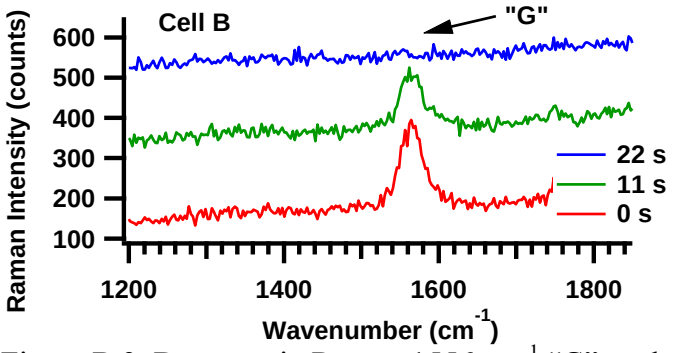

Figure B.3. Decrease in Raman 1556 cm^{-1} "G" peak intensity as H_2O quickly removes surface carbon in Cell B. This figure mimics closely the figure shown for Cell A in chapter 5 (Figure 5.4a).

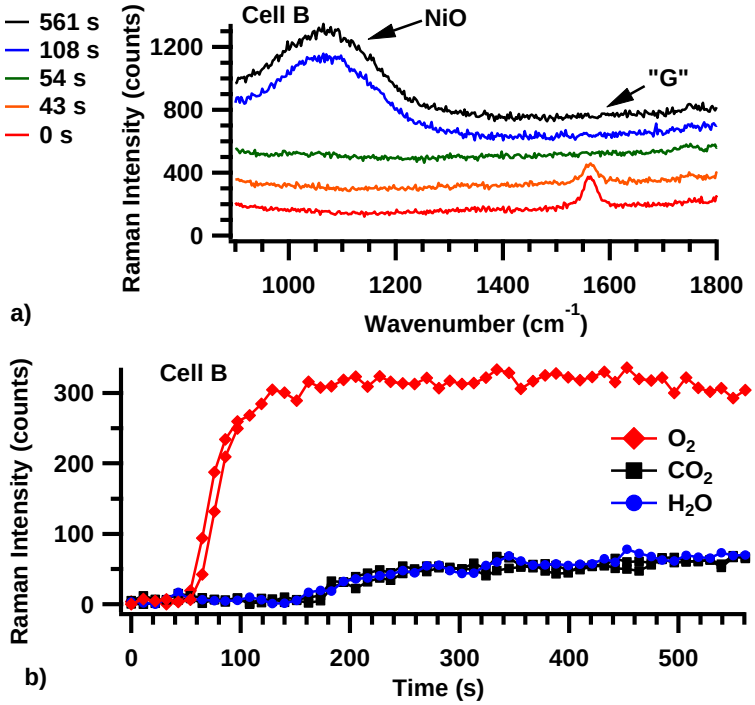

Figure B.4. After carbon is removed from the anode NiO (1050cm^{-1}) forms rapidly from a small amount of O_2 at ~730°C (a). NiO peak intensities (offset to bring lowest point to 0) are plotted as a function of time for H_2O, CO_2 and O_2 at ~730°C (b). This figure mimics closely the figure shown for Cell A in chapter 5 (Figure 5.5).

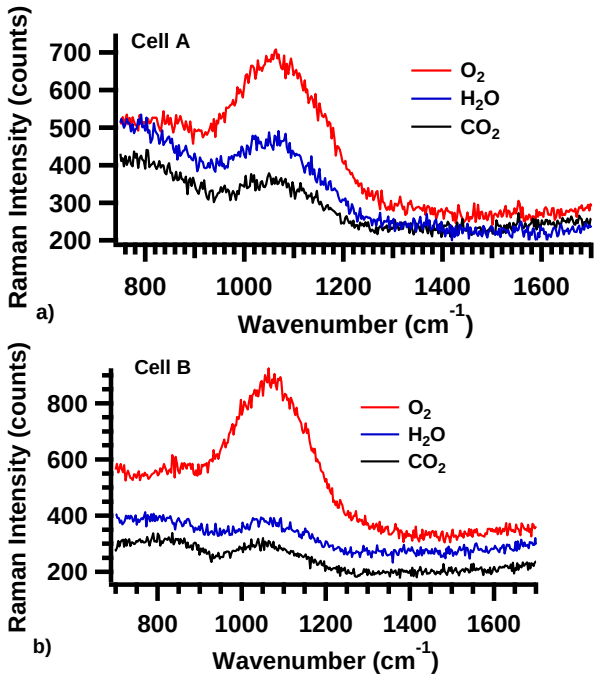

Figure B.5. Spectra acquired while exposing anodes from Cells A (a) and B (b) to O_2, H_2O, and CO_2. Spectra represent oxidized samples near the end of each oxidant exposure. "H_2O" trace in (b) has been vertically offset for clarity.

APPENDIX C

FURTHER EXPLANATION OF OPTICAL MEASUREMENTS IN CHAPTER SIX

Two experimental rigs used to test optical signatures of different chemical processes occurring *in operando* were similar. The rig used for Raman measurements (and simultaneous NIRTI measurements) was designed in particular to allow close optical access of the Raman microscope objective (10x, ~12mm working distance) to the anode surface (Figure C.1). The NIR camera was positioned to the side from a perspective similar to that of the photograph below. Features highlighted in this figure (including fuel inlet, gold current collector, thermocouple, alumina seal) are oriented in positions similar to those in Figure 6.1 of the main text. There are, however, some slight differences in orientation.

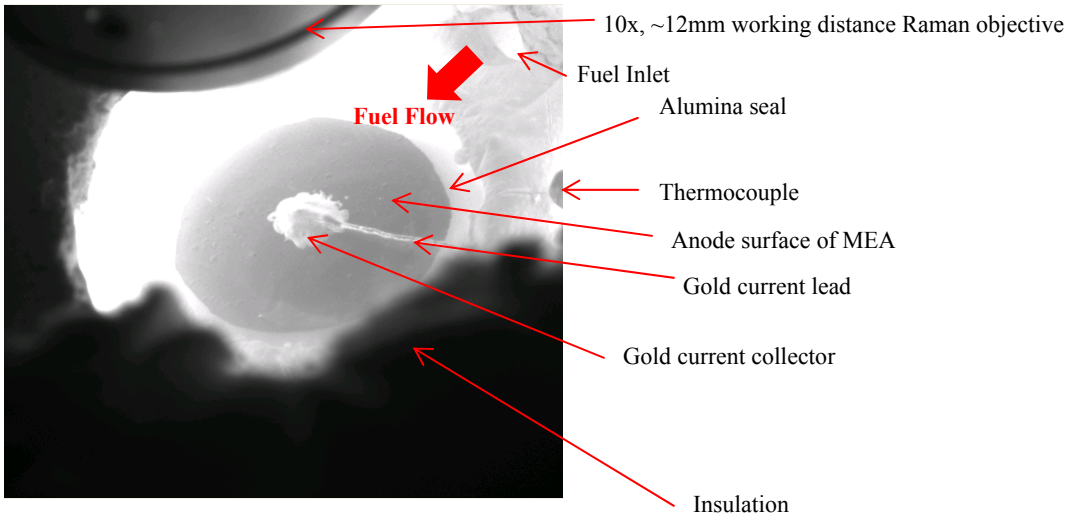

Figure C.1**.** Photograph of an operational (and representative) anode-supported MEA.

Because fuel flow in an operating MEA is unidirectional from a single inlet across the surface of the anode, chemical processes are neither homogeneous nor symmetric across the surface. Rather, the most striking phenomena that provide clues into fuel-dependent chemical processes occur nearest the inlet and directly in the fuel stream. This

is evidenced in Figure C.2a, where endothermic cooling is very pronounced under simulated biogas (see Fig. 6.3b of main text). In Figure C.2b, this inhomogeneity is further exemplified, where the decrease in temperature is plotted as a function of time within three different sample areas (R1-3 as shown in Figure C.2a). As expected, temperatures in all three sample areas drop rapidly under the introduction of biogas and stabilize earliest for R3 and last for R1. The drop in temperature is most pronounced for R1.

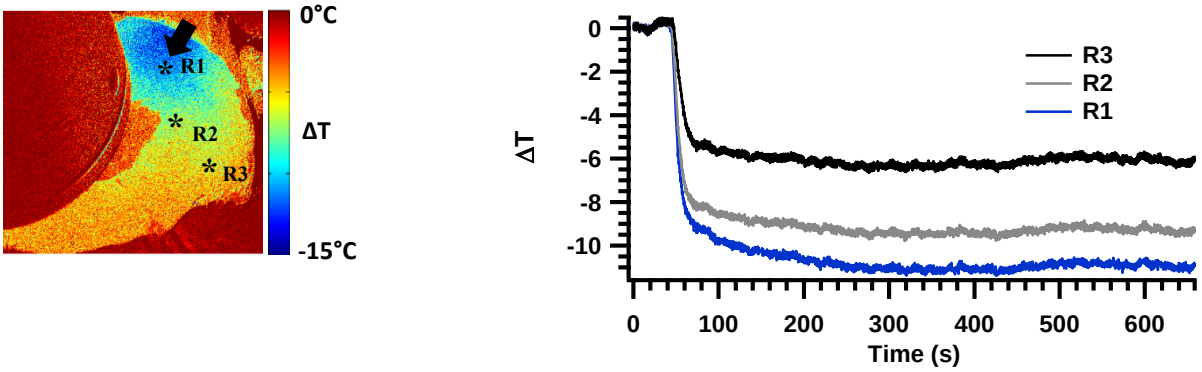

Figure C.2. Cooling of an MEA anode operating under simulated biogas at OCV and 800ºC. The NIR themal image in a) is identical to that shown in Figure 6.3a of chapter 6. Time-dependent cooling under these same conditions are shown in b) in three different sample areas R1-3 indicated in Figure C.2a.

APPENDIX D

ELECTROCHEMICAL DEPENDENCE OF ANODE COOLING: TO ACCOMPANY CHAPTER SEVEN

NIR thermal images recorded temperature changes across the anode surface, in particular near the fuel inlet, during different anode processes. The surface temperature cooled near the end of a ten minute exposure to methane or biogas relative to the initial surface temperature under hydrogen. Figure D.1 below indicates that this amount of cooling was even more pronounced when the cell was also polarized during fuel exposure. This was true in all cases, as seen from the negative d(ΔT). The additional, electrochemically-induced cooling was strongest under methane fuel at 800 °C.

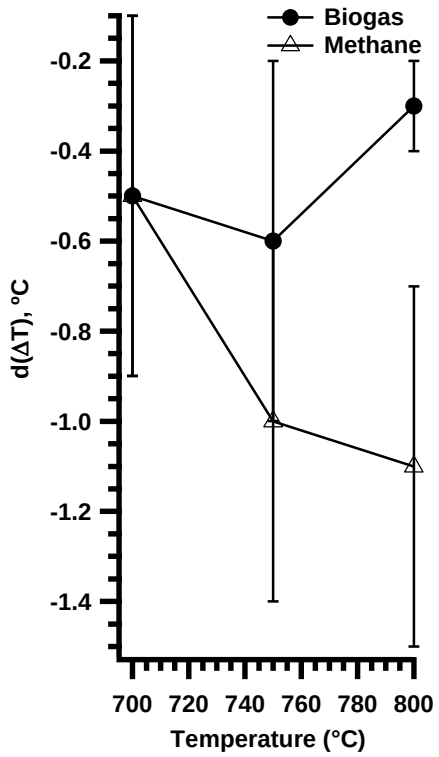

Figure D.1. Differential cooling observed on the anode surface at 75% I_{max} relative to OCV during fuel exposure; $d(\Delta T)_p = \Delta T(75\%\ I_{max}) - \Delta T\ (OCV)$ this difference is represented as d(ΔT). Data points reflect averages over 2-3 trials; error bars reflect experimental variation.